Engineering Room-Temperature Quantum Magnetic Sensors with Fibre-Cavity Diamond Lasers

By

Sarath Raman Nair

A thesis submitted to Macquarie University
for the degree of Doctor of Philosophy
Department of Physics and Astronomy
June 2020

MACQUARIE
University
SYDNEY·AUSTRALIA

Typeset in LaTeX 2_{ε}.

Except where acknowledged in the customary manner, the material presented in this thesis is, to the best of my knowledge, original and has not been submitted in whole or part for a degree in any university.

Sarath Raman Nair

Acknowledgements

I would like to thank a number of people regarding the successful completion of this thesis. First of all I would like to thank my principle supervisor A/Prof. Thomas Volz for his guidance throughout my PhD candidature. Thank you Thomas for offering a PhD position in your group and believing in me. Thank you for patient and constant encouragement as well as motivating advice, when it was necessary. Thank you for being a nice person, with whom working was really enjoyable. I would like to thank my associate supervisor Dr. Lachlan Rogers. Thank you Lachlan for your invaluable contribution in shaping an experimentalist in me. Thank you for your constant support and motivation whenever it was necessary. Thank you for sharing your curiosity in technologies. I would like to thank Dr. Xavier Vidal for patiently introducing me to the basics of cavity experiments, and encouraging me to experiment with it. I would like to thank A/Prof. Gavin Brennen, for being helpful when ever I approach you with something. I would like to thank my fellow colleagues Dr. Guillermo Munoz Matutano, Matthew van Breugel, Reece Roberts, Andrew Wood, and Dr. Cyril Laplane for their support and motivation. Thank you Guillermo for your company in the lab and for sharing the lab. Thank you for our discussions over lunch and thank you for the table soccer games that we played. Thank you Reece for our discussions and proof reading my thesis. I would like to thank whole QMAPP group. I would like to thank Dr. Jan Jeske, for your collaboration, constant support and advising me over theoretical modellings. It was really pleasant to work with you on a project that was proposed by you. I would like to thank Fraunhofer IAF, Freiburg, for facilitating my visit. I thank Macquarie University and EQUS for the facilities and support provided during the course of this project. I acknowledge that the work was done while holding international Macquarie University Research Excellence Scholarship (iMQRES). I acknowledge, the EQUS centre collaboration awards. I would like to express my gratitude to CSIRO Lindfield for the facilities they provided.

I thank Dr. Aravind M. Warrier, Dr. Sandhya Clements, Gayathri Bharathan, Elisabeth Wagner for their support and help during the PhD time.

I thank Achan, amma, appa, amma, Jerry, and all my cousins. I would like to thank all my teachers for shaping a student in me. Finally, I do not have any words to express gratitude to my love Jemy. Thank you Jemy for your amazing companionship and support.

List of Publications

- Sarath Raman Nair, Lachlan Rogers, Xavier Vidal, Reece P. Roberts, Hiroshi Abe, Takeshi Ohshima, Takashi Yatsui, Andrew D. Greentree, Jan Jeske, and Thomas Volz *Amplification by stimulated emission of nitrogen vacancy centres in a diamond-loaded fiber cavity.* arXiv preprint arXiv:1912.05801 (2019).

- Sarath Raman Nair, Lachlan Rogers, David J. Spence, Richard P. Mildren, Fedor Jelezko, Andrew D. Greentree, Thomas Volz, and Jan Jeske *Absorptive laser threshold magnetometry: combining diamond Raman lasers and nitrogen-vacancy centres*. (to be submitted)

Abstract

This thesis studies the engineering of quantum magnetic sensors based on diamond lasers containing NV^- colour centres. Specifically, the thesis experimentally and theoretically investigates two different scenarios for realizing diamond lasers in mechanically tunable fibre-based Fabry-Perot cavities.

In the first scenario, we experimentally explore a diamond-loaded open tunable fiber-cavity system as a contender for realizing lasing with the negatively charged nitrogen-vacancy (NV^-) centre in diamond as the gain medium. We measure the transmission characteristics of a cavity-resonant laser beam at a wavelength of 721 nm, close to the maximum of emission of the NV^- phonon sideband, both with and without a green pump laser at 532 nm. For moderate green pump powers, we observe an amplification of the resonant red laser light and at the same time a reduction of the spontaneously emitted background photons. When increasing the pump power further, the amplification saturates and at the same time we see an increase in spontaneous photon emission. A qualitative model including stimulated emission and charge state switching of the NV^- centre captures the dynamics in the experiment very well. The results allow conclusions to be drawn about the material challenges of realizing an NV^- laser in diamond.

In the second scenario, we theoretically study Raman lasing from a diamond crystal containing NV^- centres. The intra-cavity absorption by the NV^- centres modifies the Raman laser, and two interesting regimes are identified based on the position of the Raman and pump laser wavelengths with respect to the zero-phonon line (637nm) of the NV^- centre. When both the pump and Raman wavelengths are below the zero-phonon line we identify a magnetically tunable bistability. When only the pump wavelength is below the zero-phonon line, we predict a shift in the laser threshold dependent on the NV^- spin centres. Furthermore, we propose that such a system can be used as a technically demanding magnetic field sensor with a predicted DC sensitivity of the order of $\mathrm{pT}/\sqrt{\mathrm{Hz}}$.

Contents

List of Figures

List of Tables

"If you think you understand quantum mechanics, you don't understand quantum mechanics."

Richard P. Feynman

1 Introduction

Quantum physics has always remained as a field of great interest, despite its conceptual complexities that go beyond everyday human perceptions. The twentieth century witnessed the emergence of quantum physics, saw how it flourished and how it quickly revolutionized technology through inventions like lasers, transistors, computers, etc., that in turn further fuelled more scientific discoveries and eventually led to the internet and smartphones - to only name two commodities that we would not want to miss in everyday life. If we regard this revolution as the first quantum revolution, then we are now in the midst of the so-called second quantum revolution or quantum revolution 2.0 [1–5]. While the first quantum revolution harnessed mainly the wave-particle duality of the quantum world, the second quantum revolution puts the focus on engineering new technology using the more 'esoteric' properties of the quantum world, namely superposition, entanglement and the concept of quantum measurement [2, 3]. By and large, the second quantum revolution has been enabled by an exquisite laboratory control over fragile quantum systems, down to the level of single atoms, ions and photons.

Even for one of the pioneers of quantum mechanics, Erwin Schrödinger, experiments with single quantum particles were unimaginable and comparable with raising "Ichthyosauria in the Zoo" [6]. Almost 70 years later, quantum physicists are able to use laser light to manipulate single atomic qubits either in isolation or within a solid-state matrix. They are able to create on-chip micron-sized superconducting qubits at a scale that brings quantum supremacy to reality [7]. All around the world, quantum research into new technology is currently experiencing a real boost, funded both through public support but also by global companies such as Microsoft, IBM and Google. The potential of these efforts to repay in the form of disruptive technologies goes well beyond state-of-the art with hitherto largely unexplored real-world impact [2, 4]. Australia has been a pioneer in this space, funding several national Centres of Excellences in Quantum Science. The first to propagate the idea of 'engineered quantum technology' was Professor Gerard Milburn at University of Queensland who founded the ARC Centre of Excellence for Engineered Quantum Systems (EQUS) [8, 9] in 2011. Prompted by external stakeholders and local key players in quantum computing, the New South Wales Government recently established the Sydney Quantum Academy (SQA) [10] aimed at training and job creation in the quantum technology sector.

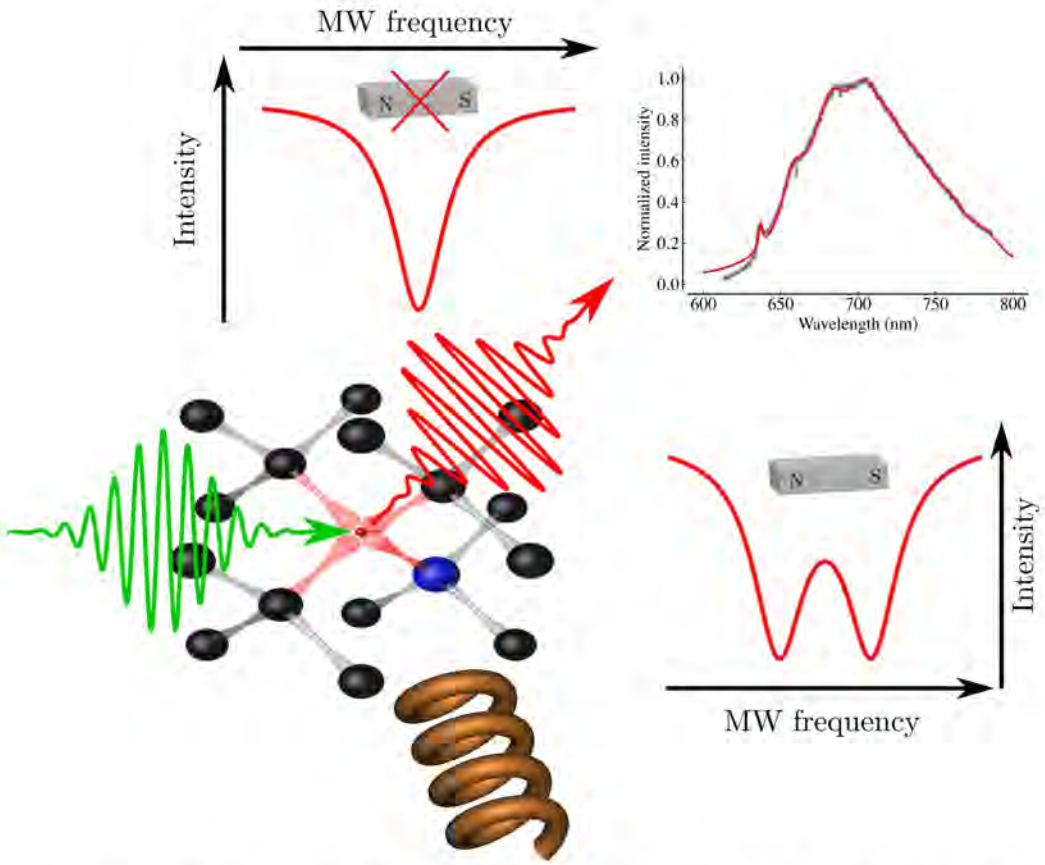

Figure 1.1: Schematic of magnetic sensing with an NV^- centre. The NV^- centre forms in a diamond matrix with carbon atoms (black spheres) bonded together, by replacing carbon atom with a Nitrogen atom (blue sphere) and a vacancy with dangling bonds with the carbon atoms and captures extra electron (small red sphere). The NV^- centre can be excited with a green photon and emits a red photon. With green excitation the emission spectra of the NV^- centre typically spans from 600 nm to 800 nm. The magnetic field can be detected by looking at the change in the intensity of light emitted by the NV^- centre by sweeping the MW around a frequency of 2.88 GHz, which is the ground state resonance frequency of the NV^- centre.

There are different application areas such as quantum information processing, quantum communication as well as cryptography, and quantum sensing within the second quantum revolution [1–3, 11]. Quantum sensing is one of the key areas that shows great promise to yield innovative technologies within the second quantum revolution on a relatively short time frame [2, 4, 12]. In the conventional picture, external noise disturbs the coherent quantum nature of the system under consideration and therefore constitutes a threat to the system. Quite a lot of research has been devoted to isolate quantum systems from these external disturbances. Quantum sensing, however, treats noise and the interaction of a quantum system with its surroundings as a feature rather than a bug [2, 4, 12]. A quantum sensor exploits the laws of quantum mechanics to learn something about the environment. Since a quantum state can be made sensitive even to exceptionally weak external noise, quantum sensors can be useful in detecting extremely weak signals. Depending on the particular sensor under question, one can detect for example external magnetic fields, electric fields, temperature, pressure, gravitation and rotation. Among all of these, magnetic-field sensors are one of the most advanced and best developed quantum sensors to date [4, 12]. A prime area of interest for magnetic sensors is the field of biomagnetism [13], specifically in the

study of brain and neural networks [14, 15], the human heart [16] and the steady currents in the body [17]. Other areas of application are the exploration of minerals and more generally geo-resources [18], and aerial navigation [19], specifically in GPS-denied environments.

There are several different quantum systems capable of detecting magnetic fields, namely superconducting quantum interference device (SQUID), atomic vapors in a glass cell, trapped ions and solid-state spins. These are either mature technology (SQUID) or are currently being explored in the context of quantum magnetic sensing [12]. Out of the listed quantum sensors, SQUIDs and atomic vapor cells currently reach magnetic-field sensitivities in the $\mathrm{aT}/\sqrt{\mathrm{Hz}}$ range that are suitable for high sensitivity applications such as the detection of extremely weak brain signals [12, 20, 21]. Whilst the SQUIDs require cryogenic temperatures [12, 20], atomic vapor cells work at temperatures even above room-temperature [21]. Despite their success in high sensitivity, these magnetometers lack high spatial resolution. In contrast, solid-state spins within nano-crystals can in principle bring the spatial resolution down to the nano-scale. In particular, the nitrogen-vacancy (NV) colour centre in diamond [22] has established itself as a key contender and stands out as an exceptional candidate for quantum sensing.

The NV centre is formed when two carbon atoms along one of the four body diagonals of the diamond lattice get replaced by a nitrogen (N) atom and a vacancy (V). The resultant atom-like defect is a spin-half system, known as the *neutral* charge-state of the NV centre or simply as NV^0 [22]. When the NV^0 traps an extra electron, it forms a spin-1 system known as the negatively-charged NV centre or simply as NV^- [22]. For the rest of the thesis, we denote negatively-charged NV centre as NV^-, neutral charge state as NV^0, and the NV centre without specifying the charge state simply as NV.

It is the NV^- which is highly sensitive to external magnetic fields. An illustration of the NV^- centre properties and the idea of magnetic-field detection using the NV^- is displayed in Figure 1.1 Since NV^- is a spin-1 system, it has a spin-triplet ground and excited-state, contrary to the doublet-states for the spin-$\frac{1}{2}$ NV^0 centre. When absorbing and emitting light, the NV^- undergoes spin-dependent optical transitions. These spin-dependent transitions can be manipulated using MW fields around 3 GHz at low magnetic fields. Remarkably, the NV^- fluorescence intensity is spin-dependent, and hence the observed total fluorescence will change once the microwave field induces resonant transitions between the spin sub-levels. This effect is called optically-detected magnetic resonance (ODMR). An external magnetic field Zeeman-shifts the spin levels, and therefore changes the resonance condition for observing ODMR. Hence the ODMR signal is a direct measure of external magnetic fields.

Though the NV^- centre had been regarded as a potential candidate for quantum technologies more than a couple of decades ago [22], only in 2008 was its full potential for sensing magnetic fields recognized [23, 24]. The initial proposals were soon supported by two experimental implementations of NV magnetic field sensing at the nano-scale [25, 26]. Its exceptional properties make the NV^- centre unique and have enabled these breakthrough experiments. In particular, the NV^- centre keeps its quantum nature (spin coherence and single-photon emitter properties) even at room-temperature [22]. It remains stable close to the diamond surface, even in nanodiamonds down to 5 nm diameter [27, 28], and is therefore an ideal candidate for use in nanoscale magnetic field imaging [29]. Sophisticated optical and materials engineering of diamond nanopillars as atomic force microscope (AFM) tips [30] have enabled the successful demonstration of nanoscale imaging of the magnetic field of even single electron spins [31]. Recently, a low-temperature NV scanning system at the University of Basel has been employed to explore magnetic 2D van der Waal (vdW) crystals, revealing

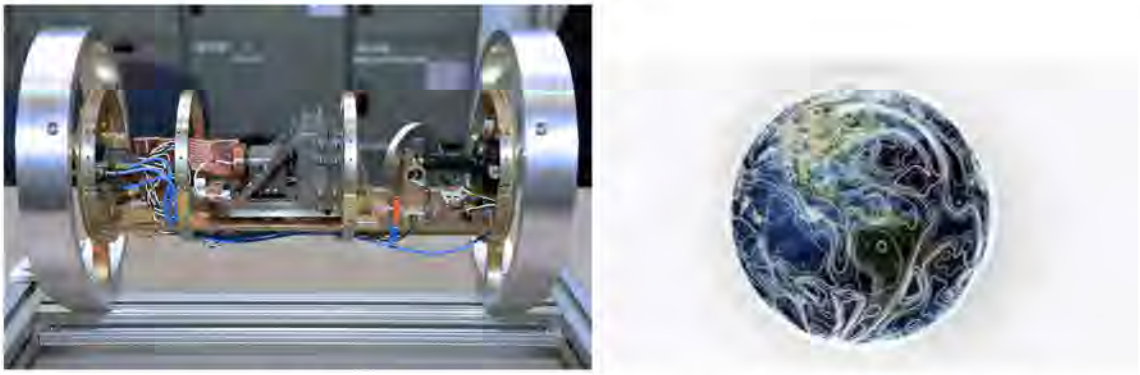

Figure 1.2: Lockheed Martin's 'Dark Ice' quantum magnetometer GPS, by detecting earth's magnetic field. Pictures are included with permission, Source: Lockheed Martin.

for the first time interesting conformation-induced magnetic properties [32]. It looks that there is a market for quantum magnetic sensors at the nanoscale emerging at the moment. In Switzerland two-spin off companies, QZABRE from ETH Zurich [33], and QNAMI from the University of Basel [34], are selling NV-based nanoscale magnetic-field sensing platforms, mainly for the scientific market. In Germany, the Fraunhofer Society has identified quantum magnetic sensing as a key future market opportunity and has therefore established a national lighthouse project on the topic (QMAG), with one of two key technologies based on NV centres.

While single NV^- centres can provide high spatial resolution and good sensitivity, ensembles of NV^- centres enhance the overall sensitivity — albeit at the cost of reduced spatial resolution [35]. Initial expectations of NV^- magnetometry in terms of achievable sensitivities saw it as being comparable to or even better than contemporary state-of-the-art competitors such as SQUIDs and atomic vapor cell systems [12]. However, the best magnetic-field sensitivity experimentally achieved for NV^- ensembles so far is 0.9 $pT/\sqrt{Hz}$ [36]. Regardless, NV^- centres have been successfully employed in experimental demonstrations by imaging living cells [37, 38], and detecting the action-potential of the neuron [39], amongst others. Furthermore, the usefulness of NV^- centre magnetometry in brain imaging was discussed in detail in a recent theoretical study [40]. A real device prototype based on NV^- sensing is the 'Dark Ice' quantum magnetometer shown in Figure 1.2. This remarkable magnetometer developed by Lockheed Martin detects both the local strength and direction of the Earths magnetic field and can therefore help ships and aircraft navigate in GPS denied environments [41, 42].

One of the key points for further improving the sensitivity of NV^- centre-based magnetometers is the read-out efficiency, that is the way the NV^- centre interacts with light and also its fluorescence signal. Most NV^- magnetometers to date rely on spontaneous emission of the NV^- centre(s) [19]. A very interesting alternative is the idea of using stimulated emission of NV^- centres [43, 44] for generating the NV photons. This method is called Laser Threshold Magnetometry (LTM) and was first proposed by Jeske et al. in 2016 [43]. In principle, LTM uses the light field of a laser generated by an ensemble of NV^- centres within a diamond crystal that acts as the magnetic-field dependent gain medium. Theoretically, such an NV^- laser would offer a magnetic-field sensitivity of a few $fT/\sqrt{Hz}$, which would be several orders of magnitude higher than that of state-of-the art NV^- magnetometers. Soon after the proposal appeared, the authors in collaboration with the Quantum Materials and Applications (QMAPP) group at Macquarie University, Sydney, and also others, demonstrated the direct observation of stimulated emission of NV^- centres in 2017 [45]. However, the demonstration

Figure 1.3: A fibre cavity apparatus loaded with an NV rich diamond sample. The green laser at ~ 532 nm is pumped through the cavity fibre. The red emission from the NV centres with the green laser pumping is clearly visible in the picture.

of an NV^- laser is still outstanding. A similar method employing the absorption of light by NV^- centres within a (laser) cavity was proposed recently by Dumeige et al. in 2019 [46]. In this work the authors consider an ensemble of NV centres in an infra-red (IR) laser cavity, and the modification of the laser properties due to the presence of the NV^- centres. In essence, the present PhD thesis makes a contribution, both experimentally and theoretically, to the engineering of an NV-based laser-threshold magnetometer.

The type of optical resonator that is of interest for the present study is a mechanically tunable fibre cavity [47]. The fibre cavity forms between a micron-sized dielectric mirror at the tip of an optical fibre and a macroscopic mirror on which the diamond sample is placed. These mirrors are highly reflective for the wavelengths of interest and thus form a strong intra-cavity field with which the colour centres in the diamond interact. An early version of the fibre-cavity apparatus with diamond sample built during the PhD is shown in Figure 1.3. A key feature of fibre cavities compared to conventional macroscopic cavities is the fact that the light field is confined to extremely small mode volumes [47], resulting in an enhanced interaction with the quantum emitters embedded in the sample. Several groups are currently working towards realizing a spin-photon interface with diamond colour centres in such fibre cavities [47–52]. However, to the best of the author's knowledge, no studies have considered mechanically tunable fibre cavities in the context of building a laser. References [49, 51] explored the challenges of loading fibre cavities with diamond samples of non-negligible thickness. Though these studies are at the other extreme in terms of interaction strength and the number of emitters within the cavity, the general ideas developed there can be extended to the studies presented in this thesis. In fact, the fibre mirrors used for the present study, were originally developed with the idea in mind of engineering a spin-photon interface with diamond colour centres.

The primary goal at the beginning of the PhD work from which this thesis is shaped is to realize an NV^- laser by extending the stimulated emission study [45] into fibre cavities and construct a magnetic sensor from it, in collaboration with Dr Jan Jeske, IAF Fraunhofer, Freiburg, Germany and Prof Andrew D. Greentree from Royal Melbourne Institute of Technology (RMIT), Melbourne, Australia. In order to achieve lasing from NV^- centres, the

strong light-matter interaction in the fibre cavities is expected to support lasing by Purcell enhancement of the spontaneous emission, while the high cavity Q factor should enable stimulated emission and the buildup of a significant intra-cavity field [53]. This experimental PhD work is the first room-temperature work with mechanically tunable fibre cavities, particularly with diamond colour centres, in the Quantum Materials and Applications (QMAPP) group at Macquarie University, Sydney. This thesis was shaped from a strict three year PhD duration including the thesis writing.

1.1 This thesis

This thesis focuses on engineering a quantum magnetic sensor using diamond lasers in mechanically tunable fibre cavities. The work builds on two main key concepts, the first one being quantum magnetometry with NV^- centres and the second one being the realization of diamond lasers in fibre cavities.

The thesis therefore starts with a discussion about the fundamentals of magnetic sensing with NV^- centres in Chapter 2. Then a brief discussion about magnetometry methods based on spontaneous emission and absorption of NV^- centres is also provided in Chapter 2. Towards the end of Chapter 2, the concept of NV^- laser threshold magnetometry is introduced based on reference [43] and is directly compared to the other methods. Since the ultimate goal of this thesis was the realization of an NV^- laser using fiber cavities, a realistic estimate of the expected laser threshold and the associated sensitivities is required. Chapter 3 is devoted to answering these questions. First a brief introduction to optical cavities with a focus on fiber cavities is given in Chapter 3. Next, Chapter 3 explores the expected NV^- laser properties and the prospects for building a fiber-cavity LTM sensor by revisiting the calculations in Reference [43] with our cavity parameters. Interestingly, for the parameters considered in this thesis, the magnetic field sensitivity calculated is only a few $pT/\sqrt{Hz}$ in contrast to the originally proposed $fT/\sqrt{Hz}$. One key challenge that the original LTM proposal by Jeske et al. did not consider is the well-known issue of photo-ionization of the NV^- centre. In the experiments reported in Chapter 4, this photo-ionization of the NV^- becomes apparent.

The main experimental challenge during this PhD was the construction of a mechanically stable fibre cavity platform and its isolation from the environment. The setup and experiments constructed and performed during the course of this PhD are discussed in Chapter 4. While at time of completion of this thesis no lasing has been observed, clear amplification of probe laser light transmission in the diamond loaded fiber cavity was observed, Chapter 4 reports on these observations and presents a qualitative model, including charge state switching and stimulated emission of NV^-, that captures - at least qualitatively - the observations made in the experiments. The work presented in this chapter is currently being refined into a manuscript, which is posted in arXiv.org and will be submitted to a peer-reviewed journal.

Besides the experimental work towards an NV^- based LTM, this thesis also investigates the potential for realizing an absorption-based LTM using diamond Raman lasers. Chapter 5 reports on a theoretical study that looks at the response of a diamond Raman laser in an external magnetic field in the presence of NV^- centres within the diamond crystal [46]. While in principle a magnetic field detector can be constructed in the same manner as for other absorption-based schemes [46], further investigations are required to understand the role of ionization in such a system. The modelling presented in this chapter is also being prepared for publication, and the manuscript will soon be posted on arXiv.org. Based on the findings presented in this thesis, Chapter 6 outlines the challenges and perspectives that line

ahead in the quest for realizing an NV centre based LTM sensor.

2

Quantum magnetometry with NV^- centres

This chapter provides an introduction into magnetic sensing with NV^- centres and an overview of different magnetic sensing methods developed over the years. The chapter starts in section 2.1 with the fundamental ideas for magnetic sensing using the NV^- centre. This section introduces the current understanding about the quantum picture of the NV^- centre, its usefulness in magnetic field detection, and also the concept of sensitivity. Though the focus of this thesis is magnetic field sensing with an ensemble of NV^- centres, we discuss the fundamentals by considering a single centre as a representative one. Then we move on to the discussion about different magnetic field sensing methods in section 2.2. Since NV^- magnetometry is evolving fast, a detailed review of different methods is beyond the scope of this thesis. An interested reader can find more details about different magnetic sensing methods from review articles like references [12, 19, 35, 54, 55] and references therein. Here we discuss the main optical magnetometry techniques in the three categories, the spontaneous emission based techniques, absorption based techniques and stimulated emission based techniques.

2.1 Fundamentals of magnetic sensing with NV^- centre spin

In recent years the underlying physics of the NV^- centre spin system [22] and its application in sensing external magnetic fields [35, 54, 55] have been explored in great detail. The possibility to manipulate the intrinsic optical quantum properties of the NV^- centre at room-temperature makes it an interesting magnetic sensor. The quantum properties of the NV centre based on the energy level diagram, discussed in this section, considers transition rates which are taken from the mean value of the transition rates obtained in reference [56]. Comparable transition rates are experimentally observed in references [57, 58] and are summarized in reference [19]. Since the physics is not expected to change, though these rates may change slightly for different samples, we stick with these rates throughout the thesis.

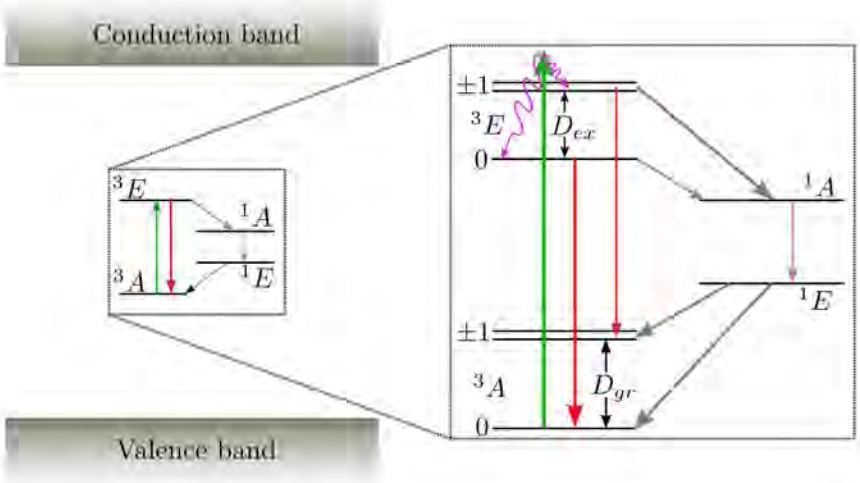

Figure 2.1: Energy level diagram of the NV⁻ centre showing spin dependent optical transitions. The triplet ground and excited sates are denoted as ^{3}A and ^{3}E respectively. The ground and excited states' splitting in the absence of any external field are denoted as $D_{gr} \sim 2.88$ GHz and $D_{ex} \sim 1.42$ GHz respectively [22]. The singlet states are denoted as ^{1}A and ^{1}E. The non-resonant optical excitation of the NV⁻ centre is shown in green arrows. The non-radiative transitions are shown in magenta curly arrows. Radiative spontaneous emission transitions (600 nm - 800 nm) are shown in red arrows. The inter-system crossing transitions which does not preserve spin conservation are shown in grey arrows. The infrared emission around 1042 nm is shown by a brown arrow. For simplicity, the phonon transitions in the ground state and also between the singlet states are not shown.

2.1.1 Quantum picture of the NV⁻ centre spin system

The NV⁻ centre energy levels are within the band gap between the valence and conduction bands of the diamond [54, 59]. An energy level representation of the NV⁻ centre in the band gap of diamond is shown in Figure 2.1. This centre consists of a ground state (^{3}A), an excited state (^{3}E) and two meta-stable states (^{1}A and ^{1}E). As mentioned in the introduction chapter, the NV⁻ centre is a spin 1 system. The ^{3}A and ^{3}E are spin triplet levels. As a result these two levels have fine splitting [22] based on the spin state. However, the ^{1}A and ^{1}E states are singlet states [22].

The energy of the NV⁻ centre spin is quantized along the dangling bond between the Nitrogen and the vacancy, which can be denoted as the NV axis. The two triplet states ^{3}A and ^{3}E have $m_s = 0$, $m_s = +1$ and $m_s = -1$ states. Ideally, in the absence of any external field, the $m_s = \pm 1$ of the ground and excited state are degenerate. The splitting between the $m_s = 0$ and $m_s = \pm 1$ of the NV⁻ ground state in the absence of any external field is $D_{gr} \sim 2.88$ GHz and the corresponding excited state splitting is $D_{ex} \sim 1.42$ GHz [22] at room-temperature. Typically, even in the absence of any external field, the strain in the diamond crystal can also affect the degeneracy of the ± 1 state, so that these levels can split [22, 35]. Strain in bulk diamond samples is typically lower compared with nanodiamonds [35]. Since we focus on a bulk diamond sample in this thesis, we consider the strain induced splitting to be zero in order to simplify the physics in this subsection. Furthermore, the phonon levels of both the ground and excited states are neglected for simplicity. However, later in this chapter we will consider the impact of the phonon levels as they are important for the research presented in this thesis.

As shown in Figure 2.1, the NV⁻ centre is usually exited from the ground state to the

excited state using non-resonant green light ($\sim$ 532 nm, which is a typical wavelength). Between ground state and excited state, the NV^- centre undergoes spin conserving optical transitions. The green light excites the NV^- centre from the ground state $m_s = 0$ and ±1 levels to the phonon levels of the excited state $m_s = 0$ and ±1 levels respectively and quickly decay non-radiatively down to respective levels of the excited state. In Figure 2.1, the phonon levels of the excited state are not drawn.

From the excited state there are two paths to decay down to the ground state. The first one is the spin conserving transition from excited state to the ground state and the second one is a spin non-conserving transition known as the inter-system crossing (ISC) through the singlet levels [22, 35]. The spin conserving transition from excited state to ground state happens from $m_s = 0$ to $m_s = 0$ and from $m_s = \pm1$ to $m_s = \pm1$. Photons emitted during this spin conserving transition account for the visible emission spectrum. Due to the phonon-levels in the ground state the emission is broad, roughly between 600—800 nm. The transition rate for both the direct decay transitions between $m_s = 0$ states and $m_s = \pm1$ states is around 65.93 MHz [56]. The ISC transitions occur from $m_s = 0$ and $m_s = \pm1$ levels of the excited state to the singlet states with uneven transition rates, 7.93 MHz and 53.25 MHz respectively [56]. The maximum life-time of the upper level singlet state, ^{1}A, is around 1 ns [60]. The NV centre decays from ^{1}A to ^{1}E both non-radiatively and radiatively with an infra-red (IR) emission wavelength around 1042 nm [22, 61]. The ^{1}E has a longer lifetime and the NV centre decays from ^{1}E to the ground state $m_s = 0$ and $m_s = \pm1$ with slightly uneven transition rates around 0.98 MHz and 0.72 MHz respectively [56].

Despite the fact that the spin conserving decay transitions have equal transition rates, the population fraction of the NV^- centre available for decay from $m_s = \pm1$ is smaller compared with that from the $m_s = 0$ level of the excited state. This is due to a stronger ISC transition to the singlet state ^{1}A from $m_s = \pm1$ state than that from the $m_s = 0$ state. The ISC transition from $m_s = \pm1$ state is also comparable with the spin conserving transition from these levels. On the other hand, the non-radiative decay transitions from the singlet state ^{1}E to the ground state slightly prefer the $m_s = 0$ over the $m_s = \pm1$ of the ground state. As a result the ISC transitions altogether favour increasing the NV^- population fraction in the $m_s = 0$ state.

Two key points about the intrinsic quantum properties of NV^- centres can be identified. The first one is that continuous excitation with a non-resonant wavelength (e.g. green laser typically around 532 nm) polarizes the NV^- centres to the $m_s = 0$ state. Secondly, the amount of spin conserving decay, producing observable photons, is stronger from the $m_s = 0$ state than from the $m_s = \pm1$ state. Conversely, the amount of ISC transition from the $m_s = \pm1$ state is more than from the $m_s = 0$ state. This allows optical readout of the spin projection.

In the presence of a magnetic field the degenerate $m_s = \pm1$ states split due to Zeeman splitting [22, 35]. By detecting this splitting using the intrinsic optical properties of the NV^- centre, the magnetic field can be sensed. This is typically done by manipulating the ground state spin by applying a microwave (MW) frequency close to the ground state splitting D_{gr} ~2.88 GHz [22, 35].

2.1.2 Magnetic field detection using spin manipulation of the NV^- centre

In order to see the magnetic field influence of the NV^- centre, let us consider the ground state ^{3}A. Let us also assume a co-ordinate system with the z-axis is along the NV^- axis. Then using spin 1 matrices S_x, S_y, and S_z, the ground state Hamiltonian for the NV^- centre in the presence of a weak magnetic field B_w can be approximately written as [22, 35],

$$H_{gr} = hD_{gr}S_z + hE_{gr}(S_x^2 - S_y^2) + g_{es}\mu_B B_w \cdot S, \tag{2.1}$$

where, h is the Planck's constant, E_{gr} is the strain splitting in the ground state, $g_{es} \sim 2.01$ is the g-factor of the NV^- centre [22], and μ_B is the Bohr magneton. In the weak magnetic field regime, the NV^- centre is almost insensitive to perpendicular components of the magnetic field, even up to a few mT [35]. Thus, we consider only the z component of the Hamiltonian in equation (2.1). From the H_{gr} we can obtain two eigen frequencies as [35],

$$\nu_{gr} = D_{gr} \pm \sqrt{(E_{gr})^2 + (\frac{g_{es}\mu_B B_w}{h})^2}. \tag{2.2}$$

These two frequencies corresponds to the splitting between $m_s = 0 \leftrightarrow +1$ and $0 \leftrightarrow -1$. As we discussed these two frequencies are equal (or in other words the +1 and -1 are degenerate in the absence of any external magnetic field), in the approximation $E_{gr} \sim 0$. From equation (2.2), we see that the magnetic field induces further separation in the frequencies and this is the well known Zeeman splitting.

Though for simplicity, we neglected the strain splitting E_{gr} for discussing the energy levels (we will do the same later in the thesis), in reality there will always be some strain induced splitting. This can vary from hundreds of kHz in bulk samples to a few MHz in nanodiamond crystals [35]. From equation (2.2), we can see that Zeeman splitting is visible only if the magnetic field component is much stronger than the strain component. Typically, in experiments for sensing weak magnetic fields, a bias magnetic field to marginalize the strain component is required [35]. However, recent demonstration of magnetic field detection without a bias field in reference [62] opens a new possibility to do bias field free sensing. Since it is beyond the scope of this thesis, we are not going into the details of this paper. In general terms, magnetic field sensing in NV centres occurs by finding the resonant interaction frequency of the microwave drive. This method is known as Optically Detected Magnetic Resonance (ODMR).

ODMR

So far in this chapter, we have not specified the time dependence of the magnetic field. If the magnetic field is static or slowly varying typically up to the frequencies in the kHz range, then it is considered as DC magnetic field [19]. On the other hand, if the magnetic field is oscillating fast typically in the MHz range, it is considered as an AC magnetic field [19].

The DC magnetic field that affects the ground state can be estimated if the two eigen frequencies are somehow connected to the intrinsic optical property of NV^- centre. As we mentioned earlier a MW frequency resonant to the eigen frequencies can do this job. The easiest way to do this is by simultaneously applying a continuous wave (CW) green laser and a CW sweeping of the MW frequency around the ground state splitting. Then, detecting the visible spontaneous emission from the NV^- centre, the resonance frequencies can be detected. An illustration representing the central idea of ODMR is shown in Figure 2.2.

The NV^- centre population evenly splits between $m_s = 0$ and ± 1 at resonant MW frequency, which leads to less $m_s = 0$ population compared with non-resonant MW frequencies. Since the visible red spontaneous emission of the NV^- centre is proportional to the $m_s = 0$ population, the fluorescence drops at the resonant frequency. This is the reason for the observation of a fluorescence dip at the resonant frequency. In the absence of any external field only one resonance dip is observable due to the degeneracy of $m_s = +1$ and -1, whereas, in the presence of a magnetic field, two resonance dips are observable due to the Zeeman

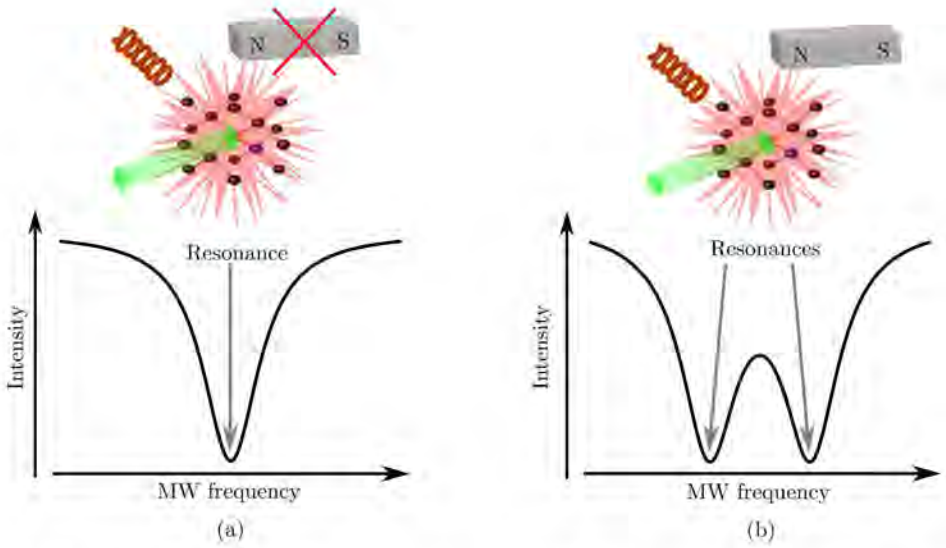

Figure 2.2: Cartoon of the ODMR measurements. The NV⁻ centre excited with a green light gives spontaneous emission of red light. The microwave is shown in brown color and the magnet is shown in grey color. The cartoon of resonances with optical intensity versus microwave frequency plot for without and with magnetic field is shown in (a) and (b) respectively.

splitting. The splitting between the dip is proportional to the magnetic field present and thus can be found from equation (2.2). However, this method of determining the DC magnetic field is not particularly sensitive.

The more sensitive method is to keep the MW frequency fixed and through the change in the optical output induced by the unknown external magnetic field, changes in magnetic field can be detected. The MW frequency corresponding to the maximum slope point of the ODMR dip is the best frequency for this. This point provides the maximum sensitivity magnetic field detection using a CW ODMR method.

2.1.3 Sensitivity

It is important to discuss sensitivity before we move on to see how the underlying physics about magnetic field detection is implemented in experiments. Sensitivity is the figure to compare the performance or quality of a sensor.

The magnetic field is essentially detected using some signal, which is optical as far as this thesis is concerned. Unfortunately, noise is also an unavoidable part of magnetic field detection measurements. In order to infer any information from measurements, the signal has to be distinguishable from the background noise. The limit of usefulness of any measurement is taken to be when the signal to noise ratio is one. The sensitivity of the DC magnetic sensor is defined as the minimum detectable magnetic field using the sensor at this limit, per unit time [12, 35].

Adapting the general sources of noise discussed in [12] for the case of NV⁻, we can see that the main sources of noise in the measurements are quantum projection, interaction of NV⁻ centre with its surroundings, errors in controlling the intrinsic properties of the NV⁻ centre, and noise associated with photons in the optical detection read-out. The quantum projection noise is the fundamental noise associated with projective measurements [12, 63]. This arises

due to the uncertainty in determining the population fractions by projective measurements, which will be discussed in the following section. For the case of optical readout of the NV$^-$ centre, the photon shot noise that arises due to optical readout is the most dominant noise source [35]. The basic idea of different magnetic field detection techniques developed by researchers over the past decade is to reduce all the noises in the measurement and reach the fundamental quantum limit.

Considering only the photon shot noise alone as it is currently the main noise source, we can generally quantify the sensitivity following reference [35] for the research presented in this thesis. The equation for sensitivity is useful for the emission cases, since we are interested in magnetic field sensing using some emission associated with the NV$^-$ centre.

Let the optical signal from NV$^-$ centre have a frequency ν and power P. We apply an infinitesimally small magnetic field δB that produces an infinitesimal change $\delta\phi$ in the photon flux ϕ $(= P/h\nu)$. If we measure the emission for a time period δt, then the photon shot noise in the measurement is $\sqrt{\phi \cdot \delta t}$ and the signal for magnetic field sensing in this measurement is $\delta\phi \cdot \delta t$. Equating this measurement signal to the photon shot noise, the magnetic field sensitivity (η) can be written as [12, 35],

$$\eta = \delta B\sqrt{\delta t} = \sqrt{h\nu}\frac{\sqrt{P}}{\delta P/\delta B}. \tag{2.3}$$

This is a very general form of the sensitivity that we use later in the main part of this thesis. The AC magnetic field sensitivity is generally higher than the DC magnetic field sensitivity by a scaling factor higher than one, due to the improvement in the coherence time in AC magnetometry [24, 35, 43]. The optimum value of the sensitivity is when the $\delta P/\delta B$ is maximum. As we mentioned above, one of the methods for magnetic field detection is by keeping the MW frequency constant and detecting the change in the signal due to the magnetic field noise. This is in general terms, a signal response as a function of detuning between the MW and the NV$^-$ centre ground state. In the absence of any magnetic field, the detuning can be induced by changing the MW frequency. Hence the response signal as a function of magnetic field is proportional to the same signal response as a function of MW frequency. The maximum value of $\delta P/\delta B$ is then proportional to the maximum value of $\delta P/\delta\nu_{mw}$.

Though the response functions are different for different magnetometry methods with NV$^-$ centres as we shall see in the following section, we can generally write the sensitivity irrespective of whether it is a DC or AC magnetic field as [64, 65],

$$\eta \propto \frac{\Delta\nu}{C_{\mathrm{r}}\sqrt{\phi}}. \tag{2.4}$$

Here, C_{r} is the contrast in the response signal due to the magnetic field noise and $\Delta\nu$ is a parameter that basically depends on the spin dephasing time of the NV$^-$ centre ground state. A detailed derivation considering each response function for different magnetometry is beyond the scope of this thesis. An interested reader can find more information in one of the pioneering papers [64].

The CW ODMR response signal that we discussed above is typically a combination of a Gaussian response due to the power broadening and a Lorentzian response due to the natural line shape and the resultant combination is a Voigt response function [65]. Due to the intrinsic properties of the NV$^-$ centre, C_{r} has a fundamental limitation of about 20% for a single centre [35]. The fundamental limit to the line width $\Delta\nu$ is the dephasing rate of the NV$^-$ ground state. However, due to the CW green laser and the MW frequency, the $\Delta\nu$ is

much higher than its fundamental limit. Using an ensemble of NV$^-$ centres instead of a single centre the sensitivity can be enhanced by a factor of square-root of the number of NV$^-$ centres, since the fluorescence improves by the number of NV$^-$ centres [35]. However, using the CW-ODMR method well above the fundamental limit is a major draw back that limits many potential applications of NV$^-$ magnetometry. There are different magnetometry methods developed over the last decade to overcome this challenge in the CW ODMR measurements.

2.2 Different NV$^-$ magnetometry methods

In this section we discuss the magnetic sensing methods using NV$^-$ centres experimentally developed for improving the sensitivity over the CW ODMR method and for practical high-sensitivity applications. As mentioned earlier in this chapter, we consider NV$^-$ magnetometry based on spontaneous emission and absorption here. In the spontaneous emission case, CW ODMR has already been discussed and thus, in this section we discuss the extension of CW ODMR in the transient regime. Even in the CW case, by enhancing the interaction between the magnetic field and the NV$^-$ centre or by more efficiently collecting the spontaneous emission, the sensitivity can be further improved. A good example of this is using light-trapping diamond wave guide work reported in reference [66].

2.2.1 NV$^-$ centre magnetometry using pulse schemes

Pulsed spin manipulation of the NV$^-$ centre and its application in magnetic field detection is based on the resonant interaction of MWs with the NV$^-$ centre in the transient regime. Generally a clear picture of the resonant interaction helps the reader to follow the later part of this thesis. Hence, to make the resonant interaction clear, let us consider the NV$^-$ centre ground state in the absence of any strain or magnetic field, driven with a near-resonant MW frequency. In the rotating wave approximation, the Hamiltonian of the NV$^-$ centre resonantly driven with the MW frequency can be written as,

$$H_{\mathrm{gr,rwa}} = -h\frac{\Delta_{\mathrm{gr}}}{2}\sigma_z + h\frac{\Omega_{\mathrm{gr}}}{2}\sigma_x. \tag{2.5}$$

Here, Δ_{gr} is the detuning between the ground state splitting and the MW, Ω_{gr} is the Rabi frequency, which depends on the strength of the driving field, and σ_{z} and σ_{x} are the Pauli spin matrices. Assuming that all other losses are negligible compared with the dephasing rate (Γ_{gr}), the master equation in Lindblad form [67] can be written as,

$$\frac{\mathrm{d}\rho_{\mathrm{nv}}}{\mathrm{d}t} = -\frac{i}{h}[H_{\mathrm{gr,rwa}}, \rho_{\mathrm{nv}}] - \frac{\Gamma_{\mathrm{gr}}}{2}(\rho_{\mathrm{nv}} - \sigma_{\mathrm{z}}\rho_{\mathrm{nv}}\sigma_{\mathrm{z}}). \tag{2.6}$$

Here, ρ_{nv} is the density matrix for the two level system.

This master equation (2.6) is solved using mesolve in the QuTip python package [68]. For simplicity and to capture the essential physics, we hypothetically consider that the NV$^-$ centre population fraction is fully in the $\mathrm{m_s} = 0$ state at time 0. The resultant time evolution of the population of the ground state spin levels for different detunings are shown in Figure 2.3.

The resonant interaction drives the population fraction between the two levels with the frequency Ω_{gr}. This resonant interaction can be visualized using the Bloch sphere representation as shown in Figure 2.3. When the ground state population fraction is fully at $\mathrm{m_s} = 0$ (or $\mathrm{m_s} = 1$; only +1 is considered for simplicity) the Bloch vector is fully along $|0\rangle$ ($|1\rangle$). If

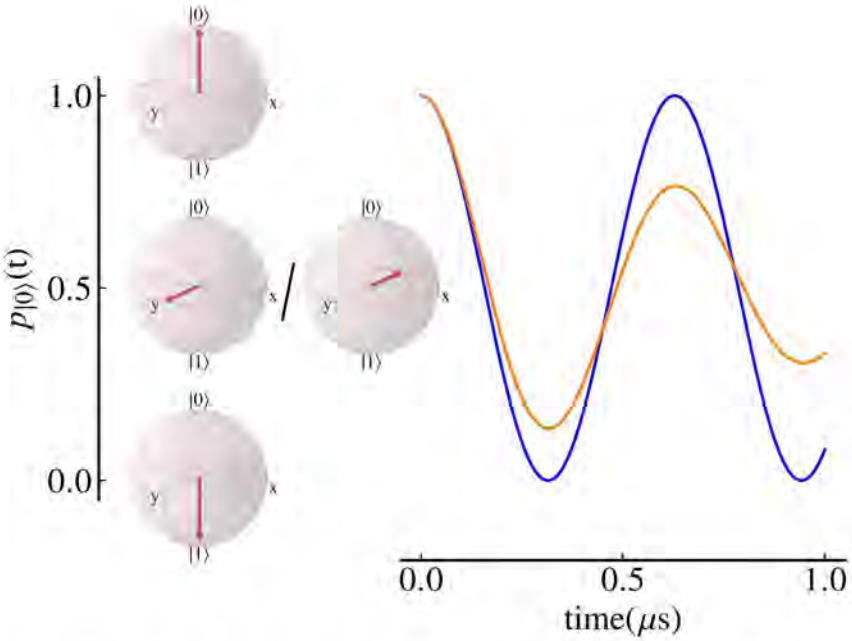

Figure 2.3: Simulated Rabi oscillation due to resonant MW driving of NV$^-$ centre ground state. Ω_{gr} is assumed to be $10/2\pi$ MHz. The blue and orange curves correspond to ideal case without dephasing and with a dephasing rate of 1MHz respectively. The Bloch sphere representation corresponding to each y-axis value is also shown.

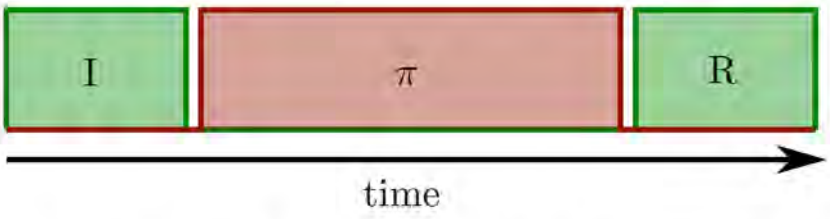

Figure 2.4: Pulse scheme for ODMR in pulsed mode. I denote the initialization pulse of the green laser, π represents the MW pulse and R represents the readout pulse.

the spin state is in equal superposition then the Bloch vector is in the x-y plane. Resonant interaction with the MW for time = $\frac{\pi}{\Omega_{gr}}$, flips the spin population fully from $m_s = 0$ to $m_s = 1$ or vice versa. A MW pulse of this duration is known as a π pulse. A MW pulse of half this duration is known as a $\pi/2$ pulse. A $\pi/2$ pulse puts the fully polarized NV$^-$ centre in to a spin superposition state in the x-y plane of the Bloch sphere.

In the presence of external noises, dephasing dampens the Rabi oscillations. An example of population fraction driving under dephasing is shown in Figure 2.3. With this brief introduction to the resonant interaction of MW with the NV$^-$ centre in the transient regime, we can now see the magnetic field sensing methods.

NV$^-$ magnetomery using pulsed ODMR

This method is the direct extension of CW ODMR magnetometry employing pulsed schemes for detecting DC magnetic fields [69]. In this scheme a green laser pulse alone is applied first

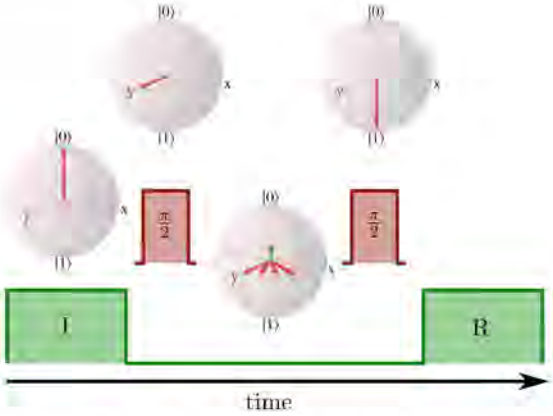

Figure 2.5: Pulse scheme and Bloch's sphere representation of Ramsey magnetometry. The magnetic field noise is shown in green. The evolution of the superposition state is due to Larmor precsion which follows right hand thumb rule.

to initialize the NV⁻ centres spins to the $m_s = 0$ of their ground state. When this initializing pulse turns off, a π pulse is applied in the absence of any green laser light. After the π pulse a green laser pulse is applied to read out the NV⁻ centre fluorescence. When the π pulse is applied to spin polarized NV⁻ centres, the presence of magnetic field affects the perfection in flipping the spin state [19]. Thus, the spin readout gives information about the imperfection in the spin flip and hence the magnetic field can be detected. By sweeping the MW frequency, the ODMR spectrum can be obtained similar to the CW case. In this scheme, since the MW is applied in the dark, there is no power broadening of the NV⁻ centres by the green laser light, but only due to the MW. With this reduction in the noise, the contrast increases and the linewidth reaches close to the dephasing limited value. However, this method is susceptible to variations in Ω_{gr} [19]. The pulse sequence for this method is shown in Figure 2.4.

The duration of a π pulse with the optimum sensitivity is found to be equal to the spin dephasing time ($T_2^* = \frac{2\sqrt{\ln 2}}{\pi\Gamma_{gr}}$, assuming Gaussian line shape for the ODMR dip) [69]. Then $\Delta\nu \sim \Gamma_{gr}$, and the optimized dc magnetic field sensitivity is [69],

$$\eta \approx \frac{\sqrt{2e}(\hbar/(g_{es}\mu_B))}{C_r\sqrt{N_r}\sqrt{T_2^*}}, \tag{2.7}$$

where N_r is the total number of detected photons in the measurement time and it is the product of rate of photon collection (ϕ) in the continuous excitation of NV⁻ centres and the duration of read out pulse [69].

NV⁻ magnetometry with pulse sequences

DC magnetic field detection can be done using Ramsey magnetometry to improve the sensitivity. The pulse scheme for this method is shown in Figure 2.5. The I-pulse polarizes the NV⁻ spins to $|0\rangle$. The $\frac{\pi}{2}$ pulse brings the NV⁻ centres to the superposition state. Then after the $\frac{\pi}{2}$ pulse, the NV⁻ centres, superposition undergoes evolution in the dark. Another $\frac{\pi}{2}$ pulse converters the information about the evolution in to the population fractions by projecting the superposition state to the $|1\rangle$. This population fraction information is read out using the R-pulse. The Ramsey magnetometry signal shows fringes, known as Ramsey fringes. The signal for this method follows $C_r \cos(g_{es}\mu_B B_w \tau_d)$ [19, 64, 65]. Where τ_d is the time corresponding to the evolution of a superposition state under magnetic field noise in the dark

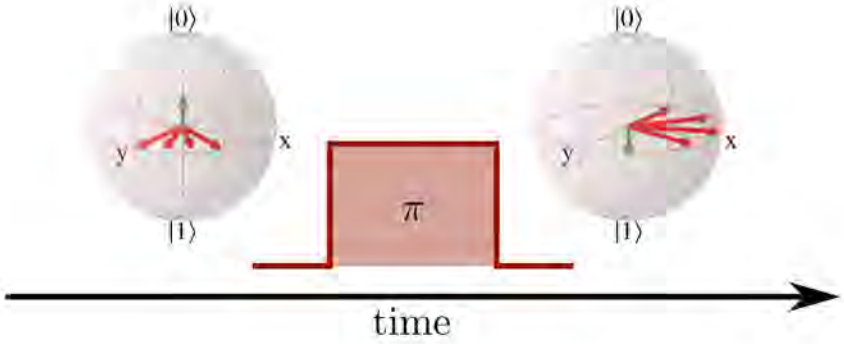

Figure 2.6: π-pulse effect on the ac magnetometry. This π pulse is at the centre of the Ramsey pulse method

and B_w is the effective magnetic field, that induces detuning to the MW driving. The maximum slope of this signal with respect to the magnetic field, which determines the sensitivity, contains τ_d, and the optimum sensitivity is achieved when this free precession time is equal to the spin dephasing time T_2^* [64, 65]. The optimum sensitivity then follows equation (2.7).

An AC magnetic field can be detected if an extra π pulse is added in between the two $\frac{\pi}{2}$ pulses of the Ramsey magnetometry. If one complete cycle of the AC magnetic field is equal to the time between the two $\pi/2$ pulses, then the π pulse at the centre flips the superposition state exactly for half the AC cycle of the magnetic field. As a result, the phase evolution continues as in the Ramsey case. However, since the spin flip suppresses quasistatic noise, the spin dephasing time improves, which results in an increase in the sensitivity. This type of magnetometry method is known as spin echo magnetometry [64]. The effect of an extra π pulse is shown in Figure 2.6.

The optimized sensitvity is when the free precision time is equal to the spin decoherence time, T_2. Then the sensitivity can be written as [64, 65],

$$\eta \sim \frac{(\pi/2)(\hbar/(g_{es}\mu_B))}{C_r\sqrt{N_r}\sqrt{T_2}}. \tag{2.8}$$

The best magnetic field sensitivity (0.9 pT/$\sqrt{\text{Hz}}$ [36]) achieved so far in NV⁻ magnetometry experiments was with AC magnetometry.

2.2.2 NV⁻ absorption magnetometry

So far we discussed magnetometry methods using the emission from the NV⁻ centres. In these techniques, the efficient collection of photons is an important factor [70]. However, due to the internal properties of diamond samples especially with a high density of NV⁻ centres, internal scattering can lose photons and thereby suppress information about the magnetic field [70]. A way to deal with this is to use NV⁻ centres' absorption for magnetometry [71]. The absorption properties of NV⁻ also depends on the intrinsic quantum properties of the NV⁻ centre. Then similar to the above mentioned emission based techniques, the magnetometry with absorption of NV⁻ centre can also be done. However, the key difference in the physics of the absorption case is that the focus is on the long lifetime of the singlet state of NV⁻ centre, in contrast to the spin conserving transition in the emission based methods. Two elegant methods have been experimentally demonstrated. The first one uses absorption of IR wavelength at 1042 nm [72–74]. The second one uses absorption of green laser at ~

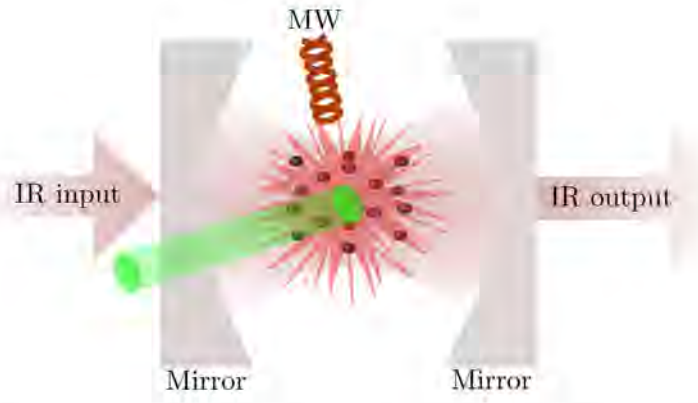

Figure 2.7: Simplified experimental concept of IR absorption magnetic sensing [72–74]. The green color represent the green laser pumping of NV$^-$ centres. Only one NV$^-$ centre is shown as a representative one. The IR output is detected as the signal.

532 nm [70]. These methods used optical cavities in which the diamond sample containing NV$^-$ centres are placed.

The underlying physics of the absorption-based NV$^-$ magnetometry is that when the MW frequency is resonant to the ground state splitting of the NV$^-$ centre, a significant population fraction of the NV$^-$ centre de-excites through the ISC transition to the ground state, more than when the MWs are non-resonant. Since the singlet state has a longer lifetime than the excited state lifetime, NV$^-$ spends significant amount of time in the singlet state. As a result the steady state population of the ground and singlet states of the NV$^-$ centre can be tuned via the magnetic field which in turn controls the absorption [70]. Later in this thesis, we investigate using a Raman laser for absorption-based NV$^-$ magnetometry. Hence we discuss the two absorption magnetometry methods below, to make the reader more familiar with this method.

IR absorption NV$^-$ magnetometry

IR absorption NV$^-$ magnetometry was demonstrated before the green absorption methods in references [72–74]. For IR absorption NV$^-$ magnetometry, the IR wavelength of a 1042 nm cavity is used. A simplified schematic for the IR absorption experiment is shown in Figure 2.7. However, in order to pump the NV$^-$ centres an additional green laser is used. Since the singlet transition wavelength is 1042 nm and the lifetime of the lower singlet state is longer, the NV$^-$ centres reaching the singlet state absorb the IR wavelength. Using MW, the ODMR measurement is done through the cavity transmission signal [72–74]. The best magnetic sensitivity for this method is achieved experimentally with the IR absorption in the pT/$\sqrt{\text{Hz}}$ regime. Since the singlet state population is higher when the MW frequency is resonant, the absorption in the diamond is increased.

A new version of this IR absorption magnetometry has been proposed recently in reference [46] using the idea of laser threshold magnetometry (LTM) [43], which is the main focus of this thesis. In this proposal the MW driven NV$^-$ centres in diamond are used as an absorber inside another IR laser cavity. It is then theoretically shown that the IR laser output can be modified, particularly the threshold behaviour, by an external magnetic field. This work estimates that the sensitivity of such a magnetometer could surpass the pT/$\sqrt{\text{Hz}}$ regime [46].

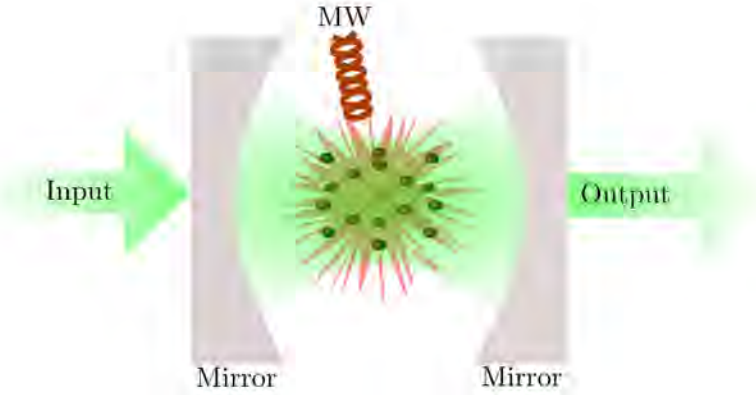

Figure 2.8: Simplified experimental concept of green laser absorption NV$^-$ magnetic sensing [70]. The green color represents the green laser pumping of NV$^-$. Only one NV$^-$ centre is shown as a representative one. The output intensity is detected as the signal.

Green laser absorption NV$^-$ magnetomery

Green laser absorption NV$^-$ magnetomery was experimentally shown recently in reference [70]. In this method an optical cavity for green wavelength is used in which the diamond containing NV$^-$ centres are placed. A simplified version of the sensor in reference [70] is shown in Figure 2.8. The cavity transmission of the green laser is detected during absorption detected magnetic resonance (ADMR), the absorption version of ODMR [70].

In contrast to the IR absorption case, the absorption of green laser is smaller when the MW frequency is resonant and this is detected through the cavity transmission [70]. The main advantage of this method over the infra-red case is that it is easier and does not require any special detectors as required for detecting IR wavelengths. The sensitivity of this method in reference [70] is in the nT/$\sqrt{\text{Hz}}$ regime and has a projected sensitivity of pT/$\sqrt{\text{Hz}}$.

2.3 Magnetometry using NV$^-$ laser

In the previous section, we have discussed magnetometry by using spontaneous emission of NV$^-$ centres and absorption of NV$^-$ centres. However, quite recently a new method has been proposed using the stimulated emission of the NV$^-$ centre, or lasing, at a red wavelength. This emission is generated from the NV$^-$ centres and used for magnetic field detection [43, 44]. We explore the stimulated emission in detail in the next chapters as this is a major focus of this thesis. Here in this section, we briefly summarize the findings in the proposal for direct comparison with the other methods discussed above.

The NV laser based technique is first proposed in reference [43] based on using NV$^-$ centres as a gain medium in an optical cavity with high Q-factor. The NV$^-$ centres embedded in a high Q-factor cavity are pumped with a green laser at 532 nm. The spontaneous emission into the cavity then induces the lasing transition in the phonon side band of the NV$^-$ centre. An energy level diagram representation of the stimulated emission or the lasing transition is shown in Figure 2.9.

Since the laser is formed due to the stimulated emission of the spin conserving transitions, similar to the spontaneous emission case, the spin conserving stimulated emission can be tuned using an external MW field. If a MW frequency is applied resonant to the ground state transition, the presence of magnetic field can change the laser output, especially the laser

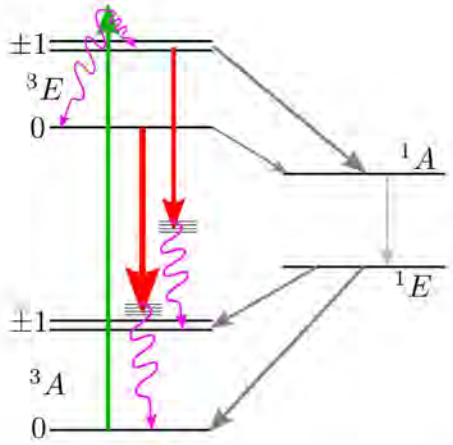

Figure 2.9: Energy level diagram of the NV⁻ centre showing the stimulated emission of NV⁻ centre. The stimulated emission or lasing transition is shown in red arrows. The phonon levels of the ground state are shown in a bunch of black lines. The spin conserving spontaneous emission transitions are not shown in this figure.

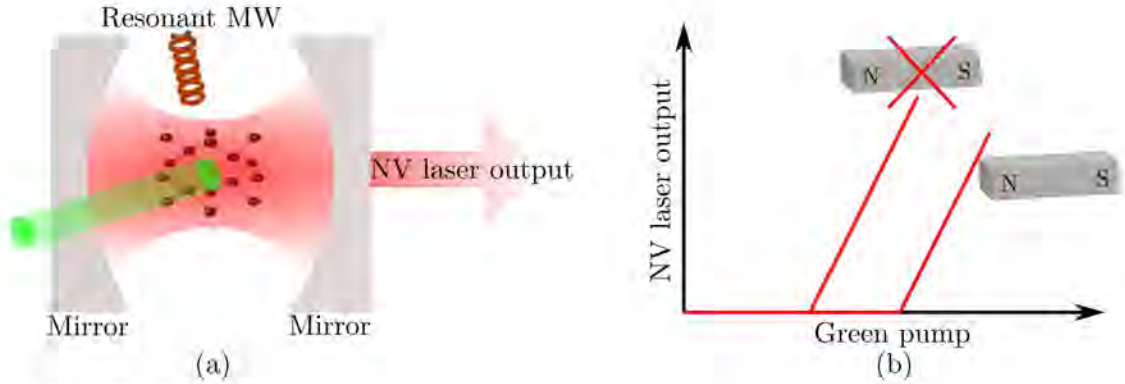

Figure 2.10: Simplified experimental concept of NV⁻ laser magnetometry. (a) NV⁻ laser magnetic sensor. The green color represents the green laser pumping of NV⁻ centres. Only one NV⁻ centre is shown as a representative one. The NV⁻ laser output is the signal. (b) hand drawn cartoon of the NV⁻ laser output in (a) as a function of green laser in the presence and absence of a magnetic field.

threshold [43]. A conceptual cartoon of this method is shown in Figure 2.10.

The sensitivity of such a laser can be represented similarly to the sensitivity given in equation 2.3 [43]. The proposed DC magnetic field sensitivity in reference [43] goes down to a few fT/$\sqrt{\text{Hz}}$. This drastic improvement in the magnetic field sensitivity is due to the directional property of the laser or stimulated emission itself allowing more of the signal to be detected [19]. A similar sensitivity is theoretically calculated even in the absence of the cavity and by only considering amplification due to the spontaneous emission [44]. Since the NV⁻ laser is based on the steady state condition of the lasing process, the NV⁻ laser is only useful for detection of static or slowly varying magnetic fields [43].

In comparison with the spontaneous emission based magnetometry or absorption based magnetometry, the stimulated emission based NV⁻ magnetometry is a conceptually simple method to improve the sensitivity. However, the fundamental challenges in realising this NV magnetometry method still remain. As we already mentioned, the experimental realization of the NV⁻ laser is one of the first challenges. Further challenges such as laser oscillations close

to the laser threshold as speculated by reference [19] still remain. However, the conceptual simplicity of the laser threshold magnetometer has already inspired the adaptation of IR absorption based NV^- magnetometry to next level through the proposal of IR laser threshold magnetometry in reference [46].

3

Magnetometry with a fibre cavity NV^- laser and charge state switching of NV^- centres

This chapter revisits magnetometry with an NV^- laser by considering fibre cavity as the laser resonator. We start with an introduction to optical cavities in the Fabry-Perot geometry, which are applicable to the fibre cavities in section 3.1. Then the NV^- laser in fibre cavity and its response against external magnetic fields are explored in section 3.2. We then briefly discuss stimulated emission in STED microscopy, which is a high resolution microscopy based on the idea of stimulated emission in section 3.3 This section is provided to give an insight into the NV^- stimulated emission process and to introduce the charge state switching of the NV^-. Then in section 3.4, we discuss the charge state switching of the NV centre.

3.1 Fundamentals of Fabry-Perot optical cavity

A Fabry-Perot optical cavity is a two-mirror optical cavity in which the electromagnetic field forms standing waves. One can find the details of optical cavities in standard references like [75] or articles like [76]. Here we briefly review the properties of the optical cavities relevant for this thesis. A schematic of the Fabry-Perot cavity is shown in Figure 3.1. Though the cavities that we are studying are not planar cavities formed by two flat mirrors, most of the underlying physics can be extracted by approximating the cavities with curved mirrors to the planar cavities.

In the figure, the light field enters into the cavity only for certain allowed separations between the two mirrors along the direction of propagation, the z-axis. This quantized light field inside the cavity is known as a longitudinal cavity mode. For each longitudinal cavity mode, the fine tuning of the mirror separation can produce different profiles in the x-y plane due to the boundary conditions when curved mirrors are used. These quantizations in the transverse plane of the longitudinal mode are known as transverse cavity modes. We will see more about these cavity modes in the following subsections.

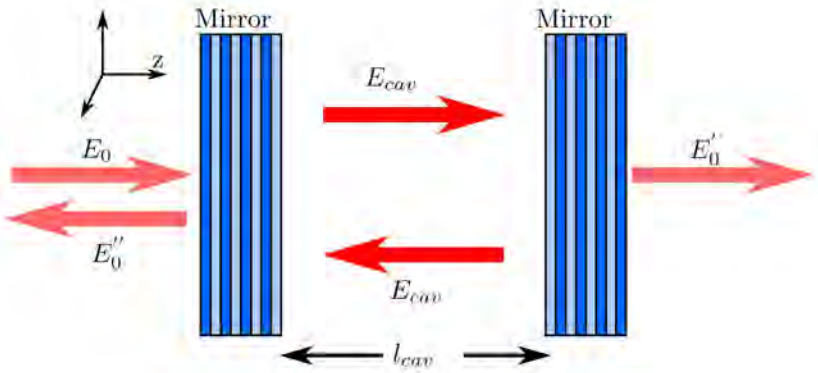

Figure 3.1: A two mirror Fabry-Perot cavity. The cavity mode is shown neglecting the curvature of the mirror. The l_{cav} represent the cavity length. E_0, $E_0^{'}$, $E_0^{''}$ and E_{cav} respectively represent input and transmission, reflection, and intra-cavity electric field intensities associated with the light.

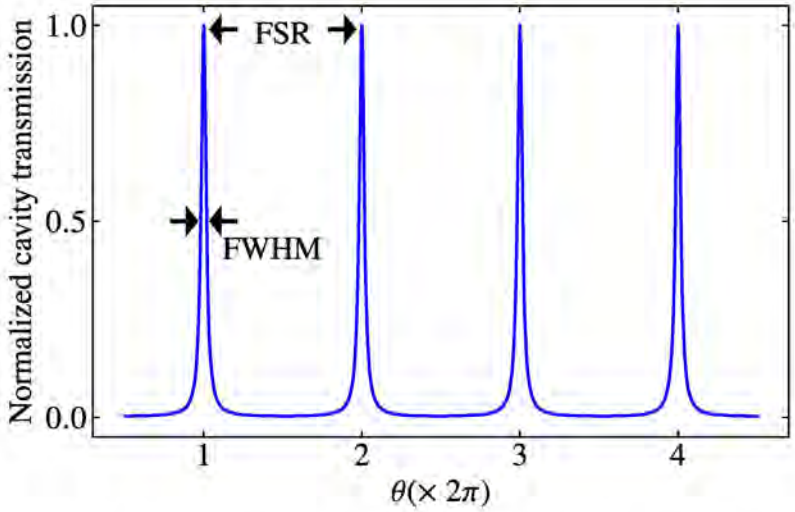

Figure 3.2: Illustration of normalized longitudinal cavity modes as a function of phase difference (θ) corresponding to a round trip. The R considered is 99%. The Free-Spectral Range (FSR) and FWHM are shown in the figure.

3.1.1 Longitudinal cavity modes

As mentioned above the longitudinal cavity modes arise because the light field enters only for certain mirror separations. We can derive the condition for the longitudinal cavity modes.

Consider the cavity and electric fields corresponding to monochromatic light on the cavity as shown in Figure 3.1. Let us assume for simplicity that both the mirrors are identical. Let t and r be the electric field transmission and reflection coefficients of each mirror. Furthermore, let θ be the phase difference accumulated by the electric field bouncing back and forth inside the cavity for one round trip, and d is a loss parameter for the electric field in a single pass through the cavity. We consider the transmitted light, since the studies in this chapter involve the light transmitted through the cavity. Then, the total electric field transmitted through the cavity at steady state can be written as,

$$E_0^{'} = \frac{E_0 t^2 d}{1 - r^2 d^2 \exp\{i\theta\}}. \tag{3.1}$$

In terms of intensity, this can be written as,

$$I_0^{'} = \frac{I_0 T^2 D}{(1-RD)^2} \frac{1}{1+4\frac{RD}{(1-RD)^2}\sin^2\frac{\theta}{2}}, \tag{3.2}$$

where, $D = d^2$, assuming d is a real number that accounts for the losses such as absorption and scattering. The round trip phase difference θ can be written as,

$$\theta = \frac{2\pi}{c} \cdot 2l_{cav} \cdot \nu_{cav}, \tag{3.3}$$

Then from equations (3.2) and (3.3), we see that the transmission of a Fabry-Perot cavity can be tuned either via length of the cavity or via the frequency of the light we are pumping into the cavity.

Assuming an ideal cavity with $D = 0$, the normalized cavity transmission as a function of θ is shown in Figure 3.2. It is clear that the cavity transmission is only allowed when θ is an integer multiple of 2π. These resonance frequencies corresponding to these allowed values can be written as,

$$\nu_j = \frac{c}{2l_{cav}} j, \tag{3.4}$$

where j is an integer. For the other frequencies the light field inside the cavity undergoes destructive interference and the light field does not transmit or enter the cavity, instead it reflects back from the cavity.

Associated with each of these longitudinal modes, there are transverse modes with different orders, which have different spatial profiles in the x-y plane. We can see this in the next subsection.

3.1.2 Transverse cavity modes

Let us consider curved cavity mirrors. The standing EM waves trapped inside the cavity can be expressed using standard wave equations. The electric field associated with the light field inside the cavity obeys the Helmholtz equation in the scalar form and can be written as,

$$(\nabla^2 + \frac{4\pi^2}{\lambda^2}) E_{cav}(x, y, z, t) = 0, \tag{3.5}$$

where ∇^2 represents Laplacian, λ is the wavelength of the light field and E_{cav} is the electric field. Dropping the harmonic time dependence, the E_{cav} can be written as,

$$E_{cav}(x, y, z) = E_{cav}^0 \psi(x, y, z) \exp\left\{-i\frac{2\pi}{\lambda} z\right\}, \tag{3.6}$$

where E_{cav}^0 is the electric field amplitude and $\psi(x, y, z)$ is the envelope of the electric field. In the standard paraxial approximation, that is assuming that the variation in the field envelope along the cavity axis is negligibly slower than that of the x and y directions, we can write the Helmholtz wave equation as,

$$\frac{\partial^2\psi(x, y, z)}{\partial x^2} + \frac{\partial^2\psi(x, y, z)}{\partial y^2} - i\frac{4\pi}{\lambda}\frac{\partial\psi(x, y, z)}{\partial z} = 0. \tag{3.7}$$

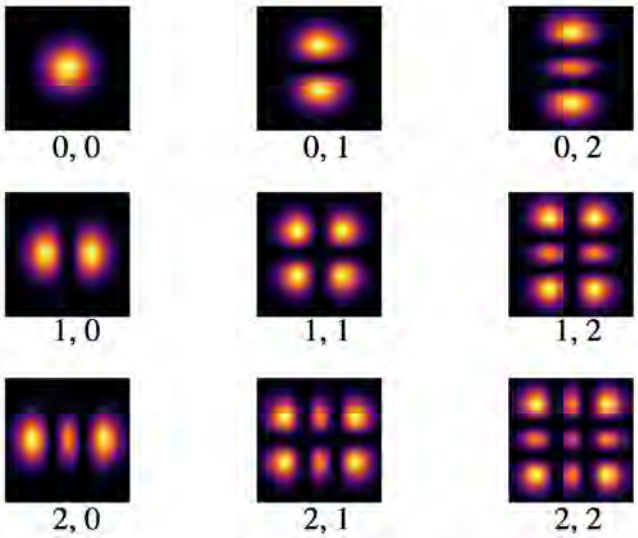

Figure 3.3: Simulated transverse cavity mode profiles up to a few higher order modes. The transverse modes are shown at the mode waist. The m and n values are shown below for each transverse mode as m, n. The mode waist was assumed to be 5μm.

The general solution of the wave equation in equation 3.7 can be written as [77],

$$\psi(x,y,z) = \frac{w_0}{w(z)} H_m\left(\frac{\sqrt{2}}{w(z)}x\right) H_n\left(\frac{\sqrt{2}}{w(z)}y\right) \exp\left\{-\frac{(x^2+y^2)}{w(z)^2}\right\} \exp\left\{-i\frac{\pi}{\lambda}\frac{(x^2+y^2)}{R(z)}\right\} \exp\{i \arctan(z/z_R)\}, \tag{3.8}$$

where H_m and H_n are the m^{th} and n^{th} order Hermite polynomials respectively, w_0 is the waist of the cavity, $w(z)$ is the beam spot size at a distance z from the cavity waist, $R(z)$ is the radius of curvature of the wave-front at a distance z from the cavity waist and z_R is the Rayleigh length. The arctan term corresponds to the phase accumulated along the z direction and is known as the Gouy phase shift. In terms of intensity, the cavity electric field can be written as,

$$I_{cav}(x,y,z) = I^0_{cav}|\psi(x,y,z)|^2, \tag{3.9}$$

The spatial distribution of the cavity mode in the x-y plane is then determined by $|\psi(x,y,z)|^2$. A simulation of this is shown in Figure 3.3. Transverse modes with the Gouy phase shifts modify resonant frequencies given in equation (3.4) [77] and can be written as [77],

$$\nu_j = \frac{c}{2l_{cav}}\left(j + \frac{1}{\pi}(m+n+1)\arccos\left(\sqrt{\left(1-\frac{l_{cav}}{R_1}\right)\left(1-\frac{l_{cav}}{R_2}\right)}\right)\right), \tag{3.10}$$

where R_1 and R_2 are the radius of curvature of the two mirrors. It is clear from equation (3.10) that for each of the longitudinal modes there are transverse modes with different orders.

So far the discussion is about the empty cavity. However, when a sample, for example in the present case a diamond crystal is placed inside the cavity, the cavity resonance conditions change. A derivation of such a cavity resonance is again beyond the scope of this thesis. Such cases have been studied in the past with thick diamond samples inside fibre cavities in the following references [49, 51, 52]. Adapting these results, the resonance frequency of the fundamental Gaussian mode resonant to the sample loaded cavity, in contrast to equation

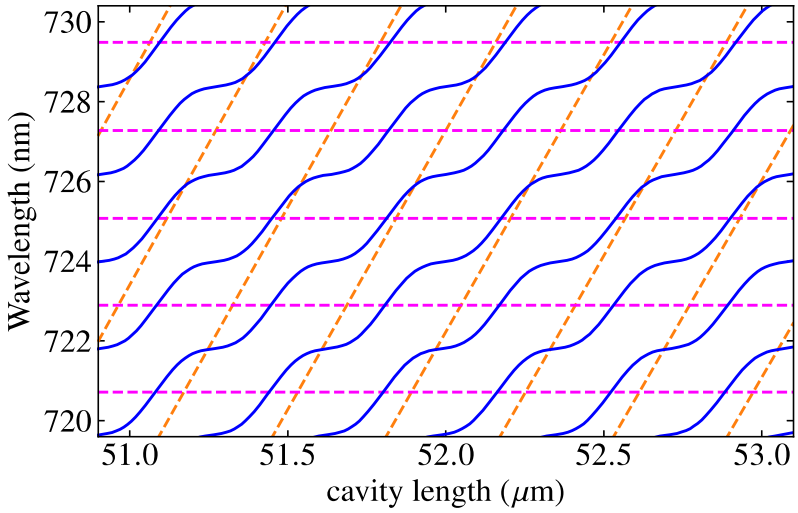

Figure 3.4: The resonant wavelengths of the cavity as a function of cavity length. Dashed magenta and orange colours correspond to 50μm thick diamond modes and empty cavity modes. The solid blue curves are the cavity modes of a 50μm thick diamond sample loaded cavity.

(3.10), can be written as [49],

$$\nu_j = \frac{c}{2\pi(l_a + l_d)}(j\pi - (-1)^j \arcsin(0.412 \times \sin(j\pi \frac{l_a - l_d}{l_a + l_d}))), \tag{3.11}$$

where l_a and l_d are the optical lengths of light in air and diamond respectively. The factor 0.412 is the standard Fresnel reflection coefficient of the electric field for normal incident at the air-diamond interface. This is a one dimensional model assuming that $j >> 1$ [49].

For a laser cavity, a fundamental Gaussian cavity mode is important as it ensures maximum gain. A visualization of the deviation of the resonance conditions from the empty cavity by placing the sample studied in this thesis, i.e. 50μm thick sample, is shown in Figure (3.4). In this figure the change in the resonance conditions due to the extra boundary conditions at the air diamond interface is clearly visible, similar to the studies [49, 52].

3.1.3 Finesse and Quality factor of the cavity

Finesse (F_{cav}) and Quality factor (Q-factor) are the two important parameters that are of interest for an optical cavity. Both these parameters show how efficiently the light field, or in other words photons, can be stored in the cavity.

Finesse depends only on the reflectivity of the mirrors. Assuming both mirrors are identical, finesse can be written in terms of reflectivity (R) of the mirror as,

$$F_{cav} = \frac{\pi\sqrt{R}}{(1-R)}. \tag{3.12}$$

When the reflectivity of the mirrors tends to unity, the finesse can be written as [78],

$$F_{cav} \approx \frac{\pi}{(1-R)}. \tag{3.13}$$

Since the output intensity can be written in terms of intra-cavity intensity(I_{cav}) as $I_0^{'} = I_{cav}(1-R)$ [78], the intra-cavity intensity can be written in terms of the transmitted intensity

as [78],

$$I_{cav} = \frac{F_{cav}}{\pi} I_0'. \tag{3.14}$$

For a high finesse cavity, the finesse can be written as a ratio of FSR to FWHM (κ_{cav}) of the longitudinal cavity modes. Since the cavity modes can be tuned either via tuning the frequency or via tuning the cavity length, the finesse can be estimated in both ways. However, from equation (3.4), the FSR is $c/2l_{cav}$ as a first order approximation for simplicity. Then the finesse can then be expressed as,

$$F_{cav} \approx 2\pi \frac{(c/2l_{cav})}{\kappa_{cav}}. \tag{3.15}$$

Then using equations (3.13) and (3.15), the FWHM or the cavity loss rate can be written as,

$$\kappa_{cav} = \frac{c}{l_{cav}}(1 - R). \tag{3.16}$$

The cavity loss rate determines how long a photon can be stored in the cavity, as it is the inverse of the photon life-time inside the cavity. The Q-factor can be defined as the ratio of the frequency of the light field (ν) to the cavity loss rate of the longitudinal cavity modes and can be written as,

$$Q = 2\pi \frac{\nu}{\kappa_{cav}}, \tag{3.17}$$

which is the related to the Finesse as [78],

$$Q = jF_{cav}. \tag{3.18}$$

Equation (3.18) makes it clear that the Q-factor can be increased by increasing the finesse as well as increasing the length of the cavity. The advantage with the fibre cavity is that the micro-cavity can be formed with a really high Q-factor [47, 49].

3.2 NV$^-$ laser in the fibre cavity and associated magnetic sensing

Now with the knowledge of cavity basics that we discussed above, we can model an NV$^-$ laser in the fibre cavity and can investigate its prospects for magnetic field sensing. A fibre cavity, as we will see in the actual experimental setup in the next chapter, is a miniaturized cavity with extremely tight cavity volume. Hence, the MW driven NV$^-$ laser model introduced in reference [43] is adapted for the present study.

The idea of a laser made from the emission of NV$^-$ centres in diamond was of interest [79] even before the proposal of LTM in 2016 [43]. Although lasing from the emission of an NV$^-$ colour centres has not been observed so far, the stimulated emission of both the charge states of NV centres has been explored in the context of the NV$^-$ laser in references [45, 79–82], particularly, direct observation of the stimulated emission of NV$^-$ centres in reference [45] and the estimation of stimulated emission cross-section in references [79, 80, 82]. In this section, we start with the discussion of the stimulated emission cross-section of the NV$^-$ centre by considering the sample studied in this thesis. Then, similar to reference [43], we model the emission of the MW driven NV$^-$ centres in a diamond crystal. Using this model in conjunction with our NV$^-$ fibre cavity laser characteristics, we study the theoretical magnetic sensing performance of this platform.

3.2.1 Stimulated emission cross-section of the NV$^-$ centre

In the light induced transition, a parameter known as cross-section, associated with the system undergoing transition, sets the rate of transition along with the intensity of the light. The cross-sections of the transition for the absorption and stimulated emission are known as the absorption cross-section (σ_{abs}) and stimulated emission cross-section (σ_{se}) respectively. These cross-sections can be seen as an effective area associated with the NV$^-$ centre. Thus, one can imagine an effective model where only those photons that pass through this area interact with the NV$^-$ centre [77]. The absorption cross-section of the NV$^-$ centre has been studied in the literature and for the study presented in this thesis, we take the value from the literature. An understanding of the stimulated emission cross-section of the NV$^-$ centres is required to characterize the NV$^-$ centres as a gain medium.

The stimulated emission cross-section for a quantum emitter in free-space as a function of wavelength (λ) can be written as [83, 84],

$$\sigma_{se}(\lambda) = \frac{\lambda^4 \Gamma}{8\pi n^2 c} \xi(\lambda), \tag{3.19}$$

where Γ is the radiative decay rate, n is the refractive index of the medium and c is the speed of light. The quantity $\xi(\lambda)$, which has a dimension of inverse length, is defined such that $\int \xi(\lambda) d\lambda$ is the total probability of radiative decay. If the emission is completely radiative then this total probability is unity.

With the knowledge of Γ of the NV$^-$ centre and also for simplicity, assuming approximate quantum efficiency of 1 for the NV$^-$ centres [82, 85], the estimation of the stimulated emission cross-section only requires $\xi(\lambda)$. This parameter can be determined from the emission spectrum of the NV$^-$ centre and its quantum efficiency. From the Füchtbauer-Ladenburg equation for the stimulated emission cross-section given as [77, 80, 86], $\xi(\lambda)$ can be identified as $\frac{\lambda^5 I(\lambda)}{\int \lambda I(\lambda) d\lambda}$. Here $I(\lambda)$ is the intensity of emission as a function of wavelength, i.e. the emission spectrum. The stimulated emission cross-section, estimated from the emission spectra of the NV$^-$ centres in the sample that is studied in this thesis, is around $3.22 \times 10^{-21} \mathrm{m}^2$ for wavelength ~721 nm (see section 4.2). This is comparable with the values estimated in references [79, 80, 82]. In references [79, 82], this is estimated in essence by using an emission cross-section expression from Einstein's relations assuming a Gaussian line-shape for the emission, whereas, in [80] this is estimated using the same method that we follow in this thesis.

3.2.2 Modelling stimulated emission of NV$^-$ centres for LTM

Here we model the stimulated emission from NV$^-$ centres by considering a single NV$^-$ centre. Then the stimulated emission from the total number of NV$^-$ centres is obtained by multiplying the stimulated emission of the single centre with total number of NV$^-$ centres. For simplicity any collective co-operative effects due to the dipole-dipole interaction between the NV$^-$ centres is neglected [87, 88].

The model of stimulated emission of a single NV$^-$ centre upon excitation with a green laser similar to reference [43] is shown in Figure 3.5. Here we assume that a red wavelength is stimulating the emission of the NV$^-$ centres. States $|1\rangle$ and $|3\rangle$ are the ground and excited states' $m_s = 0$ level. Considering only one of the ± 1 states for simplicity, states $|2\rangle$ and $|4\rangle$ are the excited state's $m_s = \pm 1$ respectively. State $|5\rangle$ is the singlet state of the NV$^-$ centre. Here, we combine the two singlet states for simplicity, since the upper singlet state has negligible

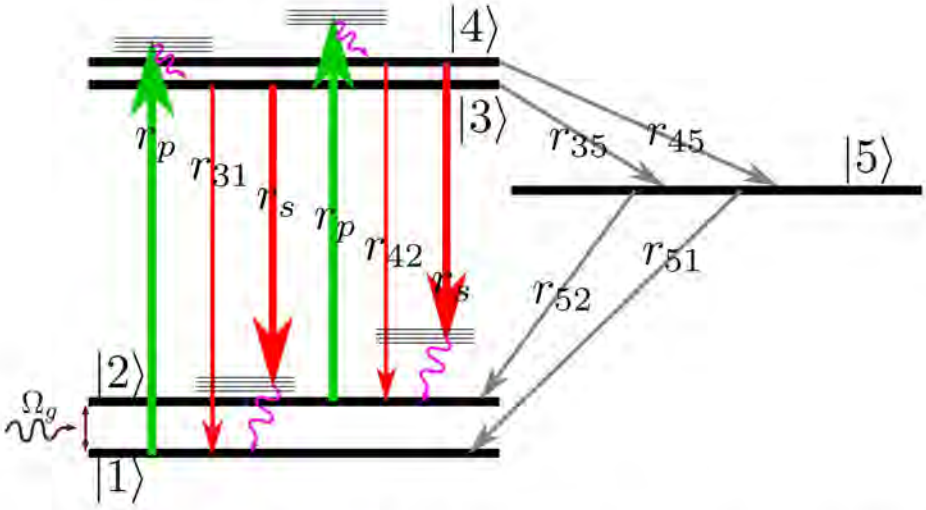

Figure 3.5: Stimulated emission model of the NV⁻ centre. The green arrows represent the non-resonant excitation of the NV⁻ centre by the green pump laser absorption. The thin and thick red arrows represent spontaneous and stimulated emissions respectively. The grey arrows represent inter-system crossing. The rates are marked to corresponding transitions. The curly magenta lines represent the phonon decay. The ensemble of black lines represent the phonon levels. The brown arrows represent the MW driving of the NV⁻ centre ground state.

lifetime compared with the lower singlet state (section 2.1.1), and also the transition between them is of no interest for the present study. The stimulated emission is spin conserving, which is assumed to be from $|3\rangle$ and $|4\rangle$ to the corresponding phonon levels of the ground state, as shown in Figure 3.5. The transition rate of the ground state phonon level is expected to be of the order of THz [43, 45]. The population of the phonon levels are expected to be small as they decay much faster than the excited state. This is the basic idea of stimulated emission and population inversion for the NV⁻ laser. Since the non-radiative decay from the ground state phonon levels to $|1\rangle$ and $|2\rangle$ are so fast and the timescales are negligible, we do not consider the phonon levels as separate levels in the model. Furthermore, we neglect any absorption of the red wavelength by the NV⁻ centres and thereby neglect any excitation from the ground state to the excited state for simplicity [43].

Then phenomenologically adding rates to the ground state master equation 2.6 (Section 2.1.2), the NV centre model can be written as,

$$\frac{\mathrm{d}p_{|12\rangle}}{\mathrm{d}t} = (i\Delta_g - r_p - \Gamma_g)p_{|12\rangle} - i\frac{\Omega_g}{2}(p_{|2\rangle} - p_{|1\rangle})\cdot \tag{3.20}$$

$$\frac{\mathrm{d}p_{|21\rangle}}{\mathrm{d}t} = -(i\Delta_g + r_p + \Gamma_g)p_{|21\rangle} - i\frac{\Omega_g}{2}(p_{|1\rangle} - p_{|2\rangle})\cdot \tag{3.21}$$

$$\frac{\mathrm{d}p_{|1\rangle}}{\mathrm{d}t} = -i\frac{\Omega_g}{2}(p_{|21\rangle} - p_{|12\rangle}) - r_p p_{|1\rangle} + r_{31}p_{|3\rangle} + r_s p_{|3\rangle} + r_{51}p_{|5\rangle}\cdot \tag{3.22}$$

$$\frac{\mathrm{d}p_{|2\rangle}}{\mathrm{d}t} = i\frac{\Omega_g}{2}(p_{|21\rangle} - p_{|12\rangle}) - r_p p_{|2\rangle} + r_{42}p_{|4\rangle} + r_s p_{|4\rangle} + r_{52}p_{|5\rangle}\cdot \tag{3.23}$$

$$\frac{\mathrm{d}p_{|3\rangle}}{\mathrm{d}t} = r_p p_{|1\rangle} - (r_{31} + r_s + r_{35})p_{|3\rangle}\cdot \tag{3.24}$$

$$\frac{\mathrm{d}p_{|4\rangle}}{\mathrm{d}t} = r_p p_{|2\rangle} - (r_{42} + r_s + r_{45})p_{|4\rangle}\cdot \tag{3.25}$$

$$\frac{\mathrm{d}p_{|5\rangle}}{\mathrm{d}t} = r_{35}p_{|3\rangle} + r_{45}p_{|4\rangle} - (r_{52} + r_{51})p_{|5\rangle}\cdot \tag{3.26}$$

Here $p_{|j\rangle}$ is the population fraction of a single NV$^-$ centre in the level $|j\rangle$. Thus $\sum_{j=1}^{5} p_{|j\rangle} = 1$. The rates r_p and r_s are light induced transitions, so that we can write them as $\frac{I\sigma}{h\nu}$, where I is the intensity of light, σ is the cross-section of the transition and $h\nu$ is the energy of a photon with frequency ν. At steady state, all the rates and populations becomes time independent. Solving equations from (3.20) to (3.26), including the summation of the population fractions, the excited state population fraction ($p_{|\mathrm{exc}\rangle} = p_{|3\rangle}+p_{|4\rangle}$) for steady state, as a function of detuning (Δ_g) is obtained analytically. Multiplying $p_{|exc\rangle}$ with the total number of NV$^-$ centres in the cavity gives the total number of NV$^-$ centres available for stimulated emission in the cavity.

3.2.3 NV$^-$ laser and LTM

Like any other laser, the NV$^-$ centres embedded into the optical cavity are expected to undergo stimulated emission induced by the spontaneously emitted photons into the cavity mode. Then the rate of change of photons in a cavity is determined by the number of photons gained by the cavity and the number of photons lost by the cavity. In an ideal case, the photon loss by the cavity can be due to absorption by any centres or mirrors etc. Since the absorption of the red laser by the NV$^-$ centres is negligible, at least ideally, the major loss factor is transmission leakage of the photons through the cavity mirrors. The gain comes from the emission by the NV$^-$ centres. Though spontaneous emission can contribute to the gain, the main contribution comes from stimulated emission. Then, the laser equation can be generally written as.

$$\frac{\mathrm{d}N_{cav}}{\mathrm{d}t} = G_{stm}N_{cav} - \kappa_{cav}N_{cav}, \tag{3.27}$$

where G_{stm} is the gain rate due to the stimulated emission, κ_{cav} is the cavity loss rate and N_{cav} is the total intra-cavity photon number. In reference [43] the gain factor is a cavity induced rate, which is in essence a cavity enhanced stimulated emission [53]. The Purcell effect on the spontaneous emission of the NV$^-$ centres, which is the modification of the spontaneous emission rates due to the cavity confinement of the emission [50, 89] is also neglected for simplicity. The G_{stm}, which is the total stimulated emission rate, is obtained by multiplying

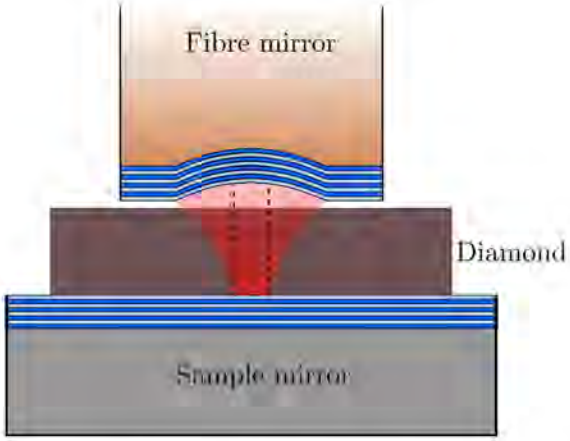

Figure 3.6: Schematic of the diamond loaded fibre cavity representing the approximation. The black dotted rectangle represents the cross-section along the diameter of the cylinder mentioned in the text. The air gap is also shown for clarity, but the approximation neglects this air gap assuming the centre of the fibre touches the sample.

the stimulated emission rate of a single NV$^-$ centre r_s with the total number of NV$^-$ centres in the excited state (total number of NV$^-$ centres in the cavity multiplied by $p_{|\text{exc}\rangle}$). Then the G_{stm} can be written as,

$$G_{stm} = \frac{c}{n}\sigma_{se}\rho_{NV}p_{|\text{exc}\rangle}, \tag{3.28}$$

where ρ_{NV} is the density of NV$^-$ centres in the sample.

A fundamental Gaussian mode of the fibre cavity is assumed for the laser construction. The important effect of the fibre cavity comes through the cavity volume that determines the pumping rate r_p. Since the fibre cavities form cavity volumes with tight beam waists roughly to a few microns [47], the pumping rate is enhanced compared with macro-cavities. At the same time, since the total number of NV$^-$ centres for stimulated emission is set by the cavity volume, the gain is limited by this number. An accurate modelling of this has to consider Gaussian features along the axis of propagation of the cavity mode as well as along the transverse plane. Also, inside the cavity there would be an air layer in addition to the sample. The Gaussian beam waist expands a bit compared with that of the empty cavity [49]. Since we are modelling a laser and the emphasis is on the qualitative feature, the cavity mode is simplified as follows. The cavity volume is approximated to have a cylindrical shape, with the beam waist as the base radius and the air gap layer is neglected with the assumption that the cavity is fully filled by the diamond crystal. A flat top approximation is assumed in the transverse plane. A pictorial representation of the cavity volume approximation is shown in Figure 3.6.

The length of the cavity is assumed to be the thickness of our sample which is $\sim 50\ \mu$m. The mode waist radius with an ideal empty cavity is $\sqrt{\frac{\lambda_s}{\pi}(Rl_{cav} - l_{cav}^2)^{\frac{1}{2}}}$ [75], where λ_s is the stimulated emission wavelength, R is the radius of the curvature. The beam waist radius of a 721 nm wavelength for an empty cavity with a length of 50 μm and with a radius of curvature of about 170 μm is around 4.2 μm. These numbers are considered due to their significance in the experiments that performed in this thesis, which are discussed in the next chapter. Then roughly, we assume that the beam waist radius for a sample loaded cavity is 5 μm. An accurate modelling with the air-diamond interface, to include the expansion of the mode waist due to the diamond refractive index can be done [49, 51]. However, we

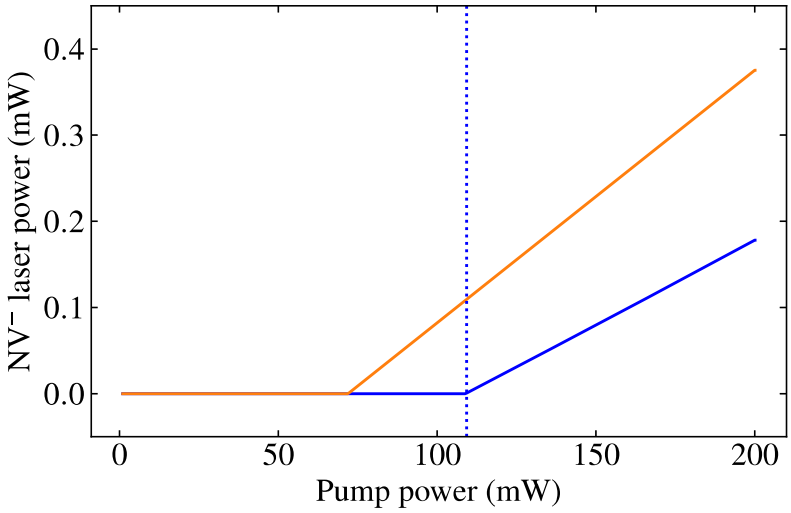

Figure 3.7: Simulated NV$^-$ laser output as a function of green pump power for different MW driving conditions. The blue curve corresponds to a coherent MW driving of the NV$^-$ ground state. The orange curve corresponds to a 0 MHz Rabi frequency, which corresponds to the MW turned off. The dotted line shows the pump power for which the sensitivity is calculated.

focus on the order of magnitudes of the quantities obtained from the calculations unlike a single-spin/single-photon regime [49, 51], i.e. in this case the laser threshold and magnetic field sensitivity of the laser etc. These values are not expected to be varied by orders of magnitude due to the approximations.

Furthermore, the cavity photon loss-rate (κ_{cav}) can be written for the diamond filled cavity from equations (3.16) and (3.13) as,

$$\kappa_{cav} = \frac{c}{2.4 l_{cav}} \frac{\pi}{F_{cav}}, \tag{3.29}$$

where the factor 2.4 is the refractive index of the diamond. For a 50 μm cavity length and a 10000 finesse, the κ_{cav} is close to 1GHz. Since the designed finesse for the 721 nm is roughly 40000 (Chapter 4), we assume a cavity loss rate of 1GHz for the calculations present in this chapter.

The ground state dephasing rate (Γ_g) and the Rabi frequency (Ω_g) are assumed to be 1 MHz [22, 43] and 10 MHz [43] respectively. Here the Γ_g and Ω_g values are considered such that the order is roughly matching with that in the references. The NV$^-$ centres can be oriented along the four crystal directions of the diamond. They can be also preferentially oriented [90]. For this calculation NV$^-$ centres in the cavity are assumed to be identical. In any case here, only the order of magnitude for the density of NV$^-$ centres (10^{23} m^{-3}) and absorption cross-sections of NV$^-$ centre, corresponding to green (10^{-21} m^{-2}) and red (10^{-24} m^{-2}) wavelengths are considered for the simplicity of the calculation. The wavelength of NV$^-$ emission considered is $\sim$ 721 nm due the property of the fibre cavity platform experimentally studied in this thesis (Chapter 4). Furthermore, the transition rates discussed in section 2.1.1 of Chapter 2 are considered.

At steady state above threshold, the gain from the NV$^-$ centres equals the loss through the cavity. The loss through the cavity mirror is the NV$^-$ laser output. Then equation (3.28) is inserted into the equation (3.27) and then the resultant equation is then solved numerically using *brentq* root finding method in python and the NV$^-$ laser output is obtained for each

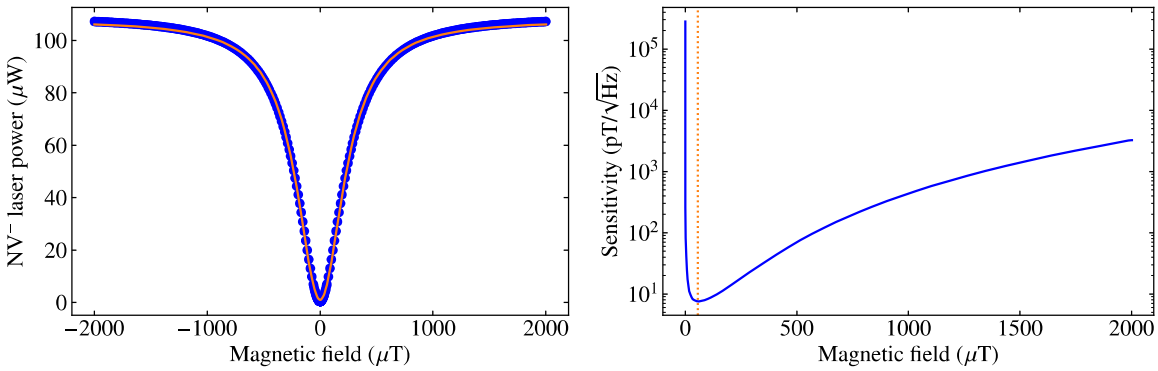

(a) (b)

Figure 3.8: (a) Response of the fibre cavity NV⁻ laser output as a function of relative magnetic field that induces detuing. The blue dots are the numerically estimated values and the orange curve is a standard Lorentian function to the numerical solution. (b) The DC magnetic field sensitivity of the laser against relative magnetic field that induces detuing. Since the Lorentian has a symmetry with respect to the zero magnetic field, only the sensitivity with respect to the positive values of relative magnetic field is plotted. The orange dotted line corresponds to the minimum sensitivity which is roughly ~7.59 pT/$\sqrt{Hz}$ for this calculation.

green pump power, using the steady state solution obtained for $p_{|\text{exc}\rangle}$. The NV⁻ laser output as a function of green pump power is shown in Figure 3.7.

The detuning (Δ_g) can be tuned either by tuning the MW or by bringing a magnet close to the NV⁻ centre. Then depending on the threshold shift of the NV⁻ laser, the magnetic field can be detected [43]. Keeping the pump power at the threshold of the resonant MW driving laser output in the Figure 3.7, we can then see how the laser output as a function of magnetic field changes. A plot of the NV⁻ laser output as a function of magnetic field present, which is a proxy for the detuning, is shown in Figure 3.8(a). Then using the equation (2.3) in Chapter 2, the sensitivity of such a laser against the external magnetic field can be determined. The DC magnetic field sensitivity as a function of external magnetic field is shown in Figure 3.8(b). The minimum DC magnetic field sensitivity calculated for the present case is ~ 7.59 pT/$\sqrt{\text{Hz}}$, which is almost three orders of magnitude larger compared to the reference [43] and almost one order of magnitude larger than the state-of-the art NV⁻ AC magnetometry sensitivity, which is 0.9 pT/$\sqrt{\text{Hz}}$ [36]. The large value for the sensitivity in the present study compared with reference [43], might be due to the combination of several factors, like the small mode volume that reduces total number of NV centres, but enhances intensity of light fields inside the cavity. The parameters that we used for the presented calculation are not really optimized here to get the minimum possible sensitivity and more careful theoretical study might be required to fully characterize such a micro-cavity laser. The motivation here was to see whether such a magnetic sensor can be achieved in fibre cavities. Such a magnetic field sensor in fibre cavities is attractive due to the compactness and conceptual simplicity. In Figure 3.8(b) an increase in sensitivity, when the relative magnetic field tends to zero can be seen. This can be attributed to the fact that when the magnetic field tends to zero, the NV⁻ laser output power tends to zero and the slop of Figure 3.8(a) also tends to zero. As a result, close to zero magnetic field, the sensor is not really sensitive. The minimum DC magnetic field sensitivity can be reached either by providing a bias magnetic field or simply by tuning the MW frequency. Moreover, here the laser output powers that are considered are really

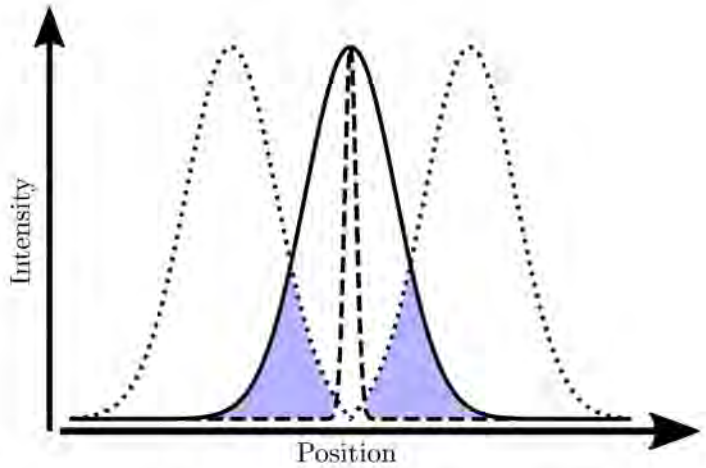

Figure 3.9: Cartoon illustration of the STED principle. The solid curve shows fluorescence due to the excitation with the diffraction limited beam spot. The dotted curve represent the doughnut beam with minimum intensity at the centre of the diffraction limited spot. The dashed curve is the resultant high resolution spot below the diffraction limit. The fluorescence contributing to the shaded area is depleted out through stimulated emission.

small compared with [43]. The reason is that since the fibre cavity mode has extremely small volume with really tight focusing, high laser output and thereby high intra-cavity power may destroy the cavity mirrors itself. For the same damage reason, the green pump power is also restricted in the calculation as evident from the figures. Since we are considering very small NV^- laser output powers, both the pump and NV^- laser power has to be stable, so that the magnetic field sensing is not affected by the power fluctuations in the lasers [43].

3.3 Stimulated emission in STED microscopy of the NV centre

So far we have discussed the stimulated emission in the context of the NV^- laser. On the other hand, in the completely different field of stimulated emission depletion (STED) microscopy [91, 92] with NV^- centres [93–96], stimulated emission is considered as the underlying mechanism.

Generally, in a microscopy technique like confocal microscopy, when the fluorescent sample is excited with an excitation light, it gives fluorescence over the entire spot of excitation. Since the excitation spot is diffraction limited, it is impossible to distinguish the emitters sitting closer together within the diffraction limited spot. In STED microscopy, another wavelength, which is red-shifted with respect to the emission peak [97] is applied to emitters after the excitation. It is important that the second beam has a doughnut shape [93–96, 98] with the minimum at the centre of the excitation spot. Then photons in the doughnut shaped intensity beam stimulate emission to the ground state. Since stimulated emission is a fast process, the slow spontaneous emission from the centre of the doughnut beam can be detected. This fluorescent spot is smaller than the diffraction limited spot. As a result the resolution of the imaging is enhanced through the process of stimulated emission. A cartoon illustration of the STED principle is shown in Figure 3.9.

STED microscopy with NV^- centres and spin manipulation of the NV^- centres detected through it is also studied[93–96]. However, in essence STED microscopy is pushing those

excited NV^- centres into a dark state [84, 99], which in the case of stimulated emission would be the ground state. Since STED is based on depleting the fluorescence of the NV^- centre through stimulated emission, rather than collecting the stimulated emission, possibilities of other dark channels like ionization should be considered [81, 99, 100]. The inter-play between the charge state dynamics and stimulated emission of the NV^- centre is an active problem that has to be addressed more [81, 100].

The stimulated emission cross-section for the NV^- centres studied in the context of STED is comparable [84, 101] with the same determined in the context of the NV^- laser that we described in the previous section. Though the stimulated emission cross-section suggests that the stimulated emission is the underlying mechanism for STED [84], recent studies in references [81, 100] suggest that when an additional near IR (NIR) wavelength is used along with a green laser, the charge state dynamics change. For STED microscopy, it does not really matter what the underlying mechanism for the depletion is. Even if spin manipulation experiments are done from the STED imaging method, the charge dynamics of the colour centres at the centre of the doughnut beam is not expected to be altered.

3.4 Charge state switching of the NV centre

The process of charge state switching refers to the inter-conversion of NV centres between its neutral and negative charge states. Unlike for STED microscopy discussed in the previous section, the photo induced charge state switching of NV^- centres may affect the conditions to achieve lasing from NV^- centres and thereby affects LTM. For instance, a reduction of the number of NV^- available for the laser generation can inhibit stimulated emission for lasing.

The neutral charge state of the NV centre, NV^0, which is a spin half system, is also a fluorescent centre, but has a different level structure than its negative charge state counter part [22]. This centre consists of a doublet ground, a doublet excited state and a quartet meta stable state [22]. The NV^0 has a ZPL around $\sim$ 575 nm and a phonon side-band spanning from approximately from 575 nm to 700 nm [102]. Unlike the NV^- centre, the NV^0 with doublet ground and excited states is not really explored in the literature and considered not so interesting for magnetic sensing application by itself. However, very recent results reported in reference [103] observe the fine structure of the NV^0, representing a strong step towards the exploration of NV^0. The photo-induced charge state switching between NV^- and NV^0 makes the NV^0 relevant in NV^- studies. In fact some studies were reported that harness the charge state switching for enhanced readout due to the spin dependence of this process [104–106]. We will not examine the details of such studies as it is beyond the scope of the present thesis.

The mechanisms of charge state conversion are not fully clear yet and under active research [81, 102]. In fact, these processes can vary depending on the diamond sample [102, 107]. Charge state conversion is typically a two-photon process, i.e. it happens with the absorption of two photons [99]. However, the availability of singlet nitrogen (N) in the diamond crystal that is within 5 nm to the NV centres can alter this process [102]. Here we discuss the process of ionization and recombination based on the simplified picture relevant for the present thesis. We take the current understanding of charge state conversion from references [81, 99, 100, 102, 106, 108]. The emphasis is on the ultimate loss of NV^- centres available for the NV^- laser generation due to the photo-induced process, rather than the absolute mechanism of this loss channel. However, the author acknowledges the fact that the absolute mechanisms of the charge state switching may influence the loss of NV^- centre in the end. More dedicated studies are required in order to make concrete comments about it

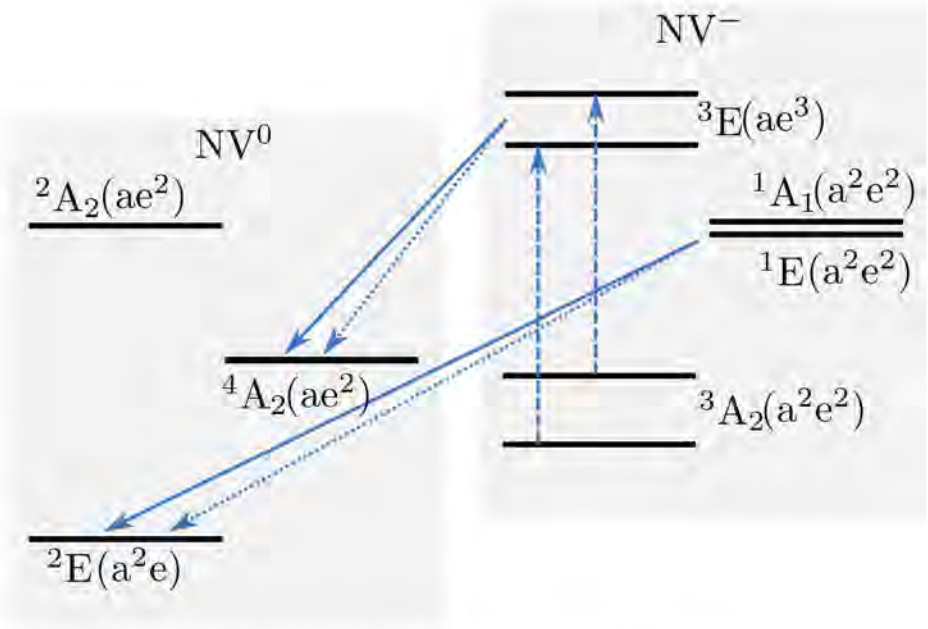

Figure 3.10: Schematic of the ionization of NV^- centre. The dashed arrows represent the first step of the ionization, i.e. excitation of the NV^- centres. The solid arrows or dotted arrows represent the photon induced ionization and the tunneling process from the NV^- centre to NV^0 centre. For simplicity and clarity, only the photon induced and tunneling process are shown and no other internal transitions of the centres are shown.

and those studies are beyond the scope of this current thesis.

3.4.1 Ionization of the NV^- centre

A schematic of the ionization process in a simplified manner is shown in Figure 3.10. For a better understanding of the process, the electron molecular orbitals 'a' and 'e' are denoted with each level [22, 102]. Both the molecular orbitals 'a' and 'e' can be occupied in the band gap of the diamond. The 'a' is a non-degenerate state that can accommodate two electrons maximum, but the 'e' is two degenerate levels which can thus accommodate a total of four electrons together [22, 102]. The ionization process happens basically in two steps. In the first step, the NV^- centre is excited with the absorption of a photon. Then in the second step, the charge state switching from the NV^- centre to the NV^0 centre happens.

The first step we have already discussed in this chapter in great detail. The typical excitation laser wavelength, which is the green laser wavelength ($\sim$ 532 nm) can induce this process. However, red NIR laser wavelengths can induce only weakly this process, since the photons of those wavelengths do not have enough energy to do so. On the other hand, the second step is not fully understood yet [81]. From the molecular orbital notation it can be seen that such a transition is possible if an electron is taken off from the NV^- excited state. Where the electrons goes is beyond the scope of the current study. In diamonds with high density of NV centres, the electron can potentially contribute to recombination process. The experimental study in reference [81] rules out the possibility of the ionization transition for their observations from the excited state of the NV^- centre to the excited state of the NV^0 centre [99, 109], at least for their data. However, in the simplified model in reference [81], they consider the transition to be from the excited state of the NV^- centre to the ground state

of the NV^0 centre. Studies reported in references [106, 108] considered that this ionization process happens directly from the excited state of the NV^- centre to the ground state of the NV^0 centre. However, from the molecular orbital notations, we can see that such a transition requires removal of an electron as well as transferring the electron from the 'e' to 'a' and since this is a two electron process this transition is not favourable [102]. The favorable transition from the excited state of the NV^- is the transition to the meta-stable state ($^4A_2$) of the NV^0, since it only requires removal of an electron and then the NV centre can relax down to the ground state of the NV^0 [82, 102]. The resultant transition however, looks like a process transferring the NV^- centre from the excited state to the ground state of the NV^0. Furthermore, the excited NV^- centre that does the ISC transition to the singlet levels can also transfer from the NV^- to NV^0 [81, 102, 110]. While the tunnelling process can happen for such a transition, the photo-induced transition is typically studied as an NIR induced transition [81].

Typically though, this ionization transition itself is not considered as a spin dependent process, the spin dependency comes through the uneven shelving of the NV^- centre population from the excited states $m_s = 0$ and ± 1 to the singlet states [104–106]. However, a recent study in the nano-diamond sample shows that these ionization transitions are spin dependent with roughly 80% weighing on the transition from the $m_s = 0$ state [100].

3.4.2 Recombination of the NV^0 centre

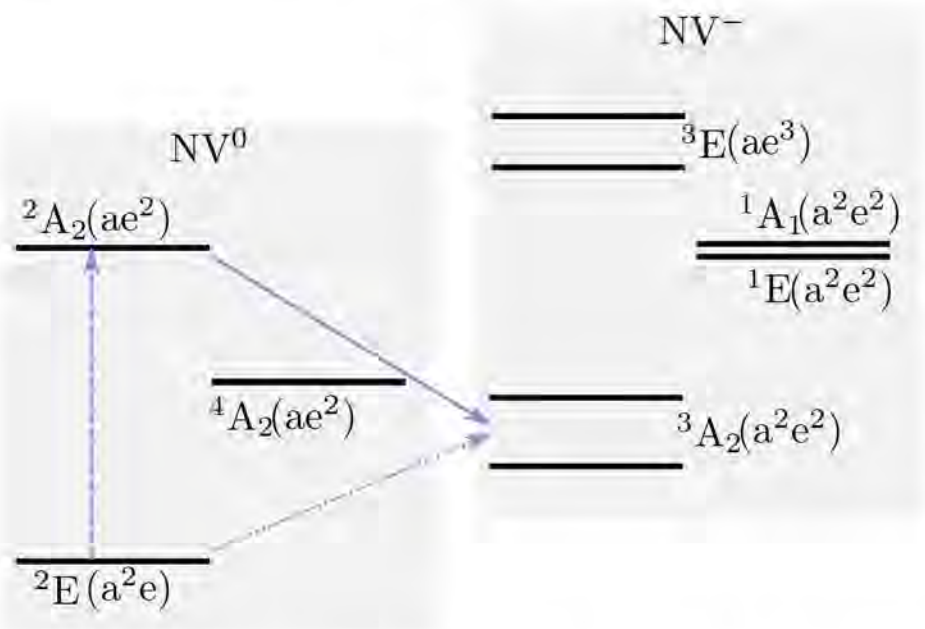

Figure 3.11: Schematic of the recombination of NV^0 centre. The dashed arrows represent the first step of the photo-induced recombination, i.e. excitation of the NV^0 centres. The solid arrows and dotted arrows represent the photon induced ionization and the tunneling process from the NV^0 centre to NV^- centre respectively. For simplicity and clarity, only the photon induced and tunneling process are shown and no other internal transitions of the centres are shown.

A schematic of the recombination process is shown in Figure 3.11. This process is also typically a two photon process. The first process is the excitation of the NV^0. The second step is to transfer the NV^0 from the excited state to the ground state of the NV^- by adding an

electron. This additional electron can come from a singlet nitrogen, by ionizing it or from an NV^- centre that is being ionized [102].

The first step is only possible with a wavelength equal to or below 575 nm, which is the ZPL of the NV^0 centre. The NIR wavelength cannot excite NV^0, since the photons corresponding to those wavelengths do not have enough energy for that. As a result the first step for the recombination cannot happen with the NIR wavelength. However, they can induce the second step. Thus NIR light alone cannot induce recombination, but along with green light, which is the typical excitation wavelength for NV centres, it can enhance the recombination process. Unlike the ionization process, the recombination process does not favour any of the particular spin states of the NV^- triplet ground state [100].

4

Realization of laser amplifier due to the stimulated emission of NV centres in open fibre cavities

This chapter discusses the experiments and the experimental observation of laser amplification due to the stimulated emission of NV centres in the fibre cavity apparatus. The chapter starts with the construction of the fibre cavity platforms for the experiments and the characterization of the cavity apparatus in section 4.1. Then in the section 4.2 ,we discuss the diamond sample used in the experiments. In this section, we estimate the stimulated emission cross-section for the sample studied. In section 4.3, we discuss the automated experiments and the observation of laser amplification in the experiments. A qualitative model discussed in this section including the charge state switching enables us to interpret that the laser amplification is due to the stimulated emission of NV centres. Finally in section 4.4, we briefly discuss the implication of the results for LTM with an active NV^- laser.

4.1 Fibre cavity platform

The experiments performed in this thesis were done with fibre cavity platforms [47]. The cavity was constructed between a curved mirror at the tip of an optical fibre and a flat mirror. All the cavity physics discussed in the Chapter 3 is applicable to the fibre cavities, and the most important part of the fibre cavity is the fibre mirror. We start the discussion about the fibre cavity platforms by discussing the fibre mirrors and their features, then we discuss the construction of the cavity. Following this, we discuss the performance of the fibre cavity platforms.

4.1.1 Fibre mirror

The curvature for fibre mirrors were laser machined employing a CO_2 laser within the QMAPP group. The tip of the optical fibre (IVG fibres, Cu 600) was ablated using controlled CO_2

(a) (b)

Figure 4.1: Images of the fibre tip (obtained using Laser Interferometry Imaging System at QMAPP group [111]) (a) before and (b) after CO_2 laser machining. The interference rings at the centre of the fibre tip represent the curvature of the tip produced by the laser machining.

laser pulses producing the desired curvature [111]. An image of the fibre tip before and after the laser machining process is shown in Figure 4.1. The machined fibre tips were coated with Distributed Bragg Reflectors (DBR) depending on the mirror specification required, by Laseroptik GmbH, Germany.

Two batches of fibre mirrors were produced by experts within the QMAPP group before the author started the PhD work presented here. The first batch of fibres were employed in the study of cavity-polaritons using quantum well structures [113]. The second batch of fibre mirrors were designed for studying diamond colour centres, and were used for the first time in this current project.

Figure 4.2 shows a standard transfer matrix simulation of the transmission of the cavity mirrors [112] and the expected finesse of the cavity as a function of the wavelength. From Figure 4.2, we can see that the maximum reflectivity band or the high finesse band are approximately $\sim$ 600 nm to $\sim$ 680 nm and $\sim$ 700 nm to $\sim$ 800 nm. One of the ideas for this particular coating for the mirrors is to study cavity Quantum Electro Dynamics (Cavity QED) with diamond colour centres like the NV and Silicon-Vacancy (SiV), with ZPLs around 637 nm and 738 nm respectively [48–50, 52, 114, 115].

4.1.2 Mechanical design and construction of the fibre cavity platforms

In the work presented here, the interest is to study the stimulated emission and thereby lasing from the NV centres in a bulk diamond sample at room temperature. The key challenge is the construction of fibre cavities that are mechanically stable. The basic idea of our cavity construction is to place a flat mirror with a DBR coating identical to the fibre mirror at the bottom and then approach it with the curved fibre mirror from the top. In this way, the sample can be loaded into the cavity by placing it on top of the bottom mirror.

Fibre cavities are more susceptible to external vibrations due to their extremely small cavity volumes and light weight, as compared with conventional macroscopic laser cavities. Over the time of this PhD work, the mechanical design of the fibre cavities were optimized over a few generations. In the previous version of the cavity the fibre mirror was attached to

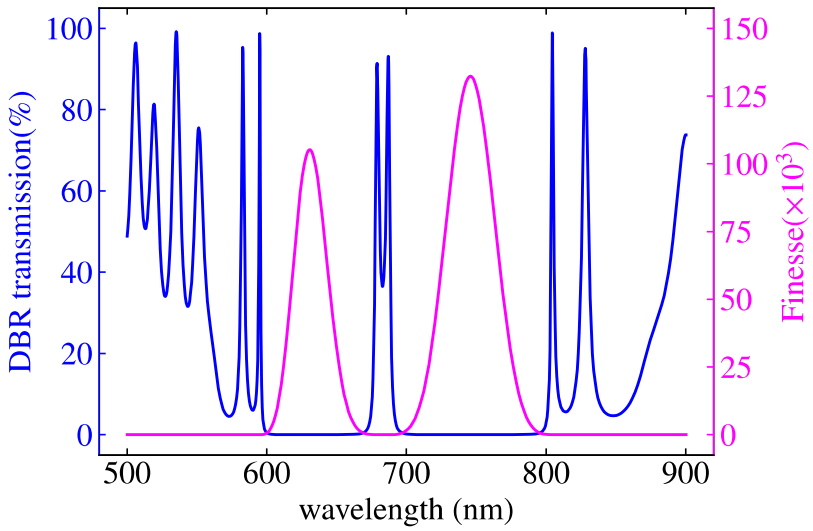

Figure 4.2: Simulation of the transmission of the DBR coating and expected finesse of the cavity using standared transfer matrix approach [112]. The blue curve corresponds to the transmission and the magenta curve corresponds to the finesse of the cavity. For this simulation an s-polarization of the light is assumed.

a fixed adapter plate hanging from a fixed stage like a cantilever, through an attocube z-stage (ANPZ101). The cavity length was tuned in this previous version by means of the attocube stage using attocube drivers (ANC 300, where ANM300 is the module).

A picture of the current geometry of the fibre cavity platform is shown in Figure 4.3 (a). The key components of this cavity geometry are as follows. The fibre mirror was attached to a shear piezo and thereby to a Z-stage (Newport) using custom built adapter plates. In the current design the adapter plates were designed deliberately to reduce any cantilever effects as much as possible. In the version in which the amplification results are shown in this thesis, coarse alignment of the cavity length was done through the Z-stage and fine tuning of the cavity length was done using the shear piezo (NAC2402-H3.4-A01). A picture representing how the shear piezo was typically glued is shown (used a different shear piezo in the picture) in Figure 4.3 (b). Only freedom along the z-axis was provided for the fibre mirror in contrast to our previous designs. This was to ensure that the optical axis of our cavity, which is set by the fibre mirror, stays the same throughout our measurements. The fibre was glued on a V-groove chip which was glued on the adapter plate mounted on the shear piezo. The fibre was glued in such a way that the curved DBR coated tip protrudes out of the V-groove chip. A picture showing the glued fibre is shown in Figure 4.3 (c).

A gimbal mount (Thorlabs) was used for mounting the sample mirror, allowing fine tuning of the cavity alignment in order to compensate for the imperfection in the gluing of the fibre. This was mounted on an X-Y stage to provide movement to different spots on the sample without changing the optical axis. A picture showing the cavity working is shown in Figure 4.3 (d).

4.1.3 Aligning the fibre cavity platform

Once the cavity was mounted, the next challenge was to optimally align the cavity. This requires fine control of the cavity length using the shear piezo. This setup uses a National Instrument (NI) card (NI USB-6259) interfaced to the computer using the *Python* programming

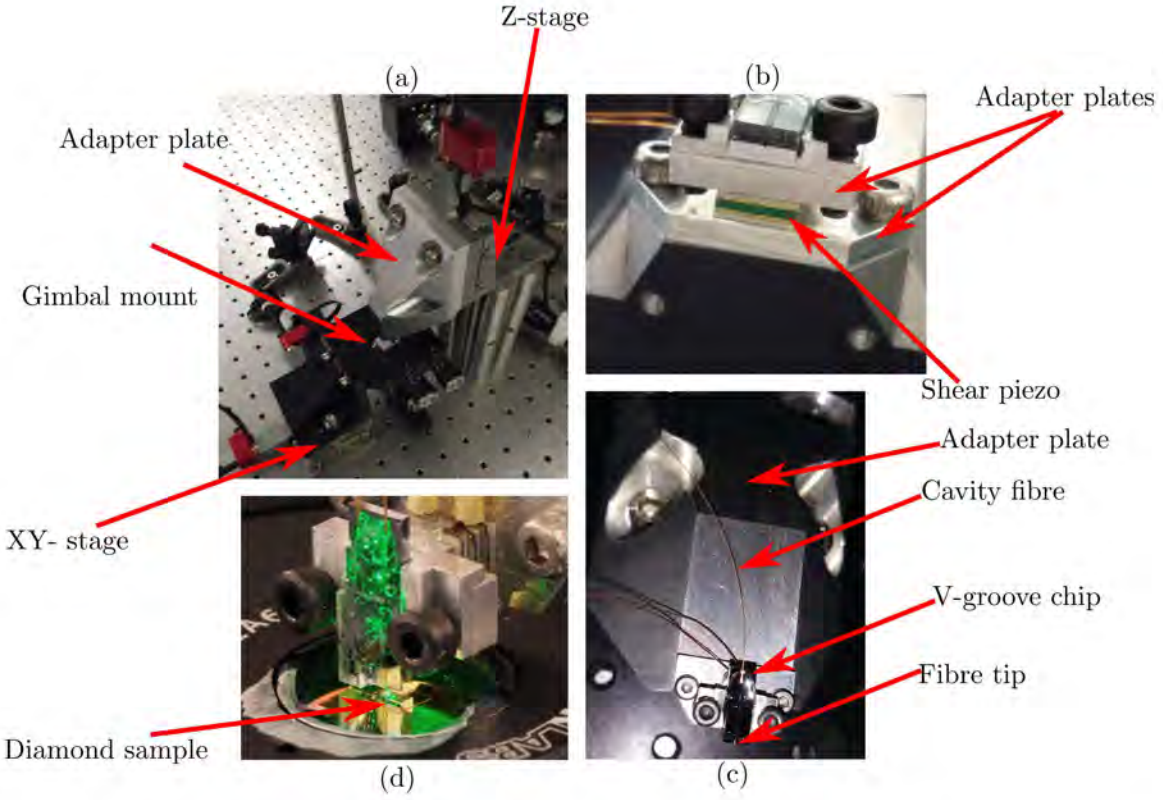

Figure 4.3: Mechanical design and construction of the fibre cavity platforms. (a) Picture showing the geometry of the fibre cavity platform. (b) Picture showing the incorporation of the shear piezo for the cavity length tuning. (c) Picture representing the gluing of the fibre mirrors. (d) Picture showing the fibre cavity in operation.

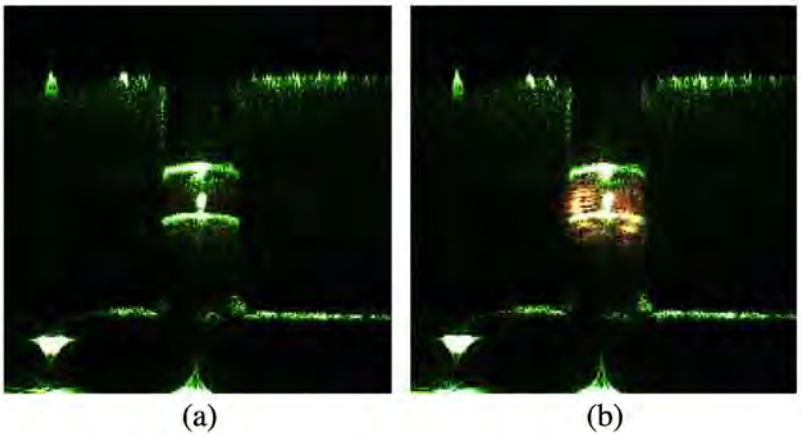

Figure 4.4: A typical cavity and resonance imaging through the side camera. One of the apparent fibre-tips is the fibre mirror itself and the other is its reflection in the sample mirror. Both the pictures are taken while pumping a green and a red laser wavelength through the fibre mirror and ramping the cavity length. (a) Off resonant cavity with faint red flash (almost invisible). (b) On resonant cavity with clearly visible flashes of red light due to the scattering of the strong intra-cavity field.

language.

In order to make sure that the fibre was not touching the sample or the sample mirror, a camera (Thorlabs DC1645C HQ) was mounted with a standard telescopic setup. The focus of the telescopic setup was aligned roughly close to the top of the sample mirror where it intersects with the cavity axis. Looking through the side camera, the fibre was brought close to the sample mirror. A view of the cavity through the side camera is shown in Figure 4.4. The cavity length was naively aligned, neglecting the curvature of the mirror, through the side camera by considering the diameter of the fibre mirror as a reference.

The key challenge in aligning the cavity was to align the sample mirror whilst compensating the tilt of the fibre tip due to the imperfection in the manual gluing of the fibre. As mentioned above the gimbal mount is useful for this purpose. However, in order to optimize the cavity a reference signal, which is some amount of cavity transmission, is required. The cavity transmission happens only if the cavity length matches the resonance condition of the light field that we are pumping into the cavity, as we discussed in the previous chapter. This can be done in two ways. The first one is to pump a broad White light source through the cavity so that the wavelengths matching the resonance conditions transmit through the cavity. Then the tilt of the cavity can be optimized by looking at the transmitted light. The second one is to pump a monochromatic light through the cavity and then constantly change the cavity length while monitoring the transmission of the cavity. This second method was most typically used in aligning our fibre cavity setup, with the cavity length tuned back and fourth using voltage ramps.

Typically a photo-diode was used in front of the collimated cavity output to detect the cavity transmission. The cavity transmission signal with the cavity length ramping was also used in the cavity finesse measurement which is discussed in the following subsection.

Interestingly, we observed the cavity resonance through the side imaging camera as shown in Figure 4.4. Practically there is always some scattering losses from the cavity which can be monitored through the side camera. When the cavity is on resonance, the intra-cavity light field is intense and so we could visibly see some flashes of light, which is really faint when the cavity moves off resonance. Although this is proportional to the scattering losses, it hints that the tilt alignment is in right direction.

By placing a standard Thorlabs camera in the cavity transmission, we monitor the transverse cavity modes as shown in Figure 4.5. For this we use a laser around 770 nm wavelength, which is not perfect for a high finesse cavity, but ensures enough transmission for a clear cavity mode imaging. Since these images are matching with the standard cavity mode simulation that is shown in Figure 3.3 in Chapter 3, the fibre cavity setup works as expected.

4.1.4 Characterising the fibre cavity platforms by finesse measurements

Cavities are mainly characterised by measuring their finesse. The finesse of the cavity is estimated by obtaining the Free Spectral Range (FSR) and spectral width (FWHM) by tuning the cavity length [47, 49, 116]. The best way to measure the finesse accurately would be by producing a side-band and using the side-band as a ruler for measuring the line width of the cavity mode [116]. However, no hardware was available to produce detuned sidebands on the laser. Instead, an easy method simplified from the one given in [47, 49] was used to estimate cavity finesse and judge whether it might be sufficient for use as a laser resonator. A wavelength for which the finesse was measured, pumped into the cavity. The cavity length was tuned back and forth by using the voltage ramps. The cavity transmission was monitored through an oscilloscope. The photo-diode signal due to the cavity transmission was typically

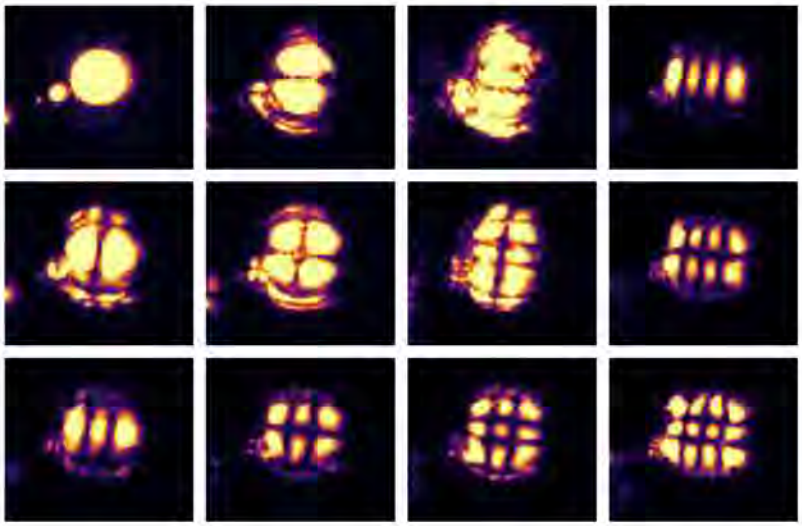

Figure 4.5: Transverse cavity mode profiles of the fibre cavity platform obtained by tuning the cavity length. The wavelength used was around 770 nm. The images were recorded for an arbitrary rotation of the camera. The images resembles the simulated results shown in figure 3.3 in Chapter 3.

measured through any standard oscilloscope. However, for high resolution of the signal, we used an oscilloscope from Agilent Technologies (DSO-X-6004A).

A representative finesse measurement data from the earlier version of the empty fibre cavity setup constructed during the course of this study is shown in the Figure 4.6. The FWHM and the FSR are obtained by fitting the data with a Lorentzian line-shape function as shown in (a) and (b) in the Figure 4.6. The FSR is obtained by taking the difference in the peak position obtained from the Lorentzian function. The X-axis is time, which stands as a proxy for the cavity length. Since the Finesse is a dimensionless number that is obtained from the ratio of FSR to FWHM, the units of both these parameters must match, but are otherwise irrelevant. The maximum value of finesse obtained is around 4000 for a wavelength of ~ 754 nm, for which the designed finesse is of the order of 10^5. This difference can be attributed to the parameter D in equation (3.2) that accounts for the intra-cavity losses, such as scattering losses, external vibrations, etc.

When the empty cavity was loaded with the diamond sample the empty cavity typically became of lousy quality as expected. These losses can be mainly due to the scattering at the air-diamond interface due to the surface roughness of the diamond sample. Absorption by the defects centres like NV centres can be another loss channel. Scattering of the light inside the diamond by the NV centres for samples with high density of NV centres can be another cause for the reduction in finesse. One of the important factors is the alignment of optimally aligning the cavity after loading the sample. For an empty cavity, the fibre mirror can reach close to the sample mirror. Hence the tilt alignment of the cavity is easy. However, for a sample loaded cavity the thickness of the diamond sample limits the tilt alignment. A good finesse measurement which is comparable with the empty cavity finesse measurement shown in Figure 4.6, with the sample loaded cavity is shown in Figure 4.7. This was taken with a laser around 720 nm.

Comparing with the empty cavity, the transverse modes are clearer for the sample loaded cavity. This can be attributed to the fact that for an empty cavity, the cavity alignment can be optimized much better than the sample loaded cavity. When the cavity was aligned well, the fundamental mode is expected to dominate over the all other transverse and the FSR is

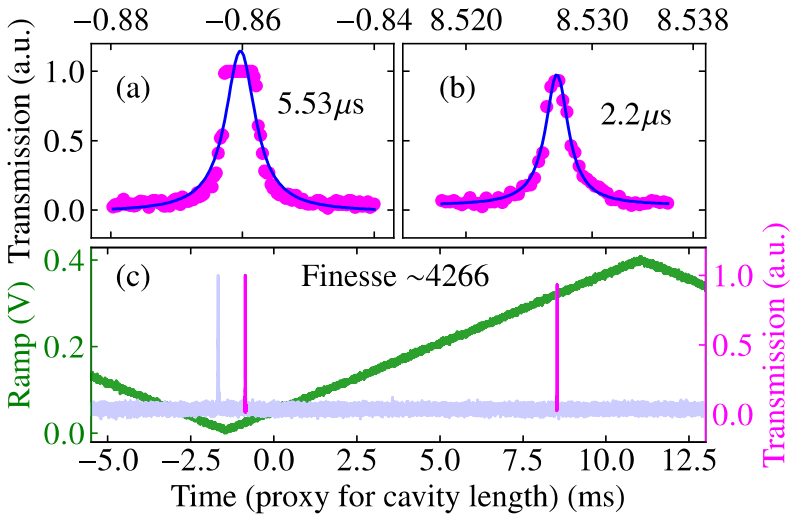

Figure 4.6: A representative figure of finesse measurement of an empty cavity. (a) and (b) shows the Lorentzian function fitting of the data point in the peak highlighted in (c). The FWHM is annotated in (a) and (b). (c) shows the free spectral range during the cavity length tuning. The peak in (a) is clipped due to the saturation in the oscilloscope and thus the FWHM is not accurate, but the fit gives peak position. The finesse is estimated using the lower bound of the FWHM in (b).

expected to be clean as we saw in the empty cavity case. However, due to the losses and the limitation in aligning the diamond loaded cavity, the fundamental mode was not dominating as in the empty cavity. The FSR is determined by taking the same peak with maximum transmission in the repetition of the three peaks as highlighted in the Figure 4.7(c). The FWHM obtained is roughly an order higher than the empty cavity. The resultant finesse, i.e, roughly 257, was an order of magnitude lower than the one obtained with the empty cavity. Like the empty cavity measurement, this comparable finesse measurement was captured in the cavity geometry with the attocube piezo state. It is really hard to make a one to one comparison across different generations of the cavities, as the fibre mirror, a deciding factor, changes in all the versions. However, it can be interpreted that the loading diamond limits the finesse of the cavities in general.

The finesse measurements presented in this section were performed in detail for an earlier version of the cavity. In the later iterations of the cavity the sole emphasis was amplification measurements in search of lasing, and finesse measurements were omitted in order to reduce risk of dust and damage accumulating on the cavity fibre tip. However, the finesse measurements in the early cavity provide an insight into the limitations of the fibre-cavity apparatus, and it is reasonable to assume that the reduction in finesse by loading the diamond sample for the present study, apply consistently across the batch of cavity fibres.

In order to reach the laser regime, the Q-factor of the cavity is needed to be higher. That means the cavity has to trap almost all the spontaneously emitted photons of the NV centres inside the cavity for a long time. This requires a cavity with really good finesse. Fibre cavities loaded with diamond samples having thickness of roughly 10 micron have already shown experimental finesse of the order of few 10000 [49]. In the experiments present in this thesis, as mentioned earlier the sample reduces the finesse from that of an empty cavity. However, sample in the present study is almost 5 times thicker than in the study mentioned above. Comparing the surface roughness of less than 0.2 nm of reference [49], the surface roughness of the present sample as we see in the section is almost two times higher, which

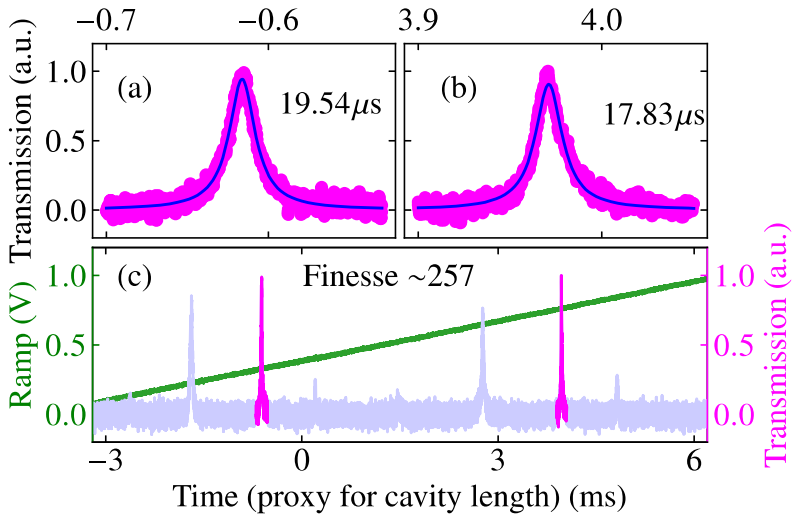

Figure 4.7: Representative finesse measurements with the diamond sample loaded fibre cavity. (a) and (b) are the cavity transmission peaks highlighted in (c). Corresponding FWHMs are shown annoted in (a) and (b). In (c) three peaks repeated with cavity length tuning are interpreted as transverse modes.

implies a significant scattering loss at the air-diamond interface in the present study. The high concentration of the NV centres could be another major factor in the current sample. However, this loss is unavoidable as these centres are required as the emitters for the laser. Another important aspect is that the red laser with which we mainly determine the finesse can induce ionization of the NV^- centres to NV^0 by stripping an electron away from the negative charge state [81, 99, 100]. How much the finesse is going to be affected in the presence of such electron movement through the sample is an open question. In fact during the course of work presented in this thesis, the author was only able to study one sample. Ideally a sample dependence study of the finesse would require to understand the challenges involved in enhancing the finesse of such an NV rich diamond sample.

The clipping in Figure 4.6(a) happened due to the saturation in the oscilloscope during the measurement. The saturation in only one of the peaks, as is evident from Figure 4.6, is due to the difference in the cavity transmission for the corresponding voltage applied to the cavity length tuning. However, the transmission determined by the detuning of the cavity length from the length corresponding to the perfect resonance and this is determined by the resolution of the cavity length tuning. On the other hand, when the cavity approaches resonance by optimizing the tilt of the cavity, it becomes very sensitive to the external noise. The cavity length drift due to external noise on top of the cavity length resolution determines the difference in transmission observed for different resonance voltages. The resolution in cavity length tuning is a technical issue that can be changed. In the latest version of the cavities, a shear piezo was used to tune the cavity length to provide almost a continuous motion than steps as in the case of attocube piezo stages. Then the external noise became the open challenge.

4.1.5 Noise characterization of the fibre cavity platform

To understand coupling of external noises to our cavity platform, a noise analysis was done. The laser used for this analysis was around 720 nm so that the observation of the cavity mode is relatively easy, since the designed finesse is close to 40000. The voltage for controlling

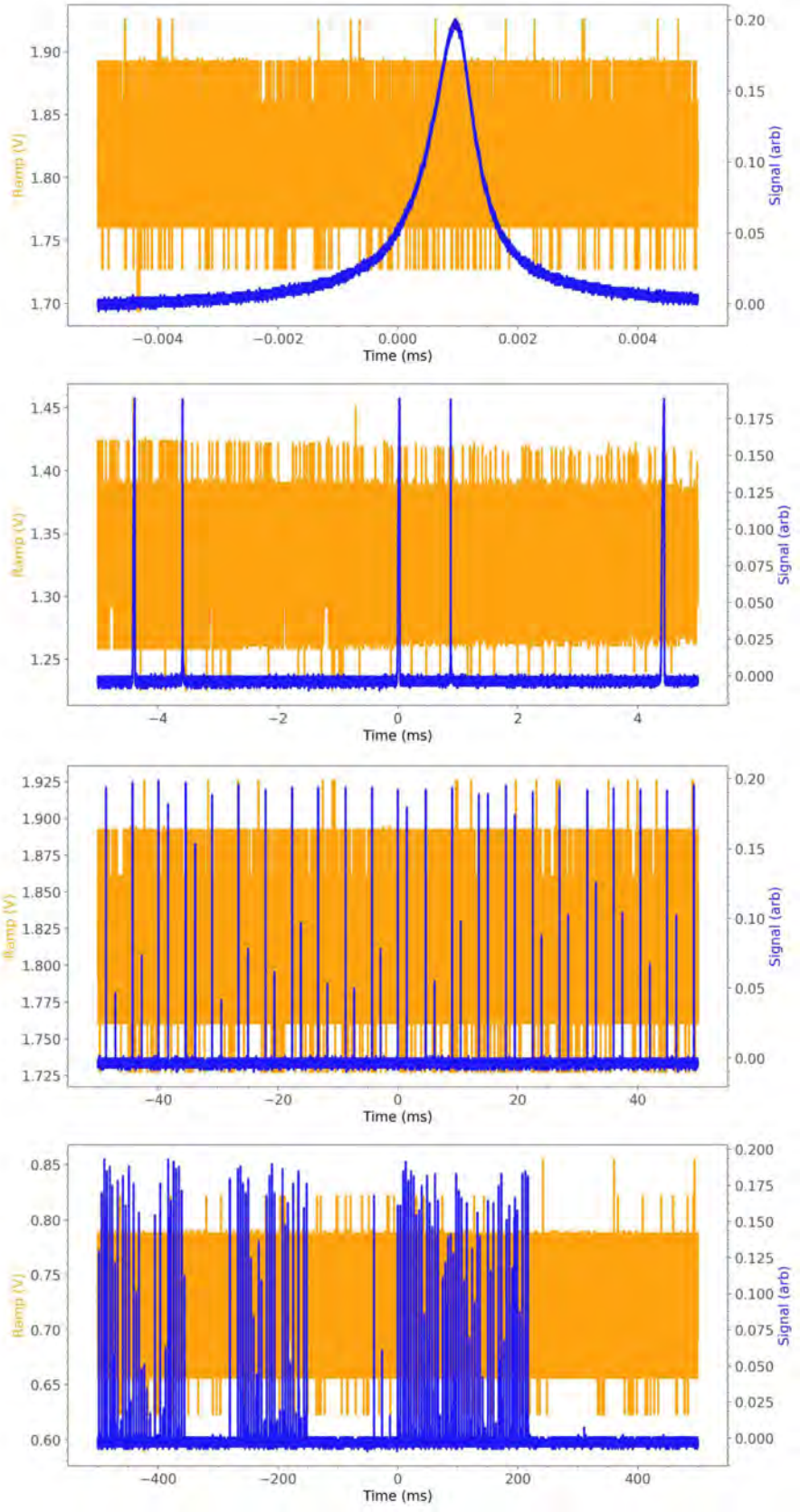

Figure 4.8: Noise analyses at various time scales. The cavity length ramp voltage that changes the cavity length (shown in orange colour) was static and the signal peaks (shown in blue colour) are modifications of the cavity transmission due to the external noise coupling to the cavity.

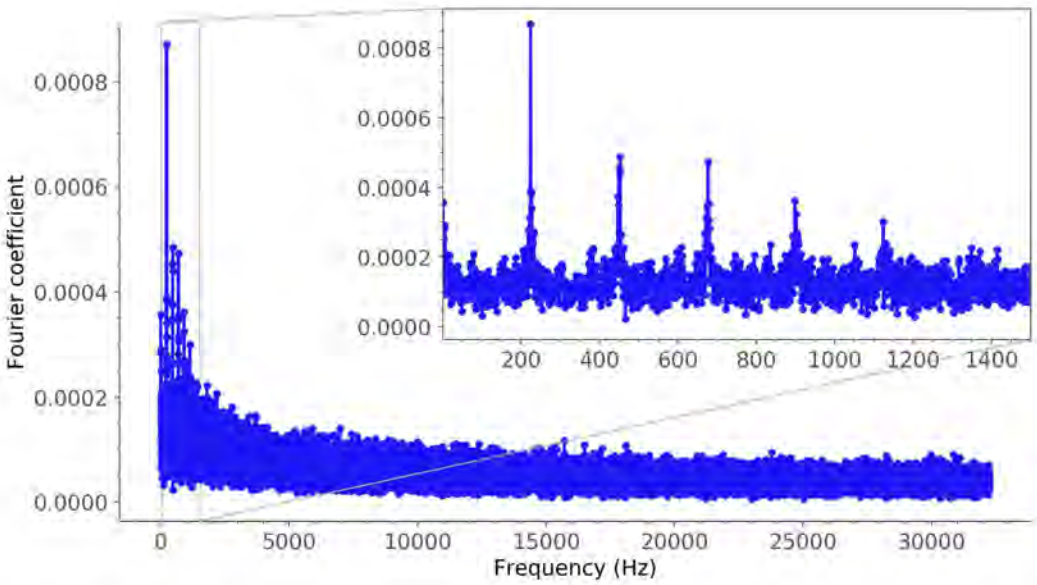

Figure 4.9: Noise spectrum showing a strong peak at 225 Hz and the harmonics. The Y axis is the Fast Fourier transform of the cavity transmission.

the cavity length was tuned manually and kept static when a cavity resonance was seen. The cavity transmission was monitored through an oscilloscope. Then the drift in the static cavity due to the external vibrations were monitored for different time scales ranging from a few micro-seconds to a few seconds. A few representative recordings of this noise for different timescales are shown in Figure 4.8.

The discrete Fourier transform of the cavity transmission as shown in the representative Figure 4.9 is obtained to understand the frequencies coupling into the cavity. A harmonic structure of frequencies in milli-second timescales were observed. The strongest characteristic frequency that we observe is 225 Hz. Figure 4.9 corresponds to the longest timescale in Figure 4.8, which shows harmonics with the 225 Hz frequency. This characteristic frequency of 225 Hz is an acoustic frequency and can be attributed to the acoustic noise in the laboratory.

4.2 Diamond sample with high density of NV centres

The diamond sample for the present study was prepared and processed by our collaborators Hiroshi abe and Takeshi Ohshima (National Institutes for Quantumand Radiological Science and Technology, Takasaki, Gunma, Japan), Thakeshi Yatsui (School of Engineering, University of Tokyo, Japan) and Jan Jeske. The diamond sample is a commercial (E6) type 1b HPHT sample with [100] orientation, which was electron beam irradiated (at 2 MeV) to a fluence of 10^{18} cm^{-2}, at 740°C temperature (to achieve in-situ annealing that improves NV creation [117] to 1.7 ppm concentration) and in vacuum. The NV concentration is expected to be around 3×10^{17} cm^{-3}, since this much concentration is achieved in similar samples [117]. The diamond sample was laser cut and polished to 50μm thickness. Then a surface roughness of 0.4 nm was achieved by optical "superpolishing" using a 213 nm pulsed laser with pulse power of 24 μJ under oxygen atmosphere.

A photograph of the sample is shown in Figure 4.10(a). The dark pigment of the sample

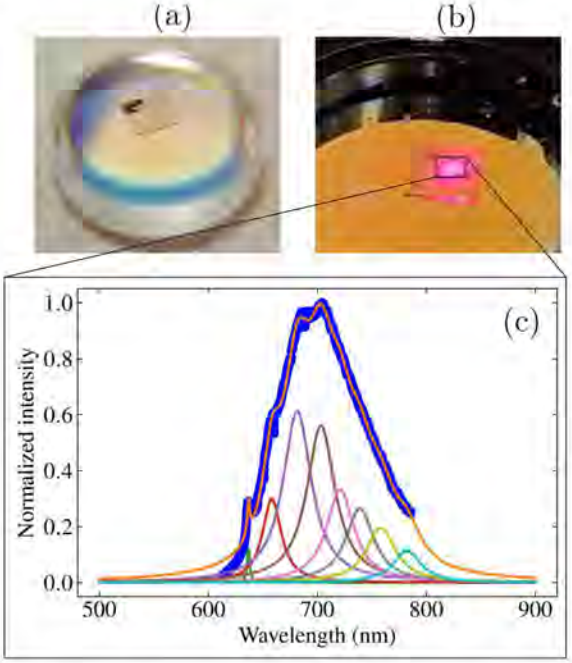

Figure 4.10: (a) Photo of the diamond sample placed on the mirror. (b) Red fluorescence emission from the NV centre with green light illumination. The green light was blocked using a notch filter for taking the photo. (c) Spectrum of the NV centre from our sample for green light illumination of the sample. The blue dots are the experimentally obtained spectrum. The orange curve is the fit using a convolution of 8 Lorentzian functions for the Zero-Phonon line (ZPL) and 7 phonon levels. The individual Lorentzian functions are also shown. See the table shown in the text for fit parameters.

visually suggest that it contains high density of impurity atoms. In the photograph 4.10(b), the bright red fluorescence is clearly visible. An emission spectrum normalized to the peak intensity of the fluorescence from the diamond sample, for an arbitrary green pump power, was obtained as shown in Figure 4.10(c). This spectrum matches with the NV^- emission spectrum with a ZPL around 637 nm. This spectrum is fitted with 8 Lorentzian functions as shown in Figure 4.10(c). The fit parameters for the Lorentzian functions obtained from the fit is shown in Table 4.1. In the spectrum there is no noticeable NV^0 emission. This is expected as the green pump power was close to 100 mW and the population of NV^- is expected to be more than that of NV^0.

The stimulated emission cross-section is estimated from the spectra as mentioned in section 3.2.1 using the Füchtbauer-Ladenburg equation [77, 80, 86]. For this the $\int \lambda I(\lambda) d\lambda$ is replaced by $\sum \lambda I(\lambda) \delta\lambda$. The $\sigma_{se}(\lambda)$ obtained is shown in Figure 4.11. The γ was assumed as r_{31}.

In addition to increasing the losses, the diamond also modifies the resonance frequencies as we had discussed in section 3.1. The diamond modes for the sample studied in this thesis was experimentally captured in the recent version of the cavity apparatus with the shear piezo tuning of the cavity length. The cavity was pumped with a green laser and the emission spectrum of the NV centre was obtained (see section 4.3.3). Ramping the cavity length back and fourth for roughly 3.75 μm 20 times, during the acquisition of the spectrum, a scaled emission spectra modified by the diamond cavity mode is observed as shown in Figure 4.12. In order to interpret the experimentally observed spectra accurately as diamond cavity modes, an approach with an extended 3×3 transfer matrix simulation including a source term [118] might be a proper approach as this is a case of emission from inside the cavity rather than

Peak position	amplitude	FWHM
636.9 nm	0.1	3 nm
658.3 nm	0.3	21 nm
681.5 nm	0.6	31.7 nm
703.4 nm	0.6	31.7 nm
721.0 nm	0.3	30.4 nm
739.0 nm	0.3	31.7 nm
758.5 nm	0.2	33.1 nm
782.3 nm	0.1	30.4 nm

Table 4.1: Parameters obtained from the 8 Lorentzian fit functions of the spectrum. Since the amplitude is the normalized intensity, it is in arbitrary units.

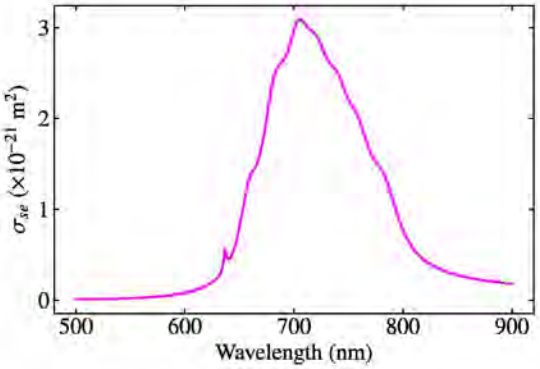

Figure 4.11: Stimulated emission cross-section of the NV centre sample as a function wavelength. The stimulated emission cross-section was determined using the 8 Lorentzian fit functions using the parameters shown in table 4.2. At ~ 721nm, $\sigma_{se} \sim 3.22 \times 10^{-21}$ m^{-2}.

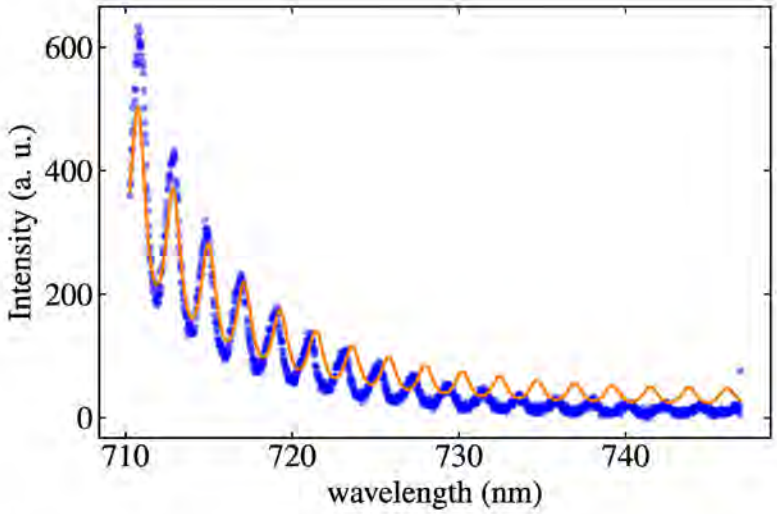

Figure 4.12: The NV emission spectra into the diamond mode. The blue curve is the spectra obtained by pumping a green laser and the orange curve is the theoretically simulated fit as described in the text. The simulated curve matches in the lower wavelength region, but not in the higher wavelength region.

transmission through the cavity. However, this method seems a bit computationally heavy and time consuming, since the ramping of the cavity has to be included. A simple approach might be to consider only the diamond and the output coupler. Since the cavity length was changing throughout the measurement, the cavity was always resonant to some wavelength. As a result naively this case can be considered as an emission into the diamond slab and then transmission through the output coupler. In fact the emission inside the diamond can be naively scaled with the transmission of the diamond crystal [118]. Then the effective modes observed (T_{eff}) can be approximated as the transmission of the diamond slab as a function of wavelength, which can be written as,

$$T_{eff}(\lambda) = \frac{T'^2 T_{DBR}(\lambda)}{1 + R'^2 - 2R' \cos\left(\frac{4\pi l_d}{\lambda}\right)}, \tag{4.1}$$

where T' and R' are the standard Fresnel's intensity transmission and reflection coefficients for the diamond to air interface, l_d is the optical thickness of the diamond and the λ is the wavelength, and $T_{DBR}(\lambda)$ is the wavelength dependent DBR coating of the flat mirror. A calculated $T_{eff}(\lambda)$ is also shown in Figure 4.12, which indicates that the periodic structure was due to the diamond mode. The parameter for the calculated $T_{eff}(\lambda)$ is obtained by fitting an arbitrarily scaled $T_{eff}(\lambda)$ to the experimental spectrum using least square fit method in *Python* (lmfit). For an initial value of 50 μm, the thickness of our diamond sample obtained from the fit is $\sim$ 50.05 μm, with negligible uncertainty ($\pm$ 6.76 $\times$ 10^{-4} μm). The matching between the fit and the experimentally observed spectra shows that the observed periodic structure is due to the diamond modes. It also shows that the slope in the spectra is mainly due to the out-coupling mirror transmission factor. The NV emission also has a similar slope around these wavelengths. In the experimentally observed diamond modes this slope of the NV emission might have contributed. The thickness of the mirror substrate on which the DBR coating, and air gap are also neglected for simplicity in the calculation as the DBR is more important. Thease could be the reason for the mismatch in y value for higher wavelength.

4.3 Laser amplification due to the stimulated emission of the NV centres

No lasing has been observed from NV centres in fibre cavities during the course of this project so far, though many rounds of experiments were performed to see lasing from NV centres in different generations of the cavities. However, a laser amplifier, which is interpreted as due to the stimulated emission by the NV centres in the fibre cavities have been observed. The laser amplification denotes the amplification on the transmission of a red laser through the sample loaded cavity pumped with a green laser. Though an amplification up to a factor around 3 was observed in our earlier generation of the cavity from which the finesse measurements were made, the challenge was to unambiguously interpret it. If it was an NV emission stimulated by the spontaneous emission of the NV centres, the quantum way might be to carry out an investigation on the second order intensity auto-correlations across the threshold, so that the coherence in the stimulated emission might be observed [119]. Since the amplification was observed through the cavity transmission of a laser light, such correlation measurements are hard. However, in the quest to achieve lasing from the NV centres an automated experiment with a stable laser pumping was built as an optimized version of the cavities. The laser amplification was observed in this experimental setup. From systematics of the study, the

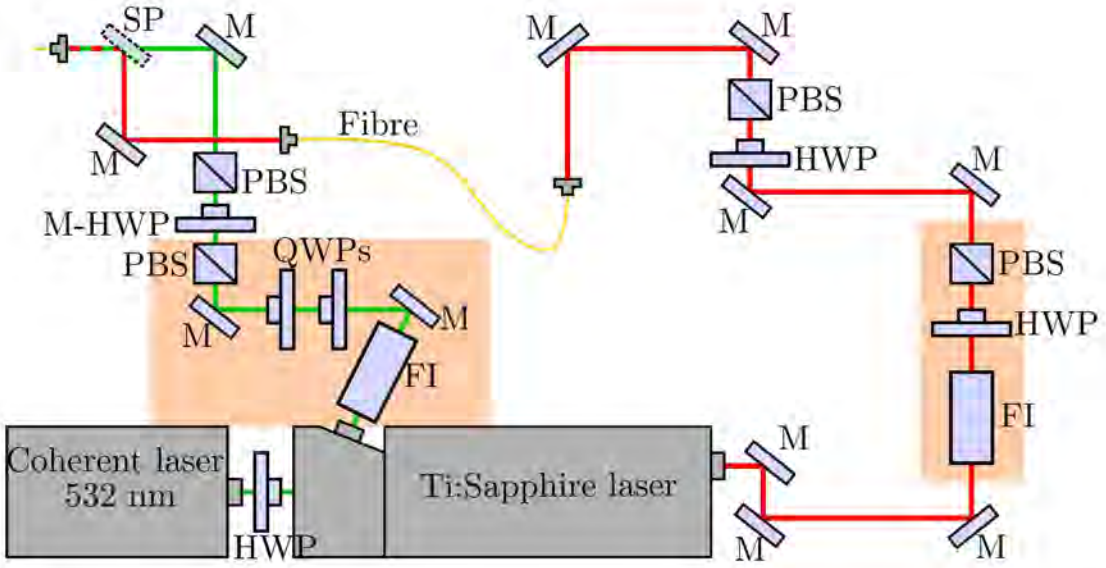

Figure 4.13: Beam combining setup including the setup to block the back reflected beams. The red and green colour correspond to the red and green lasers. The shaded region highlights the back reflection blocking setup. The dashed red and green lines represent the beam combining. Abbreviations;M : mirror, FI : Faraday isolator, HWP: half wave plate, M-HWP: half wave plate in a motorized mount, QWP: quarter wave plate, PBS : polarizing beam splitter, SP : short-pass filter.

ionization of the NV centre was identified as a limiting factor for achieving lasing from the NV centres. However, the observation of amplification of the cavity transmission, in the presence of ionization of the NV centres, enables to interpret that the amplification is due to the stimulated emission of the NV centres. These experiments and the results are presented in this section.

4.3.1 Stable lasers for the experiments

In the amplification presented in this thesis, a red laser around 721 nm and a green laser (~ 532 nm) were used. A wavelength tunable Ti:Sapphire (MSquared SOLSTIS) laser pumped with a green (Lighthouse Photonics) laser was used for the red wavelengths and a part of the green pump to the Ti:Sapphire laser was used as the green laser for the experiments. The laser powers were not actively stabilized and the experiments relied on the intrinsic power stability of the laser provided by the manufacturer. In order to stabilize the wavelength of the tunable red laser, an external wave-meter (HighFinesse WS-U) was used for locking red laser to a specific wavelength.

In our experiments the lasers were sent to the cavity through the cavity fibre for efficient coupling of the light into the cavity mode without any additional mode matching optics. For this purpose both the green and red lasers were combined together and coupled into an optical fibre that was connected to the cavity fibre. The main challenge in this experiment was the back-reflection from the cavity through the fibre.

Though the green laser has close to 60% transmission through the cavity mirrors, for higher green pump powers, the back-reflection became significant. The red laser, particularly the 721 nm laser, has almost 99.99% reflection from the cavity mirrors. As a result when the cavity was off-resonant the back-reflection was significant. As we see in the next section, our experimental technique of ramping the cavity always ensures off-resonant condition for

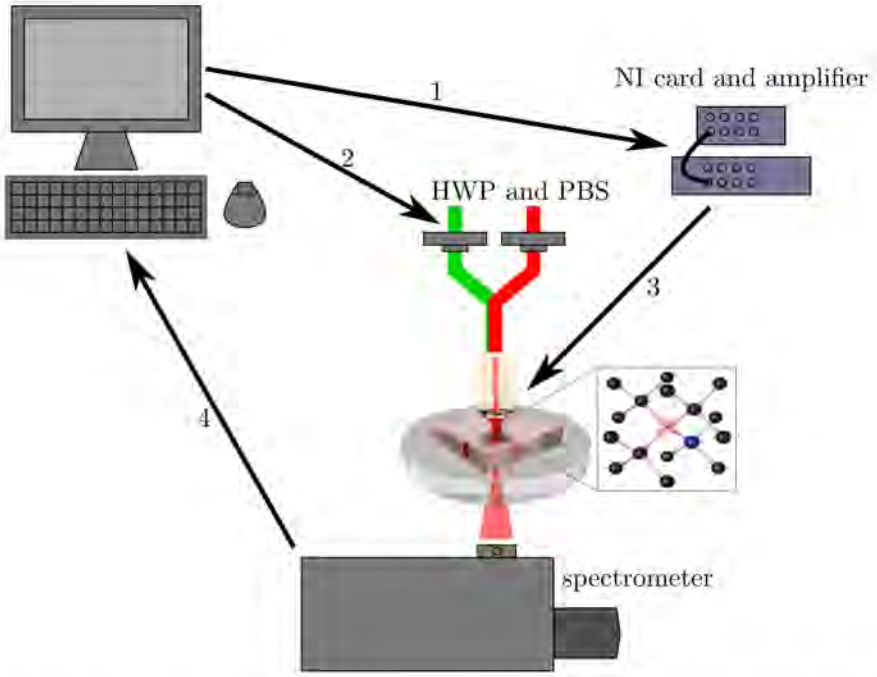

Figure 4.14: Schematic of the automated experiments. The arrows 1 and 2 represent communications from the computer to the NI card and amplifier, to the motorized HWPs that controls the laser powers respectively. The arrow 3 represent communications from the NI card and amplifier to the shear piezo that controls the cavity length. The arrow 4 represent acquisition of spectra through the QUDI.

our cavity. Even under resonant conditions, due to the deviation from an ideal resonant, i.e, 100% transmission through the cavity, the back-reflection was always present.

Any back-reflection from the cavity that goes back into the red laser causes mode instabilities which prevent wavelength locking. In additions to this, the back reflections that go back into the green and red laser may create power fluctuations. As a result the intrinsic power stability of the laser was not reliable anymore.

A schematic of our beam combining set-up including the back-reflection blocking is shown in Figure 4.13. A standard way to block the back reflection is to use a Faraday Isolator (FI) suitable for the laser wavelength, in front of the laser. However, in our setup, we had problems due to the back-reflections in the red wavelength and we experimentally found that by putting a combination of suitable polarizing beam splitter (PBS) and a half wave plate (HWP) was used in front of the FI, the back reflection problem were solved. One could interpret that the problem of back reflection, even with FI in front of the tunable Ti:Sapphire was due to the use of this laser for multiple experiments and the FI infront of the tunable Ti:Sapphire was not optimized for this particular experiment. We used similar combination of suitable FI, HWP and PBS in front of the green laser also, in order to avoid any possible back reflection problems for the green, particularly for high powers. Furthermore, in order to control the power as of the green and red laser and additional suitable PBS and a HWP were used. The motorized HWPs discussed in Figure 4.14 for controlling the green laser powers were controlled through the QUDI software control [120].

4.3.2 Automation of the experiments

The manual changing and checking of the experimental parameters like laser powers impedes the experiments to see the NV laser in the previous generations of cavities. Since the fibre-cavities are susceptible to external noises and also due to the lack of an active feedback loop in the setup, the measurements have to be taken fast. Moreover, in order to capture the essential effect through the measurements, the experiment has to be repeated a number of times as well. Considering these factors, instead of relying on manual control, the experiments were automated through *Python* and QUDI [120] software control. A schematic of the automation of the experiment is shown in Figure 4.14.

The experimental apparatus includes a voltage source to control the cavity length. In the present experiments the NI card together with an attocube (ANC 250) amplifier was interfaced with *Python* through the *PyDAQmx* library particularly the *Task* class to generate the voltages in the desired form. Though the experiments can be performed either with static voltage or with voltage ramps, the amplification measurements done in this section was with voltage ramps. The maximum voltage range possible with the NI card is ±10 V. However, the shear piezo (Noliac) works for its full specification of 6 μm with ± 320 V. The voltage amplifier was used to amplify the voltage generated by the NI card by a factor of 20, which then goes to the shear piezo. Hence for the cavity illuminated by light at 721 nm, the number of FSR for a voltage ramp from -10 V to +10 V is roughly around 10. The frequency of the voltage ramps that was used in the experiments was 1Hz so that the slow ramp makes it easy for the shear piezo to respond. Setting a slow ramp also means that the amplification experiments were CW measurements as it allows enough time to the cavity to reach steady state.

The cavity output spectra were acquired through QUDI. This enablesd real time data analysis and plotting of the parameter of interest. This enhances the efficiency in measurements, especially when optimizing the measurements. The typical spectrometer acquisition time was 10 seconds. This acquisition time was set to synchronize the voltage ramps, so that the spectrometer acquisition had a better signal to noise ratio.

Amplification measurements were done by recording three kinds of transmission spectra of the sample loaded cavity, illuminated by green laser alone, red laser alone, and also green and red lasers combined. The absolute order of the pumping is irrelevant. Comparing the spectra obtained from these different pumping scenarios allowed the effects of each laser to be identified.

The automated experiments were done in two modes depending on the synchronisation of the voltage ramp that control the cavity length and the spectrometer acquisition. The first one was to do voltage ramps up and down ten times and thereby tuned the cavity length for almost 200 FSRs for one full spectrometer acquisition. This made it possible to average out the drifts in the cavity. However, since throughout the fast ramps the cavity could move through the fundamental Gaussian mode as well as higher order Hermite-Gaussian modes, this measurement approach gave an average effect. In the present study the stimulated emission has to be strong in order to detect it through this kind of measurement. The voltage ramps were generated using a *Python* script. The second measurement strategy was to sweep through a cavity mode at once and then acquired spectra for this one sweeping through the cavity. The cavity mode was roughly located using trial and error by applying a static voltage to the shear piezo. Once the resonance was located, a voltage range was set to sweep through the cavity in such a way that the cavity mode is at the centre. This measurement was repeated by putting them into a loop command in *Python* by resetting the sweep range after each sweep

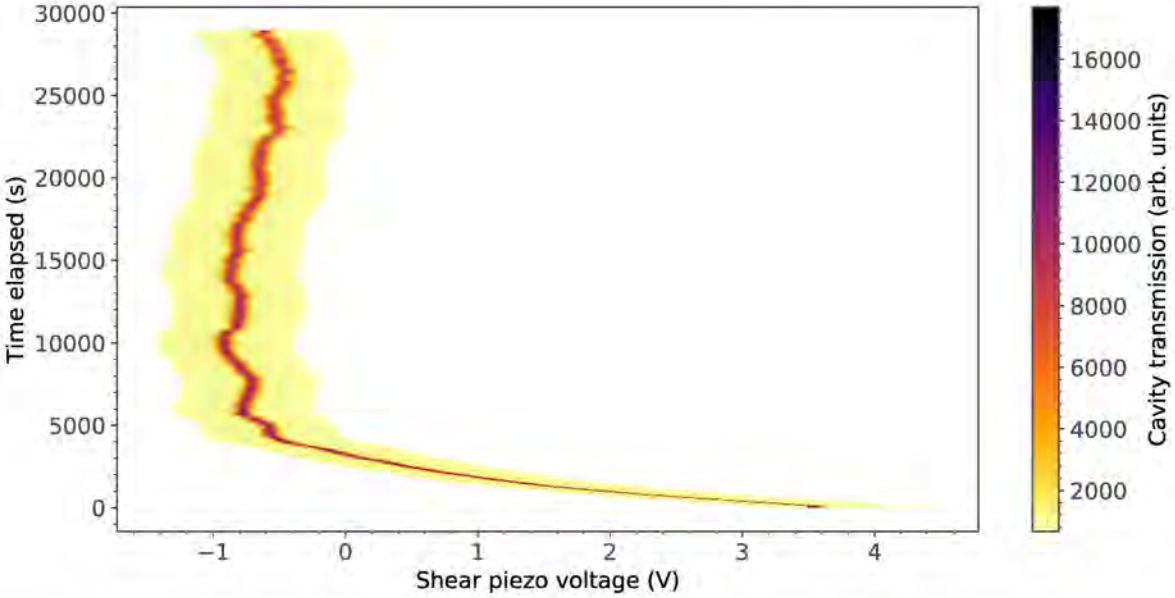

Figure 4.15: Cavity transmission with sweeping of the cavity recorded. The y axis is the time of the measurement, where the zero corresponds to the starting time of the measurement. The x axis is the union of sweeping ranges during the whole measurements.

and acquisition such that the cavity mode is at the centre of the sweep range. An example of the cavity transmission, which is the intensity obtained from each spectrum acquired in cavity sweeps, performed is shown in Figure 4.15.

The important portion of the *Python* code that is used to generate voltages from the NI card in the desired form is shown below. The static voltage was generated using

```
value = 0
v_min = -10.0
v_max = 10.0
task = Task()
task.CreateAOVoltageChan("/Dev1/ao0","",v_min, v_max,PyDAQmx.DAQmx_Val_Volts,None)
if value<=v_max:
    task.StartTask()
    task.WriteAnalogScalarF64(1,10.0,value,None)
else:
    task.StopTask()
```

The voltage ramps were generated using,

```
v_min = -10.0
v_max = 10.0
steps = 40000

freq = 1

step_size_one_way = 2 * (v_max - v_min) / steps

data_up = np.arange(v_min, v_max, step_size_one_way, dtype=np.float64)
data_down = np.arange(v_max, v_min, -1 * step_size_one_way, dtype=np.float64)\

data = np.append(data_up, data_down)

################################################################################

task = Task()
task.CreateAOVoltageChan("/Dev1/ao0","",-10.0,10.0,PyDAQmx.DAQmx_Val_Volts,None)
task.CfgSampClkTiming("",freq * steps,PyDAQmx.DAQmx_Val_Rising, PyDAQmx.DAQmx_Val_ContSamps
    ,1000)

task.WriteAnalogF64(len(data),0,10.0,PyDAQmx.DAQmx_Val_GroupByChannel,data,None,None)
```

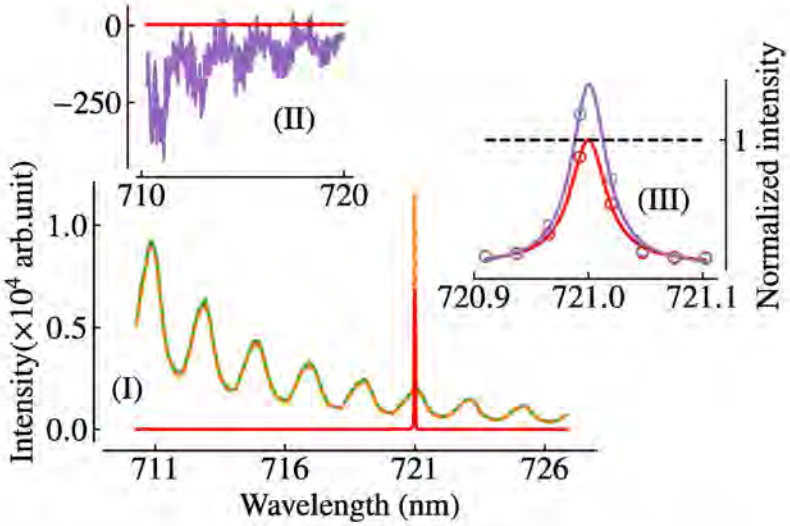

Figure 4.16: Representative spectra obtained in the cavity transmission showing amplification. The x-axis for all the figures is wavelength in nm. (I) The green and dashed orange curves are the spectra acquired for green alone and green and red combined pumping respectively. (II) The red one is the spectrum for the red alone pumping. The purple colour is the difference of spectrum of green alone pumping from the spectrum of green and red combined pumping and the negative sign means that the spectrum of the green alone pumping is higher than the green and red combined pumping. (III) The purple circles correspond to the data points from the difference of the spectrum of green alone pumping from the spectrum of green and red combined pumping. The red circles correspond to the data points in the spectrum of red alone pumping. The purple and red curves are the Lorentzian fit for the data points. The y axis is normalized with the amplitude of the Lorentzian fit to the red alone spectrum. The black dotted line is a reference line showing factor 1. The amplitude of the purple curve above 1 indicate amplification.

```
21
22 task.StartTask()
```

4.3.3 Observation of laser amplification with the fast ramping method

Two different experiments were performed with the red laser around 721 nm and the green laser around 532 nm, using the first method of sweeping over 200 FSRs mentioned in the previous section. The first one had a small power of around 67 μW for the red laser and the green pump power was varied roughly between 1 mW to 150 mW into the input port of the cavity fibre. Secondly, we pump different high powers of red laser roughly between 1 mW and 50 mW and the green pump power was varied roughly in the same range as the first one.

Representative spectra showing the amplification due to the stimulated emission is shown in Figure 4.16 for green pump power around 31.73 mW and for the red laser power around 67 μW. As mentioned in the previous subsection, spectra for green alone pumping, red alone pumping, and green and red combined pumping were compared. At the stimulating red wavelength, the amplification was observed in the presence of a green laser along with the red laser (Figure 4.16(III). On the other hand, a reduction in spontaneous emission was observed (Figure 4.16(II) at the particular green pump power in the spontaneous emission part of the spectrum.

In order to explore the effects of pumping schemes on the NV centres in a systematic

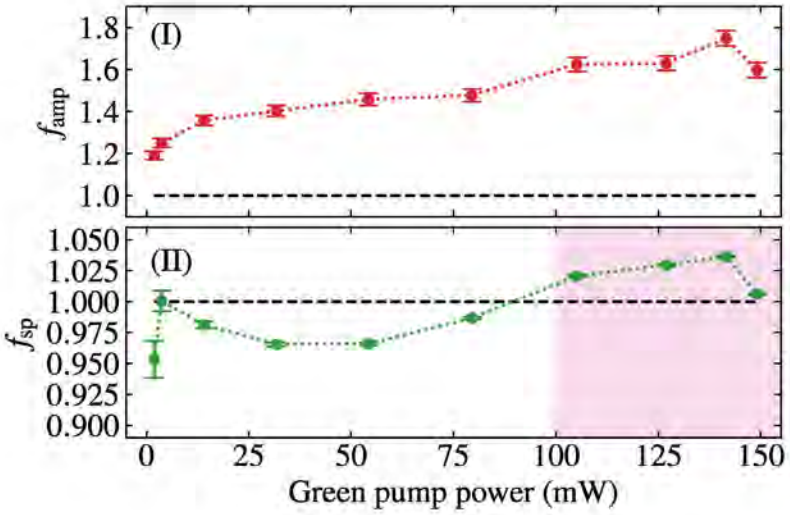

Figure 4.17: Experimentally observed amplification factors as a function of green pump power, for the red laser power around 67 μW. (I) The amplification factor for the cavity transmission of the red wavelength. (II) The reduction in the spontaneous emission of the region shown in 4.16(II). The black dotted line is the reference line at factor 1. The shaded region highlights the region with increase in the spontaneous emission. The error bars shown in both (I) and (II) are one standard deviation obtained by propagating the shot-noise error in the spectrometer count.

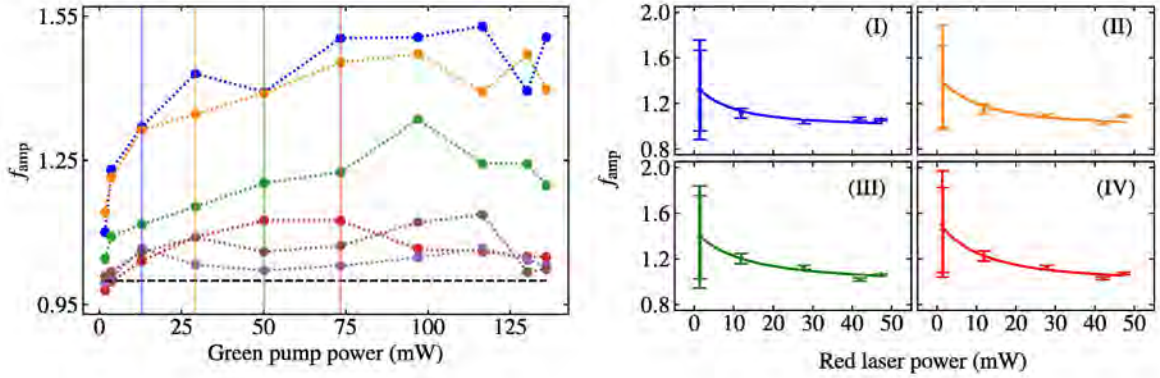

Figure 4.18: Experimentally observed change in amplification factors as a function of red laser power. (a) The blue, orange, green, red, purple and brown points corresponds to red power of ~ 1.39 mW, ~ 1.54 mW, ~ 11.84 mW, ~ 27.77 mW, ~ 41.92 mW, and ~ 47.26 mW respectively. (b) The amplification factors along the solid lines in (a) as a function of red laser power. The blue, orange, green, and red circles in (I), (II), (III), and (IV) are the amplification factors corresponding to the green pump powers ~ 12.89 mW, ~ 29.24 mW, ~ 50.09 mW, and ~ 73.38 mW respectively. For clarity the error bars of one standard deviation obtained by propagating the shot-noise error in the spectrometer count, are shown in (b) as representative ones. The solid curves with respective colors are the fit functions. The fit function in (I), (II), (III), and (IV) are $1 + 121(x + 18)^{-2}$, $1 + 181(x + 20)^{-2}$, $1 + 276(x + 25)^{-2}$, and $1 + 260(x + 22)^{-2}$ respectively, where x in this case is the red laser power.

manner, two dimensionless factors are defined. The first one f_{amp} corresponds to the amplification at the stimulating red laser wavelength in the wavelengths of data points shown in Figure 4.16(III). The second one f_{sp} corresponds to the spontaneous emission from the NV centres in the wavelength range shown in Figure 4.16(II). The f_{amp} was determined by subtracting the green alone spectrum from the spectrum of green and red combined pumping and taking the ratio of the numerical sum of these data points to that of the red alone spectrum. The f_{sp} was determined by subtracting the red alone spectrum from the spectrum of green and red combined pumping and taking the ratio of numerical sum of data points in the region shown in 4.16(II), to that of the green alone spectrum.

The f_{amp} and f_{sp} as a function of the green pump power are shown in Figure (4.17). For f_{amp} and f_{sp}, 1 means no effect of the different pumping schemes on the NV centre. f_{amp} increases as a function of green pump power and shows a saturating trend for higher green pump power, where as the f_{sp} shows a characteristic oscillatory behaviour. Interestingly, f_{sp} in the shaded region, follow the behavior of the corresponding f_{amp}.

In the light of the qualitative model that we see in the following section we, interpret that the increase in f_{amp} is due to stimulated emission of the NV centres and the characteristic feature of f_{sp} is due to the photo-induced charge state switching of the NV centre [81, 99, 100, 107].

In the second set of measurement, we observe the reduction in the f_{amp} when the red pump power increases by repeating the measurement as mentioned in the previous paragraphs. The observed effect of red alone pumping power on the f_{amp} is shown in Figure 4.18. This effect is also attributed due to the charge-state switching or ionization of NV centre into its neutral charge state [81, 99, 100, 107]. The amplification factor measured as a function of red laser power fits well with a quadratic function as shown in Figure 4.18(b). This is consistent with the argument that the two photon picture of the ionization [99] that we discussed in the Chapter 3. In the Figure 4.18(a), we can also see amplification factor below 1. This has been observed in other measurements also. This is consistent with the picture that the red laser is pushing the NV^- centres into some dark states.

Qualitative model for interpreting the laser amplification

Since the cavity length was tuned back and forth over many free spectral ranges during the measurements, an accurate modelling of the experiment is hard. Hence a qualitative modelling of the experiments is done. One can imagine two layers of physics in this experiment. The first one is the physics of the cavity and the second one is that of NV^- centres. We first consider a simplified version of our red laser pumped cavity in the experiment and then model the interaction of NV^- centres with the fundamental cavity field. In order to model the NV centres, a single NV centre is considered and modelled using a rate equation model. Then to get the collective effect on the amplification from the NV centres, this model is scaled with the total number of NV centres inside the cavity volume.

Due to the cavity length tuning, the red wavelength can form both fundamental Gaussian as well as higher order Hermite-Gaussian modes in the cavity. Also, the emission of the NV centre into the fundamental modes as well as into the higher order modes of the cavity is possible. Since the coupling of the red wavelength into the cavity mode and the spatial distribution of the cavity mode vary depending on the order of the mode, the amplification factor due to stimulated emission is expected to have different values in different modes of the cavity. However, the most efficient interaction of NV centres with the cavity is possible in the fundamental mode. Hence for simplicity and to extract the essential physics by relaxing the accuracy, we consider only the fundamental mode of the cavity. Though the fundamental

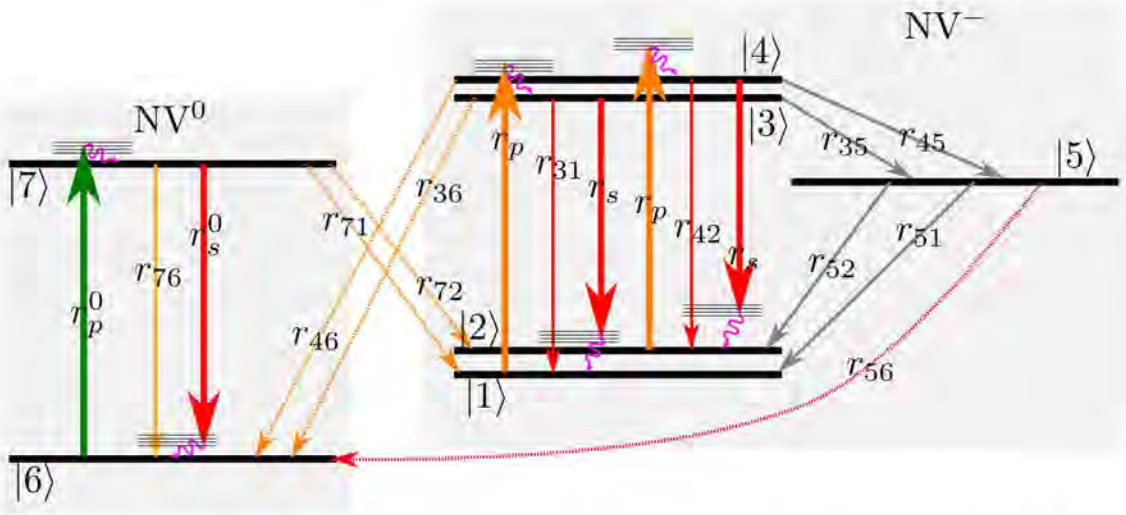

Figure 4.19: NV centre model for interpreting amplification. Levels $|1\rangle$ to $|5\rangle$ belong to NV^- and $|6\rangle$ and $|7\rangle$ belong to NV^0. In the NV^-, $|1\rangle$ and $|2\rangle$ respectively represent the $m_s = 0$ and ± 1 of the ground state, and $|3\rangle$ and $|4\rangle$ respectively represent the $m_s = 0$ and ± 1 of the excited state. $|5\rangle$ represent the singlet level of the NV^- centre. In the case of NV^0 it has only ground state ($|6\rangle$) and excited state ($|7\rangle$). Orange arrows represent transitions due to both green and red wavelengths. Solid orange lines represent the pumping rates, whereas the dotted ones represent the ionization and recombination transitions. The thin and thick solid red arrows represent spontaneous and stimulated transitions. The dotted red arrow represents ionization transition from the singlet level. Grey arrows represent inter-system crossing (ISC) transitions and magenta curly arrows represent the phonon decay. The green arrow represents the pumping rate of NV^0 by the green laser, and the yellow arrow represent its spontaneous decay. Transition rates are shown on each transitions.

mode of the cavity is Gaussian, we assume a flat-top approximation and a cylindrical volume of the cavity with the radius of the Gaussian spot size on the macroscopic mirror as the base radius. We assume this spot radius to be $\sim 5\ \mu$m. However, in the experiments, the absolute value of this spot radius may be different mainly due to the change in the refractive index as the light propagates through the cavity. For a qualitative model, it was assumed that the underlying physics is not going to change as the absolute value for the spot size is going to be close to this value. Assuming a Gaussian beam, at the stability limit, the spot radius of the cavity mode on the macroscopic mirror is expected to be less than 5μm. We assume that the cavity is fully filled with the diamond sample. Furthermore, for simplicity we assume that our cavity is resonant with the red wavelength and also that the red wavelength is fully transmitted through the cavity. Though this is not fully true in the experiment, it does not make much difference qualitatively as the amplification is expressed as a ratio. In our model the cavity volume sets the number of NV centres contributing to the amplification as in the experiment. It also sets the stimulating power or intensity of the red wavelength inside the cavity by scaling the power that we provide externally in proportion to the effective finesse of the cavity.

Considering charge state switching and both NV^- and NV^0, the NV centre was modelled as shown in Figure 4.19. The rate equations for this level scheme is written as,

$$\frac{dp_{|1\rangle}}{dt} = -r_p p_{|1\rangle} + r_{31} p_{|3\rangle} + r_s p_{|3\rangle} + r_{51} p_{|5\rangle} + r_{71} p_{|7\rangle}, \tag{4.2}$$

$$\frac{dp_{|2\rangle}}{dt} = -r_p p_{|2\rangle} + r_{42} p_{|4\rangle} + r_s p_{|4\rangle} + r_{52} p_{|5\rangle} + r_{72} p_{|7\rangle}, \tag{4.3}$$

$$\frac{dp_{|3\rangle}}{dt} = r_p p_{|1\rangle} - (r_{31} + r_s + r_{35} + r_{36}) p_{|3\rangle}, \tag{4.4}$$

$$\frac{dp_{|4\rangle}}{dt} = r_p p_{|2\rangle} - (r_{42} + r_s + r_{45} + r_{46}) p_{|4\rangle}, \tag{4.5}$$

$$\frac{dp_{|5\rangle}}{dt} = r_{35} p_{|3\rangle} + r_{45} p_{|4\rangle} - (r_{52} + r_{51} + r_{56}) p_{|5\rangle}, \tag{4.6}$$

$$\frac{dp_{|6\rangle}}{dt} = -r_p^0 p_{|6\rangle} + (r_{76} + r_s^0) p_{|7\rangle} + r_{46} p_{|4\rangle} + r_{36} p_{|3\rangle} + r_{56} p_{|5\rangle}, \tag{4.7}$$

$$\frac{dp_{|7\rangle}}{dt} = r_p^0 p_{|6\rangle} - (r_{76} + r_s^0 + r_{72} + -r_{71}) p_{|7\rangle}. \tag{4.8}$$

Hhere $p_{|j\rangle}$ is the population fraction of a single NV centre on the level $|j\rangle$. Thus $\sum_{j=1}^{7} p_{|j\rangle} = 1$. Since the decay from the phonon levels of the ground state is expected to be very high, any stimulated absorption is neglected from these phonon levels back to the excited states. The rates r_p, r_s, r_{36}, r_{46}, r_{72}, r_{71} and r_{56} are light induced transitions. If I represent the intensity of light, σ is the cross sections, and $h\nu$ is the photon energy, then these photo-induced transition rates are generally $\frac{I\sigma}{h\nu}$. Again similar to all other rate equations that we have seen in this thesis, the intra-cavity fields as assumed to be independent of time as we are focusing on the steady state. This system for steady state is solved to obtain the population fractions. Then using parameters shown in table 4.2, we estimate population fractions as a function of green and red powers. The ionization, recombination and stimulated emission rates are obtained using the cross-sections of the transitions.

In the experiments no saturation effects were observed on the spontaneous emission from the NV centres. Hence we consider a lower value of the absorption cross-section for the green available in literature from references [46, 121]. For simplicity, we consider no spin dependence on ionization transitions directly from the excited states of NV^-, as reported in [100], since it makes no difference in essence due to the absence of MW or magnetic field in our experiments. In this model the indirect spin dependence on the ionization comes through spin-dependent transitions to the singlet states [105]. The ionization and recombination cross-section values at this particular red laser wavelength was not available from literature. In reference [81], a red laser of 766 nm was used for the stimulated emission and ionization study of the NV centre. The amplification is modelled by adapting the parameters from the this study to fill the missing rates. The population fractions are obtained as a function of green pump power for $\sim 67\mu$W of red power as shown in Figure 4.20.

Figure 4.20(a) shows that the presence of the red laser along with the green laser reduces the NV^- population fraction and increases the NV^0 population fraction due to ionization. Figure 4.20(b) shows that ionization is dominant for lower green pump powers. At higher pump powers due to efficient excitation of the NV^0 compared with that of NV^-, $p_{|7\rangle}$ increases.

The population fractions that determines the emission from NV^- is $p_{|\mathrm{exc}\rangle} = p_{|3\rangle} + p_{|4\rangle}$, whereas for the NV^0 it is $p_{|7\rangle}$. f_{amp} due to stimulated emission from all the NV centres can be written as

$$f_{\mathrm{amp}} = \frac{P_{\mathrm{red}} + \frac{1}{2} P_{\mathrm{stm}}}{P_{\mathrm{red}}}, \tag{4.9}$$

Parameter	Value	Reference
$r_{31} = r_{42}$	63.93 MHz	[56]
r_{35}	7.93 MHz	[56]
r_{45}	53.25 MHz	[56]
r_{51}	0.98 MHz	[56]
r_{52}	0.72 MHz	[56]
r_{76}	$0.74 \times r_{31}$	[81]
σ_g	$3.1 \times 10^{-21}\mathrm{m}^2$	[121]
σ_r	$3 \times 10^{-24}\mathrm{m}^2$	[45]
$\sigma^g_{36} = \sigma^g_{46}$	$0.037 \times \sigma_g$	[81]
$\sigma^g_{71} = \sigma^g_{72}$	$0.08 \times \frac{1}{2}\sigma_g$	[81]
$\sigma^r_{36} = \sigma^r_{46}$	$0.071 \times \sigma_{se}$	[81]
$\sigma^r_{71} = \sigma^r_{72}$	$0.22 \times \frac{1}{2}\sigma_{se}$	[81]
σ^r_{56}	$0.0215 \times \sigma_{se}$	[81]

Table 4.2: Parameters used for the theoretical estimations. The transition rates are the average of the values from ref [56]. In general σ is the cross-section of the light induced transition. The superscript represent the color of the corresponding laser. Though the wavelength used for the red is different in reference [81], we approximate these values for the present wavelength of interest. σ_g and σ_r are absorption cross-sections of NV^- for green and red wavelengths. The absorption cross-section of the NV^0 for green wavelength is 1.3 times higher than that of NV^- [81]. Though the wavelength used in [45] is different, absorption cross-section for the stimulating wavelength is considered approximately equal to this value.

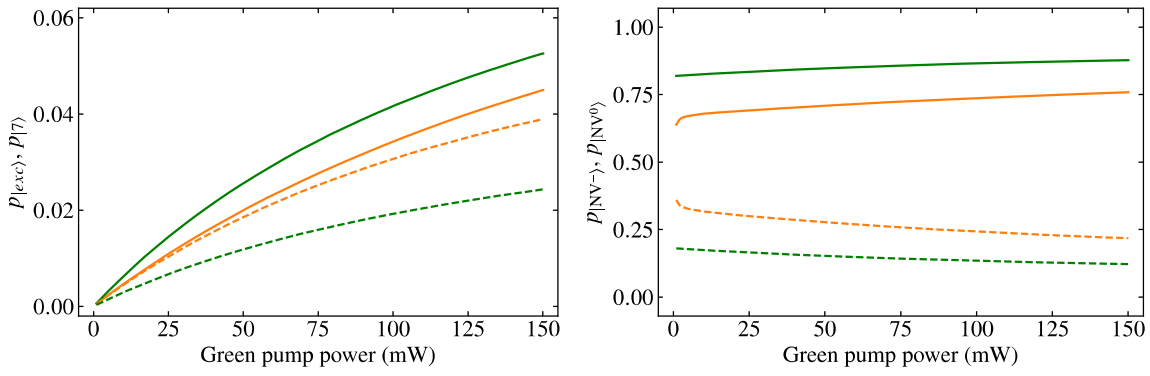

(a) (b)

Figure 4.20: Green and orange colours represent green laser alone pumping and green and red lasers combined pumping. The solid and dashed lines represent the NV^- and NV^0 respectively. For green and red lasers combined pumping, stimulated emission of both NV^- and NV^0 are considered. However, for green laser alone pumping, we neglect the possibility of stimulated emission from any of the charge states considering the fact that the spontaneous emission from these charge states into the cavity is not stimulating the emission as we do not see any trace of it in our experiment. (a) Calculated effect of green and red lasers on the excited state population fractions of NV^- ($p_{|exc\rangle}$) and NV^0($p_{|7\rangle}$) as a function green pump power. (b) Calculated effect of green and red lasers on the total population fractions of NV^- and NV^0.

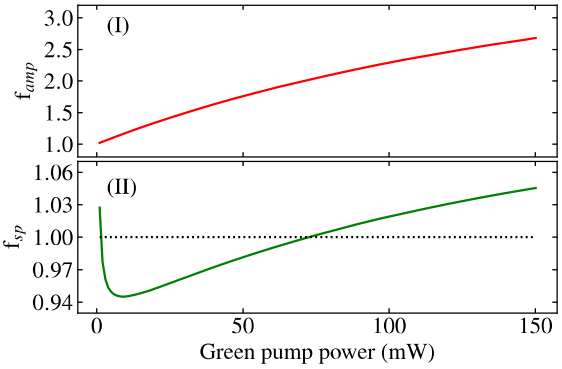

Figure 4.21: f_{amp} and f_{sp} from the qualitative model as a function of green pump power. (I) The f_{amp} due to stimulated emission. (II) The f_{sp} spontaneous emission with the stimulated emission of both charge state of NV centre is shown in green solid line. The black dotted line is the reference line at factor 1.

where P_{red} is the cavity transmitted red laser power and P_{stm} is the total power emitted by NV centres due to the stimulated emission. The factor $\frac{1}{2}$ comes from the fact that we consider that the stimulated emission comes out through both sides of the cavity and in the transmitting side we capture only half of it. Then we can rewrite equation (4.9) considering stimulated emission from both charge states [80] as,

$$f_{\text{amp}} = 1 + \frac{1}{2}\Big((p_{|\text{exc}\rangle} + \eta p_{|7\rangle})F\sigma_{\text{se}}\rho_{\text{NV}}l\Big). \tag{4.10}$$

Here σ_{se} is the stimulated emission cross section of the NV centre in the negative charge state and the η is the ratio of stimulated emission cross-section of NV^0 to NV^-, ρ_{NV} is the density of the NV centres in the diamond sample and l is the cavity length, which in our model is the thickness of the sample. F is the ratio of the intra-cavity red laser power and the power outside the cavity. Since the intra-cavity power is scaled by finesse (finesse/π), F is finesse/π.

The dependence of the f_{amp} on the laser power comes through $p_{|exc\rangle}$ and $p_{|7\rangle}$. In reference [80], around 721nm the ratio between the stimulated emission cross-section of NV^- to NV^0 is slightly higher than 3. From this we can make a reasonable assumption that $\eta \sim \frac{1}{3}$.

The spontaneous emission from this model into an optical frequency ν can be written as,

$$P_{\text{sp}} = (r_{31}p_{|\text{exc}\rangle} + r_{76}p_{|7\rangle})h\nu\rho_{\text{NV}}V_{\text{cav}}, \tag{4.11}$$

where V_{cav} is the volume of the cavity, which is the effective cylinder volume that we assumed. Then the amplification factor f_{sp} for the spontaneous emission irrespective of the frequency can be written using equation (4.11) as,

$$f_{\text{sp}} = \frac{p_{|\text{exc}\rangle} + \beta p_{|7\rangle}}{p'_{|\text{exc}\rangle} + \beta p'_{|7\rangle}}, \tag{4.12}$$

where prime $'$ corresponds to green alone pumping and β is the ratio of the spontaneous emission rate of NV^0 to NV^-. Any spontaneous emission from both the charge states of NV was neglected for red alone pumping, since at steady state the NV centres are expected to end up in the NV^0 ground state as red cannot excite the NV^0 in our model.

The f_{amp} and f_{sp} given in (4.10) and (4.12) respectively are plotted as a function of green pump power in Figure 4.21. The parameters of the NV centres for plotting these factors are

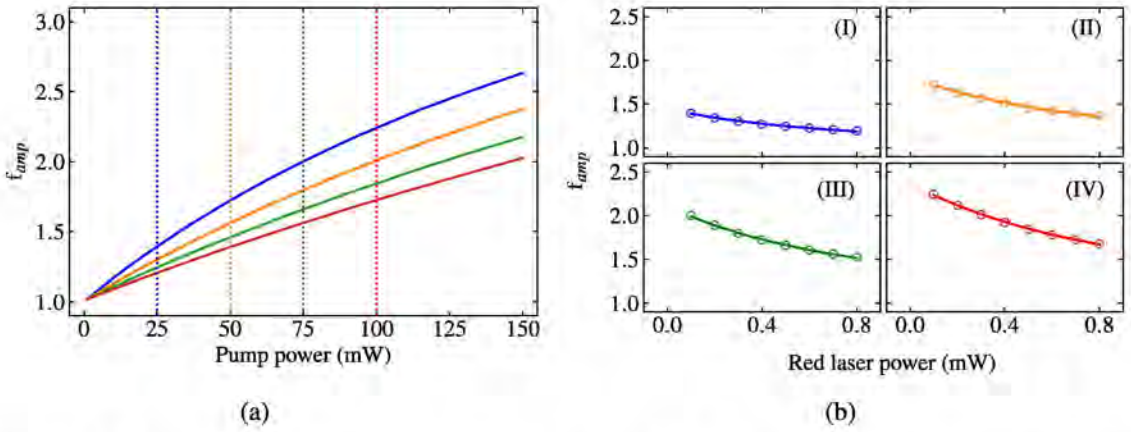

Figure 4.22: Change in amplification factors calculated from the theoretical model as a function of red laser power. (a) The blue, orange, green, red corresponds to red power of 0.1 mW, 0.3 mW, 0.5 mW, and 0.7 mW respectively. (b) The amplification factors in the dotted lines drawn in (a) as a function of red laser power. The blue, orange, green, and red circles in (I), (II), (III), and (IV) are the amplification factors corresponding to the green pump powers 25 mW, 50 mW, 75 mW and 100 mW shown by the dotted lines drawn in (a) with respective colours. The solid curves with respective colors are the fit functions. The fit functions in (I), (II), (III), and (IV) are $1 + 0.96(x + 1.47)^{-2}$, $1 + 1.98(x + 1.56)^{-2}$, $1 + 3.21(x + 1.7)^{-2}$, and $1 + 4.7(x + 1.85)^{-2}$ respectively.

discussed in appendixes. F, was set to 1200 to match the experimentally observed values of f_{amp} and f_{sp} roughly. This value is reasonable as it is below the designed value from the mirror coatings. Also similar value has been measured with our empty cavity and measuring the actual finesse particularly with the diamond sample loaded is difficult.

Modelled amplification factors in shown in figure 4.21 qualitatively match the amplification factors obtained in our experiments. Since the ionization is strong in the presence of the red laser, we have more NV^0 for red and green combined pumping than that of green alone pumping. As a result we interpret that the amplification we experimentally observe at the stimulating wavelength is due to the stimulated emission from both charge states of the NV centres. We interpret that in this system, due to ionization, the spontaneous emission decreases for lower powers of green alone pump. However, as the green power increases, due to the efficient pumping and slightly higher lifetime of the excited state in NV^0 than its negative counterpart, the spontaneous as well as stimulated emission from NV^0 contributes significantly to the total emission from the NV centres. Hence f_{sp} increases for higher green powers and goes even above 1. If there is no ionization, the maximum f_{sp} that one could expect is 1, as the stimulated emission during green and red lasers combined pumping reduces $p_{|\text{ex}\rangle}$ relative to green alone pumping. Furthermore, in the literature some studies report that NV^0 has lower excitation efficiency than NV^-. However, in the present model the observed f_{sp} could only be explained with higher excitation efficiency for NV^0 than NV^- as considered by studies [81, 107].

Since the spontaneous emission is also increasing for higher pump powers the spontaneous emission should also contribute to the amplification factor at high green power. The observation of a similar trend in f_{sp} and f_{amp} for higher green pump power might be the signature of spontaneous emission contributions from NV^0 to f_{amp}.

Furthermore, the dependence of f_{amp} on the red wavelength power is shown in Figure 4.22. The theoretically calculated f_{amp} as a function of red power fits well with the quadratic fit function for the experimental data. This strengthens our argument that the experimental

observation of reduction in amplification when red wavelength power increases is due to the ionization of the NV centre in the presence of a strong intra-cavity field.

Possible cavity effects on amplification

In the model that we presented, we have neglected the effect of the imperfections in the cavity transmission. In reality when the cavity transmission lower than 1, there is some reflected component along with the cavity transmission. When there is stimulated emission, where the emitted photons are in phase with the stimulating photons, the stimulated emission emerges from both sides of the cavity. Since the emitted photons are in phase with the stimulating photons, the total electric field of the stimulated emission destructively interferes with the cavity reflected electric field. As a result the transmission of the cavity is modified. In the amplification experiments, since the cavity was not fully transmitting, the stimulated emission could have modified the cavity transmission. However, this is not expected to alter the physics that we extracted from the model. In fact, when the cavity transmission is low the stimulated emission is expected to be low as the intensity of the stimulating wavelength is low.

In addition to this, three other effects can also contribute to the cavity transmission; absorption by NV centres, the change in the absorption due to the charge state switching and also thermal heating of the cavity fibre mirrors [47, 122]. The first one is really hard to account. The last one is expected to play an important role when the pump power of the red is high. When the red pump power is high, the intra-cavity power is going to be high as it is enhance by a factor of effective finesse. As a result on top of ionization, the high red power also impacts the cavity. Due to this reason for extracting the underlying physics we have considered lower red powers to approximately avoid the complexities of the cavity transmission.

4.3.4 Observation of laser amplification with the slow sweep method method

We tried to measure the amplification through the slow sweep method mentioned in the 4.3.2, in order to proceed to measure the laser amplification in the static cavity mode. The measurement was carried out by finding a cavity mode and sweeping through it for green laser alone pumping and green and red lasers combined pumping. One data set shows amplification, as shown in the Figure 4.23. This measurement was done with arbitrary green and red laser powers as a first step, the amplification is visible in the Figure 4.23. It is also clear that adding a green laser changes the cavity resonance as the voltage which is a proxy for the cavity length corresponding to the cavity resonance changes. This can be attributed to the thermal expansion of the fibre tip [47, 122]. However, unfortunately due to the time constraints and the breakdown of the fibre cavity setup, further systematic experiments could not be carried out.

4.4 Implications for LTM with the NV^- laser

Within the accuracy of the model and interpretations presented in this thesis, the observed amplifications on the transmission of fibre cavity modes, by external seeding is due to the the stimulated emission of NV centres that forms the basis of the LTM. The main issue

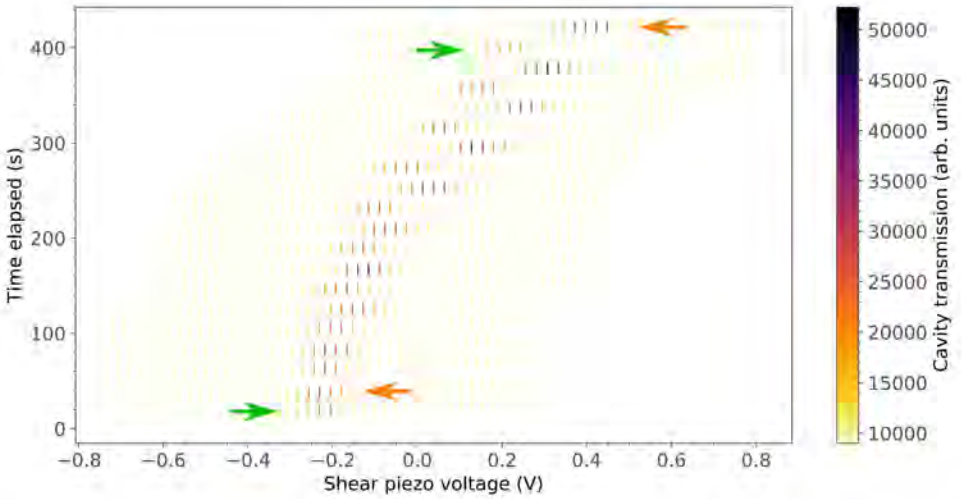

Figure 4.23: Observation of amplification with slow cavity sweep. The orange arrows denote the cavity sweep with green and red combined pumping and the green arrows denote the cavity sweep with green alone pumping. Only the first and last ones are denoted with arrows and the middle ones follow the same alternative sweeping. The red laser power was constant and the green power was increasing arbitrary as the time elapsed increases. For higher green laser powers adding a red laser changes the cavity resonance.

to achieve the self-seeded NV laser, seems to be the lousy nature of the diamond loaded cavity which results in inefficient trapping of the spontaneous emission for stimulating the NV centres. On the other hand, we can also see from Figure 4.20, that the excited state population is small compared with the total population fraction, for both charge states. In the case of NV^- centre, the simulation suggests that the ground state as well as singlet states have significant population fractions that is responsible for low population fraction of its excited state. The reduction in the excited population fractions, reduces the gain for the laser. Within the accuracy of the model presented here, it seems like the NV^0 stimulated emission also contributes to the observed amplification. One could extrapolate the results and could say that with a high Q-cavity, we might achieve a self-seeded laser. However, if such a laser has contributions from both stimulated emission of NV^0 and NV^-, one could naively question whether such a laser is really sensitive to magnetic fields anymore. To address this, more theoretical as well as experimental investigations are required. Though the charge state switching brings NV^- centres to magnetically insensitive NV^0, that switching process itself can be spin dependent [100]. The red induced transition discussed above from the singlet state is intrinsically spin dependent. Having said that more experiments and theoretical works are required to get clarity on this. An essential first step is to study the magnetic tunability of the laser amplification observed, which is unfortunately beyond the scope of the current thesis.

5

Room-temperature quantum sensor with diamond Raman lasers combined with MW driven NV^- centres

So far in this thesis, we have discussed magnetometry with an NV^- laser and efforts towards the experimental realization of such a laser. On the other hand, diamond crystal itself is an excellent gain medium for another type of laser known as a Raman laser [123–125]. Though such a laser exists in diamond itself, to the best of the authors knowledge, no study combining such lasers with NV^- centres is available in literature. In this chapter we theoretically investigate the response of such a diamond Raman laser modified by the intra-cavity absorption by the NV^- centres, driven by an MW frequency similar to the IR absorption LTM studied in reference [46]. This chapter starts with a discussion of diamond Raman lasers in section 5.1. Then we discuss modelling of the diamond Raman incorporating the absorption from the NV^- centres in section 5.2. The response of such a laser with the absorption from the NV^- centres in the presence of a magnetic field is explored with numerical solutions in section 5.3. Finally in section 5.4 conclusions with a comment about possible extensions of the model are presented.

5.1 Diamond Raman laser

Let us briefly look into the basics of the diamond Raman laser first. For now we neglect the NV^- centre inside the diamond crystal. The underlying physical process behind the Raman laser is the Raman scattering [126]. Like other materials diamond crystal made out of carbon atoms bonded together also possesses phononic energy eigen values [127]. This crystal can thus scatter an incident optical frequency by modifying the phononic energy of the crystal and thereby the incident frequency gets converted into a different frequency. Such a scattering process can happen in two different ways. First, if the crystal is occupying a higher phononic energy eigen state, the material can lose energy and de-excite to the lower eigen state when the material is illuminated with an optical frequency. The optical frequency gains the energy

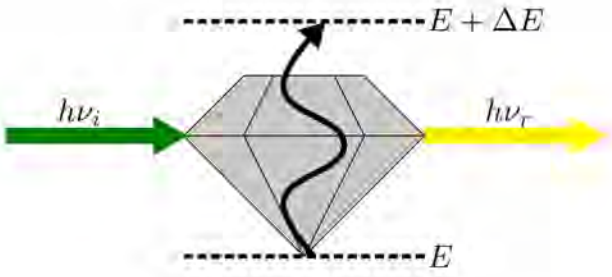

Figure 5.1: Representation of Raman scattering. The green arrows represent the incident frequency (ν_i), the yellow arrow represent the scattered Raman frequency (ν_r), and the black arrow represents the excitation of the diamond from the lower vibrational energy eigen state E to the higher vibrational energy eigen state $E + \Delta E$. Here h is Planck's constant.

lost by the material de-excitation and as a result is converted to a higher optical frequency. This process is known as anti-Stokes Raman scattering. Second, if the material is in its lower phononic energy eigen state, illuminating with an optical frequency, excites the material to the higher eigen state by extracting energy from the optical frequency. As a result the incident frequency gets scattered to a lower frequency and this process is known as Stokes Raman scattering. At room temperature the lower phonoic eigen state population is higher than that of higher state. Thus the Stokes scattering is always stronger than the anti-Stokes counterpart and it is the useful one for creating the Raman laser. Hence we consider the Stokes Raman scattering and for simplicity we refer the Stokes Raman scattering as Raman scattering for the rest of this thesis.

If ν_i is the incident optical frequency, ν_r is the Raman frequency, E is the phononic energy eigen value of the diamond material, and ΔE is the energy differnce to the next higher phonon eigen state from E, the energy corresponding to the Raman frequency can be written as

$$h\nu_r = h\nu_i - \Delta E, \tag{5.1}$$

where h is Planck's constant. A pictorial representation of the Raman scattering is given in Figure 5.1. For diamond, the frequency shift $\frac{\Delta E}{h}$ is ~ 40 THz.

The Raman scattering can be stimulated in the presence of light at the Raman frequency with the incident frequency and such a process is known as stimulated Raman scattering (SRS) [127–129]. The amplification of the stimulated Raman scattering by the optical cavity forms the Raman laser. The spontaneously emitted Raman into the cavity mode self-seeds to stimulate the further Raman scattering. In the NV$^-$ laser or more generally in any inversion laser, the energy is extracted from the pump via population inversion, but in the Raman laser no energy is stored in the system and the pump laser directly impacts the laser gain [125].

Typically diamond Raman lasers are considered for high power Raman lasers, however, there is a constant interest towards realizing Raman lasers with low pump powers [130, 131]. Recent demonstrations with ring resonators with high Q-factor shows the diamond Raman lasers function in the IR as well as NIR regions with a few tens of mW pump powers [130, 131].

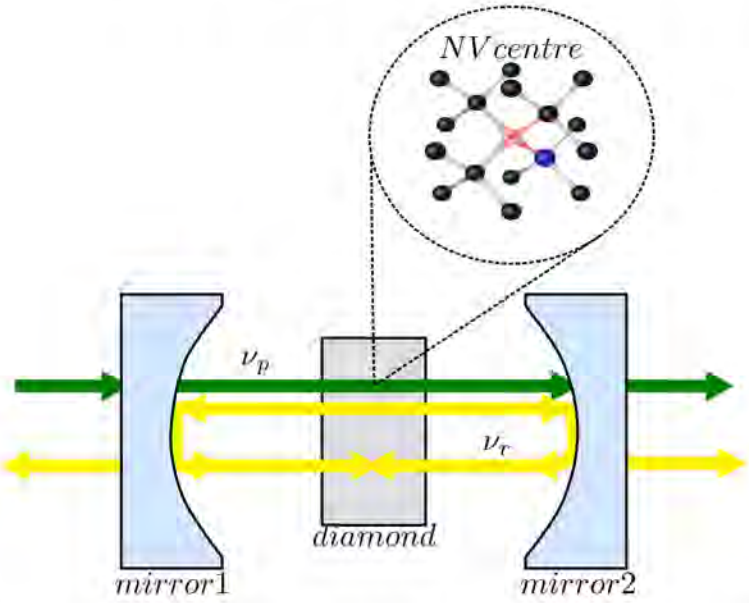

Figure 5.2: Schematic of the Raman laser with diamond crystal containing NV$^-$ centres in the Fabry-Perot cavity. The pump frequency corresponds to the green arrow (ν_p) and the Raman laser frequency corresponds to yellow arrow (ν_r). The Fabry-Perot cavity is formed between $mirror1$ and $mirror2$. The diamond crystal contains NV$^-$ centres (a representative one is shown in the inset). The pump is considered as a singe pass pump, i.e. the cavity has no effect on the pump frequency and the direction of pump is shown with the arrow head. The Raman frequency forms cavity mode and a laser signal is generated. The laser output is considered to be excited through both $mirror1$ and $mirror2$.

5.2 Modelling a diamond Raman laser with MW driven NV$^-$ centres in the crystal

In this section we model a diamond Raman laser modified by the MW driven NV$^-$ centres' absorption, inside the crystal. We can do this by assuming a general Frabry-Perot cavity as the laser cavity and then applying the fibre-cavity parameters. A schematic of the diamond Raman lasing with NV$^-$ centres is shown in Figure 5.2

The pump frequency for the laser is ν_p and the Raman frequency is $\nu_r = \nu_p + (40\ \text{THz})$. For simplicity, we can assume that both the mirrors, $mirror1$ and $mirror2$ are identical and fully transmitting all the frequencies including pump and higher order Raman frequencies, except the first Raman frequency, which forms a fundamental Gaussian mode of the cavity. Furthermore, we can assume that the diamond is fully filling the cavity volume and the NV$^-$ centres are uniformly distributed throughout the diamond.

5.2.1 Diamond Raman laser with an absorber in the crystal

We can first model the diamond Raman laser treating the absorber generally to get a pump-laser output relation. For this we can follow modelling the Raman laser in an approach similar to references [132, 133]. However, the important difference is that the absorption of both the pump and Raman frequency is considered here. We can first consider the depletion of the pump and estimate how much Raman gain has been generated from that. Then we can consider the rate equation of the Raman laser to reach a pump intensity to Raman laser output relation.

The Raman gain from the SRS is $g_r I_p I_r$ [127, 129, 132, 133], g_r is the plane Raman gain coefficient, I_p is the intensity of the pump beam, and I_r is the intensity of the Raman beam. For ease of calculation, we neglect any spontaneous emissions from the diamond, including spontaneous Raman Scattering and NV$^-$ emission from diamond at all the Raman frequencies. Then the depletion of pump when it propagate through the diamond can be written as [133],

$$\frac{\mathrm{d}I_p}{\mathrm{d}l} = -\frac{\nu_p}{\nu_r} g_r I_p(l) I_r - \beta_p I_p(l), \tag{5.2}$$

where, the β_p represents the pump absorption, I_r is approximated to be uniform throughout the cavity and the $I_p(l)$ is a function of length (l). Usually this pump absorption is neglected for simplicity [133]. Since we are interested in the absorption, we keep the β_p. However, we make the approximation that the β_p is also uniform through out the cavity and independent of length, for simplicity. Furthermore, we also approximate the Gaussian propagation of the cavity mode along the cavity length to a cylinder shape with top-flat approximation.

Using the method of separation of variables and integrating over the cavity length, we obtain $I_p(l)$ as [133],

$$I_p(l) = I_p^0 \exp\left\{-l\left(\frac{\nu_p}{\nu_r} g_r I_r + \beta_p\right)\right\}, \tag{5.3}$$

where I_p^0 is the intensity of the pump entering to the cavity through $mirror1$ as it hits the diamond crystal. If l_{cav} is the cavity length, then the depleted intensity of the pump when it passes through the diamond sample can be written as,

$$\Delta I_p = I_p^0\left(1 - \exp\left\{-l_{cav}\left(\frac{\nu_p}{\nu_r} g_r I_r + \beta_p\right)\right\}\right). \tag{5.4}$$

Following the method in reference [133], the total intensity of Raman generated from equation 5.4 can be written as,

$$\Delta I_r = \frac{g_r I_r}{\frac{\nu_p}{\nu_r} g_r I_r + \beta_p} I_p^0\left(1 - \exp\left\{-l_{cav}\left(\frac{\nu_p}{\nu_r} g_r I_r + \beta_p\right)\right\}\right). \tag{5.5}$$

Considering c as the speed of light and the n_m as the refractive index of the medium, which is diamond here, the time for the pump to just pass once through the cavity is $\sim \frac{l_{cav}}{c/n_m}$. Then the rate of Raman generation is $\frac{c/n_m}{l_{cav}} \Delta I_r$ [132]. Hence, the rate equation for the Raman laser intensity inside the cavity can be written as,

$$\frac{\mathrm{d}I_s}{\mathrm{d}t} = \frac{c/n_m}{l_{cav}} \frac{g_r I_r}{\frac{\nu_p}{\nu_r} g_r I_r + \beta_p} I_p^0\left(1 - \exp\left\{-l_{cav}\left(\frac{\nu_p}{\nu_r} g_r I_r + \beta_p\right)\right\}\right) - (c/n_m)\beta_r I_r - \kappa_r I_r, \tag{5.6}$$

where t represents time, β_r is the Raman absorption along the cavity length, and κ_r Raman photon loss rate of the cavity. At steady state, $\frac{\mathrm{d}I_s}{\mathrm{d}t} = 0$. Then from equation (5.6), we can write I_p^0 as

$$I_p^0 = \frac{(c/n_m)\beta_r + \kappa_r}{\frac{c/n_m}{l_{cav}} \frac{g_r}{\frac{\nu_p}{\nu_r} g_r I_r + \beta_p}\left(1 - \exp\left\{-l_{cav}\left(\frac{\nu_p}{\nu_r} g_r I_r + \beta_p\right)\right\}\right)}. \tag{5.7}$$

Equation (5.7) gives a relation between the incident pump intensity I_p^0 and the intra-cavity Raman laser intensity. From the intra-cavity Raman laser intensity, the intensity of the Raman laser output emitted from the cavity can be written as

$$I_r^{out} = \frac{l_{cav}}{c/n_m} \kappa_r I_r. \tag{5.8}$$

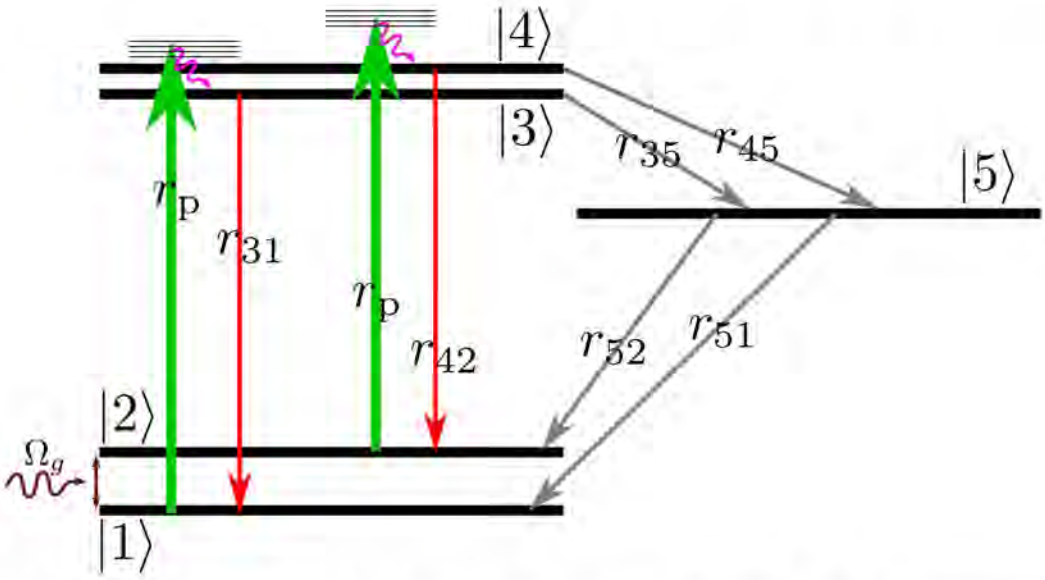

Figure 5.3: Rate equation model of the NV⁻ centre as a five level system. The levels $|1\rangle$ and $|3\rangle$ are the m_s=0 states of the ground and excited states respectively, whereas, levels $|2\rangle$ and $|4\rangle$ are m_s=±1 states of the ground and excited states respectively. Level $|5\rangle$ is the summarized singlet state. Levels $|1\rangle$ and $|2\rangle$ are resonantly driven with MW frequency resonant with the ground state splitting. Green upward arrows represent pumping, red downward arrows represent radiative decay and grey arrows represent decay via singlet states. The pumping rate and decay rate for each transition is represented is shown on each transition.

Using equation (5.8), we can write equation (5.7) as

$$I_p^0 = \frac{(c/n_m)\beta_r + \kappa_r}{\frac{\frac{(c/n_m)}{l_{cav}} g_r}{\frac{\nu_p}{\nu_r}\frac{(c/n_m)}{l_{cav}}\frac{g_r}{\kappa_r} I_r^{out} + \beta_p} \left(1 - \exp\left\{-l_{cav}\left(\frac{\nu_p}{\nu_r}\frac{(c/n_m)}{l_{cav}}\frac{g_r}{\kappa_r} I_r^{out} + \beta_p\right)\right\}\right)}. \tag{5.9}$$

The pump power is $P_p^{in} = I_p^0 A_{beam}$ and the Raman laser output power is $P_r^{out} = I_r^{out} A_{beam}$.

Now, in equation (5.9), we have a relation between I_p^0 and I_r^{out}. However, in order to make a quantitative estimate, we need to know β_p and β_r. Assuming the absorption is only from NV⁻ centres, we can estimate them by modelling the NV⁻ centre as an absorber.

5.2.2 NV⁻ centre as an absorber in the crystal

We have already seen the NV⁻ centre models in the previous chapters. Here, for simplicity, we consider an NV⁻ centre as a five level system for the rate equation model as shown in Figure 5.3, similar to the model that we have seen for the NV⁻ laser model in Chapter 3. The difference is that we do not consider any phonon levels of the ground state and the stimulated emission of the NV⁻ centres. Here also we consider the ground levels $|1\rangle$ and $|2\rangle$ are resonantly driven with MW frequency ~ 2.88 GHz with a Rabi frequency Ω_g as in the previous chapters. The spontaneous emission from levels $|2\rangle$ and $|1\rangle$ are also neglected with the assumption that the dephasing with a dephasing rate, Γ_g is the major source of noise to the resonant driving. Then the master equation for the single NV⁻ centre resonantly driven with MW frequency can be written as

$$\frac{\mathrm{d}p_{|12\rangle}}{\mathrm{d}t} = (i\Delta_g - r_p - \Gamma_g)p_{|12\rangle} - i\frac{\Omega_g}{2}(p_{|2\rangle} - p_{|1\rangle}), \tag{5.10}$$

$$\frac{\mathrm{d}p_{|21\rangle}}{\mathrm{d}t} = -(i\Delta_g + r_p + \Gamma_g)p_{|21\rangle} - i\frac{\Omega_g}{2}(p_{|1\rangle} - p_{|2\rangle}), \tag{5.11}$$

$$\frac{\mathrm{d}p_{|1\rangle}}{\mathrm{d}t} = -i\frac{\Omega_g}{2}(p_{|21\rangle} - p_{|12\rangle}) - r_p p_{|1\rangle} + r_{31}p_{|3\rangle} + r_{51}p_{|5\rangle}, \tag{5.12}$$

$$\frac{\mathrm{d}p_{|2\rangle}}{\mathrm{d}t} = i\frac{\Omega_g}{2}(p_{|21\rangle} - p_{|12\rangle}) - r_p p_{|2\rangle} + r_{42}p_{|4\rangle} + r_{52}p_{|5\rangle}, \tag{5.13}$$

$$\frac{\mathrm{d}p_{|3\rangle}}{\mathrm{d}t} = r_p p_{|1\rangle} - (r_{31} + r_s + r_{35})p_{|3\rangle}, \tag{5.14}$$

$$\frac{\mathrm{d}p_{|4\rangle}}{\mathrm{d}t} = r_p p_{|2\rangle} - (r_{42} + r_s + r_{45})p_{|4\rangle}, \tag{5.15}$$

$$\frac{\mathrm{d}p_{|5\rangle}}{\mathrm{d}t} = r_{35}p_{|3\rangle} + r_{45}p_{|4\rangle} - (r_{52} + r_{51})p_{|5\rangle}, \tag{5.16}$$

where the occupational probability of a particular level is,

$$\sum_{j=0}^{5} p_{|j\rangle} = 1. \tag{5.17}$$

Solving equations from (5.10) to (5.17) analytically for steady state, the ground state population fraction can be written as $p_{|\mathrm{gr}\rangle} = p_{|1\rangle} + p_{|2\rangle}$. Then the absorption per unit length for both the pump and Raman frequency, neglecting the orientation of NV$^-$ centres for simplicity, can be written as,

$$\beta_{\mathrm{p,\,r}} = \sigma_{\mathrm{p,\,r}} p_{|\mathrm{gr}\rangle}\rho_{NV}, \tag{5.18}$$

where $\sigma_{\mathrm{p,\,r}}$ is the absorption-cross section for the pump or Raman frequency and ρ_{NV} is the density of NV$^-$ centres in the diamond crystal. The $\beta_{\mathrm{p,\,r}}$ is actually a function of intensity of the pump rate from the ground state r_{p} through $p_{|\mathrm{gr}\rangle}$. The pump rate from the ground state $p_{|\mathrm{gr}\rangle}$ can be written as,

$$r_{\mathrm{p}} = \frac{\sigma_{\mathrm{p}} I_{\mathrm{p}}}{h\nu_{\mathrm{p}}} + \frac{\sigma_{\mathrm{r}} I_{\mathrm{r}}}{h\nu_{\mathrm{r}}} \tag{5.19}$$

Hence, $\beta_{p,r}$ is a function of pump and Raman Intensity. In the previous section, for deriving the Raman laser absorption, we made the approximation that β_p and β_r are independent of length for simplicity. In other words, the pump depletion is neglected due to the NV$^-$ centre absorption. Then we can approximate r_{p} so that the laser equation is easy to compute,

$$r_{\mathrm{p}} \sim \frac{\sigma_{\mathrm{p}} I_{\mathrm{p}}^0}{h\nu_{\mathrm{p}}} + \frac{\sigma_{\mathrm{r}} I_{\mathrm{r}}}{h\nu_{\mathrm{r}}}. \tag{5.20}$$

This equation is valid only close to the threshold where only a negligible fraction of the pump power is depleted.

We can identify two different possibilities for absorption by the NV$^-$ centres, due to the position of the pump and Raman wavelengths with respect to the ZPL. If both the pump and Raman wavelengths are below ZPL, the NV$^-$ centres can absorb both the wavelengths. However, if only the pump wavelength is below ZPL and the Raman wavelength is above ZPL, the NV$^-$ centre absorbs only pump wavelength as the Raman wavelength cannot excite the NV$^-$ centres ideally.

5.3 Numerical results of the Raman laser model with NV$^-$ absorption

Now using $\beta_{p,r}$, we can numerically solve equation (5.9) to understand the Raman laser behaviour with NV$^-$ absorption in these two wavelength regimes. We solve equation (5.9) numerically using Brent's root finding method (*brentq* method in *Python*). In order to numerically solve the equation, a closed interval in which the sign of the function changes is required. The sign changing interval for Brent's method is obtained from equation (5.9) itself. The right hand side of the equation (5.9) also contains I_p^0 through the absorption terms and it makes the equation complicated. We have seen that the I_p^0 dependence on the absorption terms come through the ground state population fraction $p_{|\mathrm{gr}\rangle}$. However, we can write $0 \leq p_{|\mathrm{gr}\rangle} \leq 1$. Hence, we can write $I_p^0(p_{|\mathrm{gr}\rangle} = 0) \leq I_p^0 \leq I_p^0(p_{|\mathrm{gr}\rangle} = 1)$, where, $I_p^0(p_{|\mathrm{gr}\rangle} = 0)$ and $I_p^0(p_{|\mathrm{gr}\rangle} = 1)$ can be written as

$$I_p^0(\rho_g = 0) = \frac{\frac{\nu_p}{\nu_r} I_r^{out}}{(1 - \exp\left\{-l_{cav}(\frac{\nu_p}{\nu_r}\frac{(c/n_m)}{l_{cav}}\frac{g_r}{\kappa_r} I_r^{out})\right\})}, \tag{5.21}$$

and,

$$I_p^0(\rho_g = 1) = \frac{((c/n_m)\sigma_s\rho_{nv}) + \kappa_r}{\frac{\frac{(c/n_m)}{l_{cav}} g_r}{\frac{\nu_p}{\nu_r}\frac{(c/n_m)}{l_{cav}}\frac{g_r}{\kappa_r} I_r^{out} + (\sigma_s\rho_{nv})}(1 - \exp\left\{-l_{cav}(\frac{\nu_p}{\nu_r}\frac{(c/n_m)}{l_{cav}}\frac{g_r}{\kappa_r} I_r^{out} + \sigma_s\rho_{nv})\right\})}. \tag{5.22}$$

Then the sign changing interval can be written as $[I_p^0(\rho_g = 0), I_p^0(\rho_g = 1)]$.

For numerical solving, we consider a micro cavity with a diamond sample of around 50 μm thickness as in the previous chapters. Then the cavity length is $l_{cav} = 50\,\mu m$. The small mode volume and the tight focusing of the micro-cavity is expected to provide Raman lasers with low threshold pump power. As we mentioned earlier in this chapter, we approximate the beam shape inside the cavity to a cylinder shape with flat-top approximation. The base radius of the cylinder is assumed to be the cavity beam waist. We consider a beam waist around 5μm. As we have already seen earlier in this thesis, such beam waist values are possible with fibre cavities [47]. We can set the cavity loss rate to 1 GHz, similar to the NV$^-$ laser case and then we can use the parameters that are used in section 3.2.3 for the internal rates of the NV$^-$ centre, except the absorption cross-sections.

5.3.1 Raman lasers with absorption of both Pump and Raman wavelengths by NV$^-$ centres

Here we assume the pump wavelength λ_p is 532 nm, which is the common wavelength especially for NV$^-$ excitation. Then the Raman wavelength λ_r is around 573 nm. The Raman gain for this case g_r is around 18.51 cm/GW [134–136]. The absorption cross-section of the NV$^-$ centre for the pump wavelength is same as the previously considered value in this thesis. The absorption cross-section of Raman wavelength is $\sigma_p \sim 5.3 \times 10^{-17}$ cm^2 [137].

We can first consider the NV$^-$ density $\rho_{NV} \sim 10^{14}$ cm^{-3} anticipating a strong intra-cavity absorption of the strong cavity field at the Raman wavelength by the NV$^-$ centres above threshold. The obtained steady state numerical solution for the Raman laser output power as a function of pump power is shown in Figure 5.4.

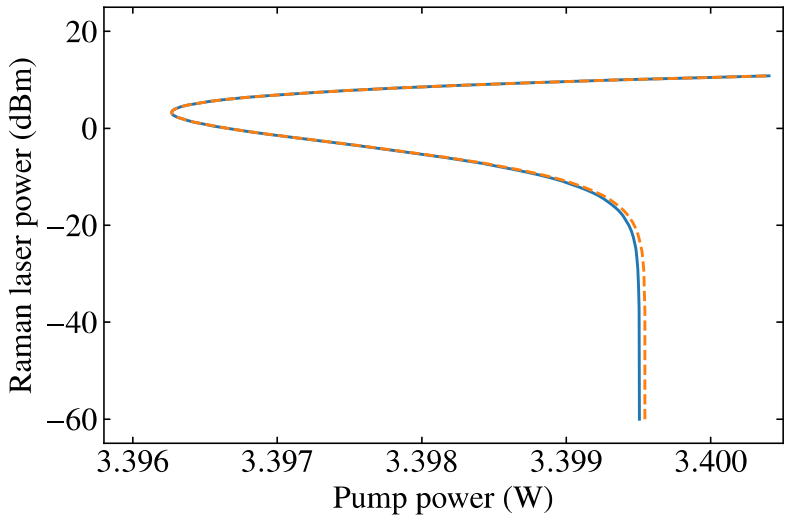

Figure 5.4: Diamond Raman laser bistability when NV$^-$ centres in the crystal absorb both pump and Raman wavelengths. The blue curve corresponds to resonant microwave driving and the orange curve corresponds to a detuning between the MW and the ground state splitting by ~ 2.88 GHz. The Raman laser output is shown in dBm to show two threshold pump powers, which are pump powers for which the slope of the laser curve tends to infinity. The threshold with the higher pump power is the forward threshold and the threshold with a lower pump power is the backward threshold.

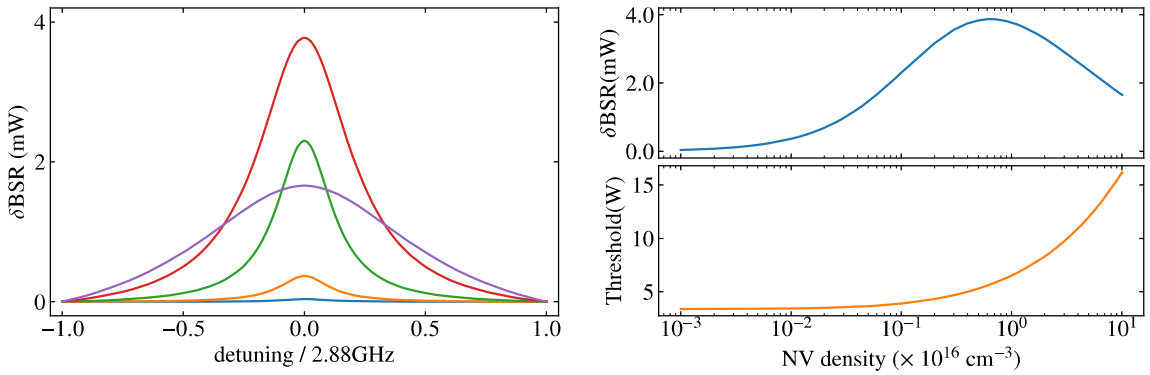

(a) (b)

Figure 5.5: (a) Absolute difference in the bistabity region δBSR as a function of the as a function detuning, for different values of NV density (ρ_{NV}). The blue curve is for $\rho_{NV} \sim 10^{14}\,\mathrm{cm}^{-3}$, The orange curve is for $\rho_{NV} \sim 10^{15}\,\mathrm{cm}^{-3}$, The green curve is for $\rho_{NV} \sim 10^{16}\,\mathrm{cm}^{-3}$, The red curve is for $\rho_{NV} \sim 10^{17}\,\mathrm{cm}^{-3}$, The purple curve is for $\rho_{NV} \sim 10^{18}\,\mathrm{cm}^{-3}$. (b) Absolute difference in the bistabity region δBSR and the forward threshold pump power for the resonant case as a function NV density in the crystal (ρ_{NV}). The blue curve shows how the δBSR changes and the orange curve shows how the corresponding threshold values changes.

In the Figure 5.4, we can see a bistable [138–143] behaviour of the Raman laser. When the pump power increases from zero, the Raman laser output remains zero unless it reaches the forward threshold. When the pump power reaches forward threshold, the laser output power switches to a high value. Decreasing the pump power, after bringing the laser output power to a high value, the laser output does not go to zero even if it is below the forward threshold. Once it reaches the backward threshold, Raman laser output will switch back to zero. The region of the plot in Figure 5.4 with negative slope appeared since we numerically solved for the pump power corresponding to each Raman laser output. In experiments, this region is invisible directly. This bistability behaviour is due to the saturation of absorption of the NV^- centres in the diamond crystal. Since we have a really good cavity, the competition between the cavity loss through the mirror and the absorption by the NV^- centres happens. Above threshold the strong intra-cavity field saturates the NV^-, and as a result the cavity loss through the mirror dominates and the laser output can be observed.

It is interesting to see that we obtain the bistability curve with magnetic/MW tunability, even with very low NV density, $\rho_{NV} \sim 10^{14}\text{cm}^2$. However, no such bistability has been reported so far in diamond Raman laser experiments, to the best of author's knowledge. We can interpret that this might be an effect of the micro-cavity that reduces the threshold pump power of the Raman laser and there by enables NV^- centres' absorption significant.

We can now further explore the tunability of the bistability. For this we consider the bistable regions of the two cases in the pump powers. The bistable region in the pump power means the difference between forward and backward thresholds' pump powers. Since the backward threshold is not tunable with magnetic field, magnetic field tunability of the bistability can be expressed as the difference between the forward thresholds of the detuned and resonant cases. We can represent this as the absolute difference in bistability (δBSR). The absolute difference in δBSR as a function of detuning, for different NV^- densities in shown in Figure 5.5(a). Furthermore, δBSR as well as forward threshold as a function of NV^- density is also shown in in Figure 5.5(b). From the Figures 5.5(a) and 5.5(b), we can see that the δBSR is a few milli Watts and it increases initially with the density, but drops for higher densities. Increasing the density, the line-width of each plot in Figure 5.5(a) increases, indicating the insensitivity against MW. The tunability of bistability should be coming from the availability of NV^- centres in the ground state for absorption. The NV centres in the ground state also absorb pump wavelength along with the Raman wavelength. Then one could interpret that the reason for a maximum in Figure 5.5(b) is due to the decrease in the availability of NV^- centres due to the pump absorption dominating over the increase in the total number of NV^- centres in the cavity due to the NV^- density increase.

Developing a magnetic sensing module using the discussed diamond Raman laser bistability remains an open challenge at the time of this thesis submission. More studies are required towards this direction.

5.3.2 Raman lasers with absorption of Pump wavelength by the NV^- centres

In this subsection, we consider that the pump wavelength is below ZPL and the Raman wavelength is above ZPL. To see the effect we can arbitrarily consider the pump wavelength λ_p is around 620 nm, and the corresponding Raman wavelength λ_r is around 676 nm. The Raman gain for this case is then $g_\text{r} \sim 14.64$ cm/GW [134–136]. The absorption cross-section of the pump wavelength $\sigma_p \sim 1.27 \times 10^{-17}\text{cm}^2$ [137]. As we have already approximated, the absorption cross-section of the Raman wavelength $\sigma_r \sim 0$. This is only true in ideal case, but

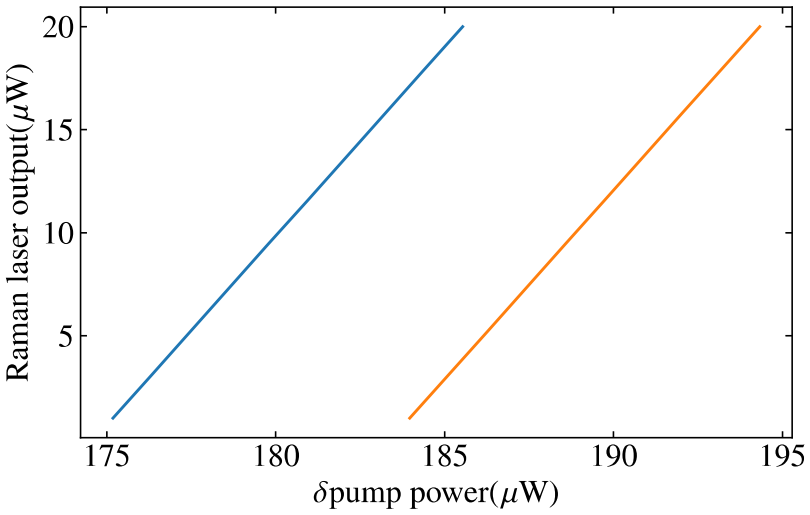

Figure 5.6: Raman laser output power as a function of pump power for resonant and detuned cases. The axis is δpump power obtained by subtracting a constant power of 4.292 W from the pump powers for clear visualization. The blue line shows the output power for the resonant driving and the orange curve shows the output power when the MW is detuned from the ground state splitting by $\sim$ 2.88 GHz.

at least the σ_r is expected to be negligible compared with the σ_p.

Since there is no Raman wavelength absorption, intuitively one does not expect to see the bistability, instead a threshold shifted laser with detuning. In order to see this effect clearly, we consider a high density of NV$^-$ centres, 1×10^{16} cm^{-3} roughly in the range as we have seen in the previous chapters. Then the Raman laser equation is numerically solved as mentioned in the previous subsections and the resultant Raman laser output as a function of pump laser power in shown Figure 5.6.

In Figure 5.7, two laser output curves are shown. The first one in blue color is the output power when the NV$^-$ centres are resonantly driven with a MW frequency. The second one in orange color is the Raman laser output power when there is a detuning of $\sim$ 2.88 GHz between the NV$^-$ centres and the MW. The threshold of the detuned laser curve is shifted to a higher value, than that of the resonant one. For the resonant case less spins are available in the $m_s = 0$ of the ground state compared with that of the non-resonant case for absorption. Hence, the resonant case reaches the threshold faster than the detuned case.

To see how the laser output behaves as a function of detuning for a fixed pump power, we can assume that the MW frequency for driving the NV$^-$ centres is constant at a fixed value and the detuning is induced by some external magnetic field. Then we can see how the laser behaves as a function of magnetic field for a fixed pump power. We numerically solve the Raman laser output as a function of external magnetic field as shown in Figure 5.7(a). The detuning to the resonant driving can be done in two different ways. The MW frequency itself can be detuned with respect to the resonant to the NV$^-$ centres ground state splitting. Or bringing a magnet close to the NV$^-$ centre can induce detuning.

For ease in calculating the slope of the curve in Figure 5.7(a), we fit the numerical solution with a Lorentzian function. The derivative of the obtained Lorentzian function with the fit parameters gives the slope of the curve. From that we can estimate the sensitivity for each external magnetic field present and the result is shown in Figure 5.7(b) similar to the NV$^-$ laser. Similar to the NV$^-$ laser, close to zero magnetic field the laser is not sensitive to the external magnetic field. This can be attribute to the fact that the slope of the Figure 3.8 tends

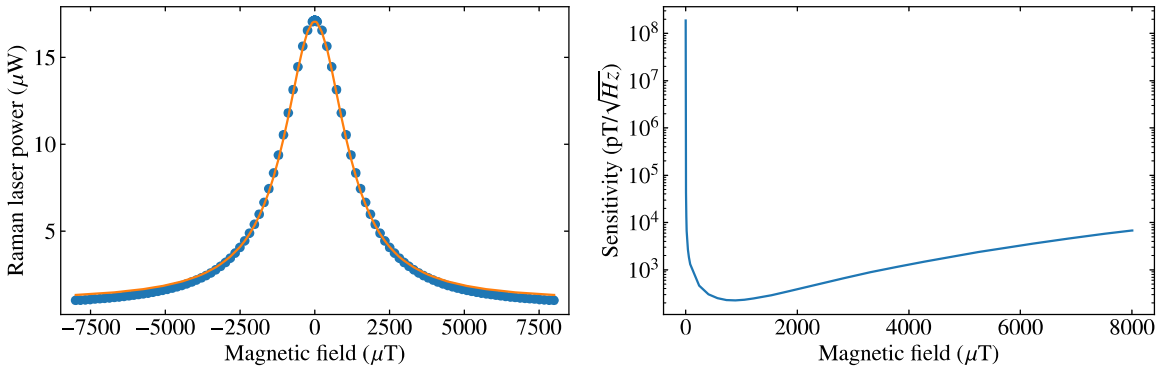

(a) (b)

Figure 5.7: (a) Raman laser output power as a function of relative magnetic field present The blue points are the numerical solution. The orange line is a lorentzian fit to the numerical solution. (b) DC magnetic field sensitivity of Raman laser as a function of relative external magnetic field.

to zero. This suggests that one needs to provide detuning via magnetic field if the MW is resonant to the ground state splitting of NV centres or via adjusting the MW frequency itself for engineering a magnetic sensor with the minimum sensitivity. The minimum sensitivity estimated in the present case is $\sim 226\,\mathrm{pT}/\sqrt{Hz}$. The advantage of this method compared to the usual absorption method [71, 144] is that unlike these methods, we can eliminate background photons in the signal containing information about magnetic field, by working at the threshold. Then the noise in the magnetic field measurement with the Raman laser is expected to be lower, compared to the usual absorption magnetometry with NV^- centres.

5.4 Comments on the approximations of the modelling

So far in this chapter we have only considered the NV^-. However, the charge state switching of the NV centres is possible as we have already seen in the previous chapters and the present model shown here is an ideal case. As a result for an accurate modelling of the Raman laser response against the magnetic field should include the charge state switching between NV^- and NV^0 centres. However, unlike the model that is shown in section 4.3.4 in the Chapter 4, such a model should include coherence effects due to the MW driving.

In experiments ionization from NV^- centres to NV^0 centres is a challenge to overcome, particularly when only the pump wavelength is below ZPL of NV^- centre, since there the pump wavelength in this case is higher than than the ZPL of NV^0. A way to circumvent this problem might be to illuminate the diamond with another green light that is enough to re-pump from NV^0 centres to NV^-. However, in this case the sensitivity is expected to reduce.

Apart from that, for the case considered in subsection 5.3.1, the Raman wavelength 573 nm is close to the ZPL of the NV^0 at 575 nm, which might bring some additional resonance effects. As a result including the charge state switching into the present model, requires careful master equation modelling, which is beyond the scope of this thesis. Furthermore, since we are considering cavities with high Q-factor, the cavity can alter the both the emission of the NV^- centres and the Raman emission. In the case considered in section 5.3.2, the emission is around 676 nm. The NV^- centres emit around this wavelength due to the phonon side band. The presence of a cavity with high Q-factor can induce Purcell enhancement [50]

on the NV^- emission or the stimulated emission of NV^- centres as we discussed before, and thereby can alter the population fractions of different states of NV^- centres. The Raman spontaneous emission can also altered by the Purcell enhancement [145] and the gain due to the stimulated emission can also enhanced. In an accurate model, these cavity effect also should be considered.

"It doesn't matter how beautiful your theory is, it doesn't matter how smart you are. If it doesn't agree with experiment, it's wrong."

Richard P. Feynman

6 Conclusions and outlook

This thesis has demonstrated substantial progress towards the understanding and engineering of high-sensitivity, robust magnetic-field sensors using diamond lasers based on fibre-cavity platforms. A room-temperature fiber cavity has been designed, implemented, and refined to provide the platform for a range of experiments. In particular, we were able to observe the interplay of stimulated emission and charge state switching for an NV-diamond-loaded fiber cavity. Amplification of laser light resonant with the phononic NV sideband was observed, and the qualitative agreement between our model and the experiments suggests stimulated emission to be the main mechanism. This strengthens the interpretation of the previously reported experimental results in the Jeske et al paper from 2017 [45], and we have gone beyond the previous work by considering the known effect of ionization. In this regard, our findings give a more complete (and complex) picture of the physics of stimulated emission of NV centres.

While no self-seeded NV^- lasing was observed, the results presented in this thesis do not preclude this possibility. The key consideration illuminated here is the fact that under strong resonant intra-cavity power, the ionisation dynamics shift the balance between NV^- and NV^0 towards the neutral charge state. As a result, self seeded NV lasing in a fiber cavity with better Q factor still seems feasible, with both the neutral and the negatively-charged NV states contributing as gain medium. However, the strong NV^0 contribution puts a question mark behind the feasibility of reaching the originally anticipated sensitivities for a laser threshold magnetometer based on an NV laser [43]. Clearly, this question deserves more work both on the experimental and theoretical side, including a detailed consideration of the spin-dependence of the singlet ionisation process. Once a better understanding is reached, careful materials engineering might allow for stabilization of the NV^- centre.

Furthermore, improvements to the fiber-cavity design, specifically a suitably designed coating that enhances the green pump laser on top of the red laser, could be advantageous since the green laser favours NV^0 to NV^- recombination. Experimentally, active feedback and stabilization of the cavity would allow for more systematic studies and better controlled external parameters. First efforts are under way at Macquarie University, with pioneering work from other groups[122, 146], demonstrating the feasibility of achieving stable fiber-cavity operation under ambient conditions.

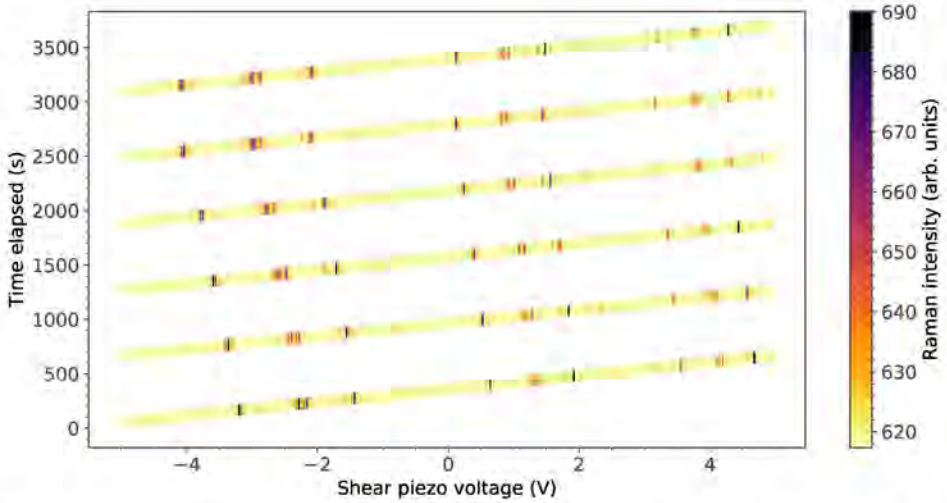

Figure 6.1: Spontaneous Raman emission recorded when slowly sweeping the fiber cavity length. The six stripes correspond to six identical piezo voltage sweeps. Each scan shows three groups of cavity transmission resonances and each of these groups in turn corresponds to a set of transverse modes belonging to one fundamental longitudinal mode.

Prompted by the complexity of building a magnetically tunable NV laser, the thesis has also investigated the feasibility of realizing a laser threshold magnetometer using a diamond Raman laser with microwave-driven NV^- centres as absorbers in the diamond material. This work provides an insight into the behavior of low-threshold diamond Raman lasers, which could be of general interest for engineering diamond Raman lasers – a field of research that is very active at Macquarie University and also in other prominent groups around the world. A key finding of the theoretical modelling described is the choice of pump wavelength that determines the position of the Raman-shifted laser output wavelength with respect to the ZPL of the NV^- centre. When both the pump and the Raman-shifted laser wavelength are below the NV^- ZPL, the model predicts a magnetically tunable bistability in a low-threshold laser formed by a cavity with tight focus and high Q-factor. This bistability is dependent on the number of NV^- centres. While it looks that this bistability only has limited applications in magnetic sensing (unfortunately), it definitely should be taken into account when constructing a Raman laser with tight focus (small mode volume) and high Q-factor, since it drastically enhances intra-cavity power at threshold.

Unlike case where NV centres were acting as amplifiers, the diamond Raman laser model developed here does not consider the problem of NV charge state switching at present. Due to the coherent MW drive, the proper inclusion of the ionisation process would require a careful master equation modelling. Since the charge-state switching itself is a spin-dependent process [100], as explained in the amplification model, it is hard to provide an intuitive argument about the predictions of such a model. Furthermore given a fibre-cavity has a small mode volume, Purcell-enhancement of the stimulated Raman emission might have to be included, which in-turn has the potential to alter the Raman gain of the laser. Developing such a model will be an important future step towards the realisation of this kind of absorptive magnetic sensor, and may yield benefits for other applications of diamond Raman lasers.

In order to realize a Raman laser in experiments using fiber cavities, it will likely be necessary to enhance both pump and Raman light using a doubly-resonant cavity. First preliminary experiments with a doubly-resonant fibre cavity, loaded with a diamond of low NV-centre concentration, were performed and showed spontaneous Raman emission as

illustrated in Figure 6.1. However, the present fiber coatings were not designed for this purpose and hence a new generation of fiber cavities is required in order to further pursue this line of research in the future.

This thesis makes it apparent that some important challenges remain in order to achieve the proposed Laser Threshold Magnetometry. Although engineering challenges remain in cavity design and construction, it is clear that the fibre-cavity system is capable of providing the physical compactness desired in a magnetic field sensor probe. It is important to better understand and characterise the light induced charge-state conversion of NV centres, and these problems are receiving attention do to the wide range of applications outside magnetometry that demand this information. The transformative and disruptive impact of a compact, high-sensitivity, room-temperature magnetic field probe provide substantial motivation to continue this line of research.

References

[1] J. P. Dowling and G. J. Milburn. *Quantum technology: the second quantum revolution*. Philosophical Transactions of the Royal Society of London. Series A: Mathematical, Physical and Engineering Sciences **361**(1809), 1655 (2003).

[2] M. Walport and P. Knight. *The quantum age: Technological opportunities*. Government Office for Science (2016).

[3] A. Zagoskin. *A brief subjective perspective on the development of quantum technologies 2.0*. Journal of the Physical Society of Japan **88**(6), 061001 (2019).

[4] E. Cartlidge. *Quantum sensors: A revolution in the offing?* Optics and Photonics News **30**(9), 24 (2019).

[5] S. Ritter and J. Stuhler. *The control of quantum states with lasers: Latest innovations for quantum technologies*. PhotonicsViews **16**(3), 75 (2019).

[6] E. Schrodinger. *Are there quantum jumps*. Brit. J. Philos. Sci **3**, 233 (1952).

[7] F. Arute, K. Arya, R. Babbush, D. Bacon, J. C. Bardin, R. Barends, R. Biswas, S. Boixo, F. G. Brandao, D. A. Buell, *et al. Quantum supremacy using a programmable superconducting processor*. Nature **574**(7779), 505 (2019).

[8] T. Roberson and A. White. *Charting the australian quantum landscape*. Quantum Science and Technology **4**(2), 020505 (2019).

[9] *Australian Research Council Centre of Excellence for Engineered Quantum Systems*. URL https://equs.org/.

[10] *Sydney Quantum Academy*. URL https://sydneyquantum.org/.

[11] N. Gisin, G. Ribordy, W. Tittel, and H. Zbinden. *Quantum cryptography*. Reviews of modern physics **74**(1), 145 (2002).

[12] C. L. Degen, F. Reinhard, and P. Cappellaro. *Quantum sensing*. Reviews of modern physics **89**(3), 035002 (2017).

[13] S. J. Williamson and L. Kaufman. *Biomagnetism*. Journal of Magnetism and Magnetic Materials **22**(2), 129 (1981).

[14] M. Hämäläinen, R. Hari, R. J. Ilmoniemi, J. Knuutila, and O. V. Lounasmaa. *Magnetoencephalography-theory, instrumentation, and applications to noninvasive studies of the working human brain*. Reviews of modern Physics **65**(2), 413 (1993).

[15] S. Khan and D. Cohen. *Using the magnetoencephalogram to noninvasively measure magnetite in the living human brain.* Human brain mapping **40**(5), 1654 (2019).

[16] G. Baule and R. McFee. *Theory of magnetic detection of the heart's electrical activity.* Journal of Applied Physics **36**(6), 2066 (1965).

[17] D. Cohen, Y. Palti, B. N. Cuffin, and S. J. Schmid. *Magnetic fields produced by steady currents in the body.* Proceedings of the National Academy of Sciences **77**(3), 1447 (1980).

[18] M. N. Nabighian, V. Grauch, R. Hansen, T. LaFehr, Y. Li, J. Peirce, J. Phillips, and M. Ruder. *The historical development of the magnetic method in exploration.* Geophysics **70**(6), 33ND (2005).

[19] J. F. Barry, J. M. Schloss, E. Bauch, M. J. Turner, C. A. Hart, L. M. Pham, and R. L. Walsworth. *Sensitivity optimization for nv-diamond magnetometry.* arXiv preprint arXiv:1903.08176 (2019).

[20] R. Fagaly. *Superconducting quantum interference device instruments and applications.* Review of scientific instruments **77**(10), 101101 (2006).

[21] D. Budker and M. Romalis. *Optical magnetometry.* Nature physics **3**(4), 227 (2007).

[22] M. W. Doherty, N. B. Manson, P. Delaney, F. Jelezko, J. Wrachtrup, and L. C. Hollenberg. *The nitrogen-vacancy colour centre in diamond.* Physics Reports **528**(1), 1 (2013).

[23] C. Degen. *Scanning magnetic field microscope with a diamond single-spin sensor.* Applied Physics Letters **92**(24), 243111 (2008).

[24] J. Taylor, P. Cappellaro, L. Childress, L. Jiang, D. Budker, P. Hemmer, A. Yacoby, R. Walsworth, and M. Lukin. *High-sensitivity diamond magnetometer with nanoscale resolution.* Nature Physics **4**(10), 810 (2008).

[25] G. Balasubramanian, I. Chan, R. Kolesov, M. Al-Hmoud, J. Tisler, C. Shin, C. Kim, A. Wojcik, P. R. Hemmer, A. Krueger, *et al. Nanoscale imaging magnetometry with diamond spins under ambient conditions.* Nature **455**(7213), 648 (2008).

[26] J. Maze, P. Stanwix, J. Hodges, S. Hong, J. Taylor, P. Cappellaro, L. Jiang, M. G. Dutt, E. Togan, A. Zibrov, *et al. Nanoscale magnetic sensing with an individual electronic spin in diamond.* Nature **455**(7213), 644 (2008).

[27] C. Bradac, T. Gaebel, N. Naidoo, M. Sellars, J. Twamley, L. Brown, A. Barnard, T. Plakhotnik, A. Zvyagin, and J. Rabeau. *Observation and control of blinking nitrogen-vacancy centres in discrete nanodiamonds.* Nature nanotechnology **5**(5), 345 (2010).

[28] C. Bradac *et al. The properties of nitrogen-vacancy centres in nanodiamond* (2012).

[29] L. Rondin, J.-P. Tetienne, P. Spinicelli, C. Dal Savio, K. Karrai, G. Dantelle, A. Thiaville, S. Rohart, J.-F. Roch, and V. Jacques. *Nanoscale magnetic field mapping with a single spin scanning probe magnetometer.* Applied Physics Letters **100**(15), 153118 (2012).

[30] P. Maletinsky, S. Hong, M. S. Grinolds, B. Hausmann, M. D. Lukin, R. L. Walsworth, M. Loncar, and A. Yacoby. *A robust scanning diamond sensor for nanoscale imaging with single nitrogen-vacancy centres*. Nature nanotechnology **7**(5), 320 (2012).

[31] M. S. Grinolds, S. Hong, P. Maletinsky, L. Luan, M. D. Lukin, R. L. Walsworth, and A. Yacoby. *Nanoscale magnetic imaging of a single electron spin under ambient conditions*. Nature Physics **9**(4), 215 (2013).

[32] L. Thiel, Z. Wang, M. A. Tschudin, D. Rohner, I. Gutiérrez-Lezama, N. Ubrig, M. Gibertini, E. Giannini, A. F. Morpurgo, and P. Maletinsky. *Probing magnetism in 2d materials at the nanoscale with single-spin microscopy*. Science **364**(6444), 973 (2019).

[33] URL https://qzabre.com/.

[34] URL https://qnami.ch/.

[35] L. Rondin, J.-P. Tetienne, T. Hingant, J.-F. Roch, P. Maletinsky, and V. Jacques. *Magnetometry with nitrogen-vacancy defects in diamond*. Reports on progress in physics **77**(5), 056503 (2014).

[36] T. Wolf, P. Neumann, K. Nakamura, H. Sumiya, T. Ohshima, J. Isoya, and J. Wrachtrup. *Subpicotesla diamond magnetometry*. Physical Review X **5**(4), 041001 (2015).

[37] L. P. McGuinness, Y. Yan, A. Stacey, D. A. Simpson, L. T. Hall, D. Maclaurin, S. Prawer, P. Mulvaney, J. Wrachtrup, F. Caruso, *et al. Quantum measurement and orientation tracking of fluorescent nanodiamonds inside living cells*. Nature nanotechnology **6**(6), 358 (2011).

[38] D. Le Sage, K. Arai, D. R. Glenn, S. J. DeVience, L. M. Pham, L. Rahn-Lee, M. D. Lukin, A. Yacoby, A. Komeili, and R. L. Walsworth. *Optical magnetic imaging of living cells*. Nature **496**(7446), 486 (2013).

[39] J. F. Barry, M. J. Turner, J. M. Schloss, D. R. Glenn, Y. Song, M. D. Lukin, H. Park, and R. L. Walsworth. *Optical magnetic detection of single-neuron action potentials using quantum defects in diamond*. Proceedings of the National Academy of Sciences **113**(49), 14133 (2016).

[40] M. Karadas, A. M. Wojciechowski, A. Huck, N. O. Dalby, U. L. Andersen, and A. Thielscher. *Feasibility and resolution limits of opto-magnetic imaging of neural network activity in brain slices using color centers in diamond*. Scientific reports **8**(1), 4503 (2018).

[41] URL https://www.lockheedmartin.com/en-us/news/features/2019-features/tech-thats-cool-as-dark-ice.html.

[42] URL https://www.wired.com/story/quantum-physicists-found-a-new-safer-way-to-navigate/.

[43] J. Jeske, J. H. Cole, and A. D. Greentree. *Laser threshold magnetometry*. New Journal of Physics **18**(1), 013015 (2016).

[44] V. G. Savitski. *Optical gain in nv-colour centres for highly-sensitive magnetometry: a theoretical study*. Journal of Physics D: Applied Physics **50**(47), 475602 (2017).

[45] J. Jeske, D. W. Lau, X. Vidal, L. P. McGuinness, P. Reineck, B. C. Johnson, M. W. Doherty, J. C. McCallum, S. Onoda, F. Jelezko, *et al. Stimulated emission from nitrogen-vacancy centres in diamond*. Nature communications **8**, 14000 (2017).

[46] Y. Dumeige, J.-F. Roch, F. Bretenaker, T. Debuisschert, V. Acosta, C. Becher, G. Chatzidrosos, A. Wickenbrock, L. Bougas, A. Wilzewski, *et al. Infrared laser threshold magnetometry with a nv doped diamond intracavity etalon*. Optics express **27**(2), 1706 (2019).

[47] D. Hunger, T. Steinmetz, Y. Colombe, C. Deutsch, T. W. Hänsch, and J. Reichel. *A fiber fabry–perot cavity with high finesse*. New Journal of Physics **12**(6), 065038 (2010).

[48] H. Kaupp, C. Deutsch, H.-C. Chang, J. Reichel, T. W. Hänsch, and D. Hunger. *Scaling laws of the cavity enhancement for nitrogen-vacancy centers in diamond*. Physical Review A **88**(5), 053812 (2013).

[49] E. Janitz, M. Ruf, M. Dimock, A. Bourassa, J. Sankey, and L. Childress. *Fabry-perot microcavity for diamond-based photonics*. Physical Review A **92**(4), 043844 (2015).

[50] H. Kaupp, T. Hümmer, M. Mader, B. Schlederer, J. Benedikter, P. Haeusser, H.-C. Chang, H. Fedder, T. W. Hänsch, and D. Hunger. *Purcell-enhanced single-photon emission from nitrogen-vacancy centers coupled to a tunable microcavity*. Physical Review Applied **6**(5), 054010 (2016).

[51] S. B. van Dam, M. Ruf, and R. Hanson. *Optimal design of diamond-air microcavities for quantum networks using an analytical approach*. New Journal of Physics **20**(11), 115004 (2018).

[52] S. Häußler, J. Benedikter, K. Bray, B. Regan, A. Dietrich, J. Twamley, I. Aharonovich, D. Hunger, and A. Kubanek. *Diamond photonics platform based on silicon vacancy centers in a single-crystal diamond membrane and a fiber cavity*. Physical Review B **99**(16), 165310 (2019).

[53] B. Romeira and A. Fiore. *Purcell effect in the stimulated and spontaneous emission rates of nanoscale semiconductor lasers*. IEEE Journal of Quantum Electronics **54**(2), 1 (2018).

[54] R. Schirhagl, K. Chang, M. Loretz, and C. L. Degen. *Nitrogen-vacancy centers in diamond: nanoscale sensors for physics and biology*. Annual review of physical chemistry **65**, 83 (2014).

[55] S. Hong, M. S. Grinolds, L. M. Pham, D. Le Sage, L. Luan, R. L. Walsworth, and A. Yacoby. *Nanoscale magnetometry with nv centers in diamond*. MRS bulletin **38**(2), 155 (2013).

[56] J. Tetienne, L. Rondin, P. Spinicelli, M. Chipaux, T. Debuisschert, J. Roch, and V. Jacques. *Magnetic-field-dependent photodynamics of single nv defects in diamond: an application to qualitative all-optical magnetic imaging*. New Journal of Physics **14**(10), 103033 (2012).

[57] A. Gupta, L. Hacquebard, and L. Childress. *Efficient signal processing for time-resolved fluorescence detection of nitrogen-vacancy spins in diamond*. JOSA B **33**(3), B28 (2016).

[58] L. Robledo, H. Bernien, T. Van Der Sar, and R. Hanson. *Spin dynamics in the optical cycle of single nitrogen-vacancy centres in diamond.* New Journal of Physics **13**(2), 025013 (2011).

[59] C. Wang. *A solid-state single photon source based on color centers in diamond.* Ph.D. thesis, lmu (2007).

[60] V. Acosta, A. Jarmola, E. Bauch, and D. Budker. *Optical properties of the nitrogen-vacancy singlet levels in diamond.* Physical Review B **82**(20), 201202 (2010).

[61] L. Rogers, S. Armstrong, M. Sellars, and N. Manson. *Infrared emission of the nv centre in diamond: Zeeman and uniaxial stress studies.* New Journal of Physics **10**(10), 103024 (2008).

[62] H. Zheng, J. Xu, G. Z. Iwata, T. Lenz, J. Michl, B. Yavkin, K. Nakamura, H. Sumiya, T. Ohshima, J. Isoya, *et al. Zero-field magnetometry based on nitrogen-vacancy ensembles in diamond.* Physical Review Applied **11**(6), 064068 (2019).

[63] W. M. Itano, J. C. Bergquist, J. J. Bollinger, J. Gilligan, D. J. Heinzen, F. Moore, M. Raizen, and D. J. Wineland. *Quantum projection noise: Population fluctuations in two-level systems.* Physical Review A **47**(5), 3554 (1993).

[64] L. M. Pham. *Magnetic field sensing with nitrogen-vacancy color centers in diamond.* Tech. rep., MASSACHUSETTS INST OF TECH CAMBRIDGE (2013).

[65] K. Arai. *Precision magnetometry and imaging via quantum manipulation of spins in diamond.* Ph.D. thesis, Massachusetts Institute of Technology (2016).

[66] H. Clevenson, M. E. Trusheim, C. Teale, T. Schröder, D. Braje, and D. Englund. *Broadband magnetometry and temperature sensing with a light-trapping diamond waveguide.* Nature Physics **11**(5), 393 (2015).

[67] H.-P. Breuer, F. Petruccione, *et al. The theory of open quantum systems* (Oxford University Press on Demand, 2002).

[68] J. R. Johansson, P. D. Nation, and F. Nori. *Qutip 2: A python framework for the dynamics of open quantum systems.* Computer Physics Communications **184**(4), 1234 (2013).

[69] A. Dréau, M. Lesik, L. Rondin, P. Spinicelli, O. Arcizet, J.-F. Roch, and V. Jacques. *Avoiding power broadening in optically detected magnetic resonance of single nv defects for enhanced dc magnetic field sensitivity.* Physical Review B **84**(19), 195204 (2011).

[70] S. Ahmadi, H. A. El-Ella, A. M. Wojciechowski, T. Gehring, J. O. Hansen, A. Huck, and U. L. Andersen. *Nitrogen-vacancy ensemble magnetometry based on pump absorption.* Physical Review B **97**(2), 024105 (2018).

[71] R. Walsworth. *Absorbtion-based detection of spin impurities in solid-state spin systems* (2017). US Patent 9,658,301.

[72] V. Acosta, E. Bauch, A. Jarmola, L. Zipp, M. Ledbetter, and D. Budker. *Broadband magnetometry by infrared-absorption detection of nitrogen-vacancy ensembles in diamond*. Applied Physics Letters **97**(17), 174104 (2010).

[73] K. Jensen, N. Leefer, A. Jarmola, Y. Dumeige, V. M. Acosta, P. Kehayias, B. Patton, and D. Budker. *Cavity-enhanced room-temperature magnetometry using absorption by nitrogen-vacancy centers in diamond*. Physical review letters **112**(16), 160802 (2014).

[74] G. Chatzidrosos, A. Wickenbrock, L. Bougas, N. Leefer, T. Wu, K. Jensen, Y. Dumeige, and D. Budker. *Miniature cavity-enhanced diamond magnetometer*. Physical Review Applied **8**(4), 044019 (2017).

[75] A. E. Siegman. *Lasers university science books*. Mill Valley, CA **37**(208), 169 (1986).

[76] N. Ismail, C. C. Kores, D. Geskus, and M. Pollnau. *Fabry-pérot resonator: spectral line shapes, generic and related airy distributions, linewidths, finesses, and performance at low or frequency-dependent reflectivity*. Optics express **24**(15), 16366 (2016).

[77] F. Träger. *Springer handbook of lasers and optics* (Springer Science & Business Media, 2012).

[78] D. A. Steck. *Classical and modern optics*. course notes available online at http://steck.us/teaching (2006 (revision 1.7.5, 3 October 2019)).

[79] V. Vins and E. Pestryakov. *Color centers in diamond crystals: Their potential use in tunable and femtosecond lasers*. Diamond and related materials **15**(4-8), 569 (2006).

[80] E. Fraczek, V. G. Savitski, M. Dale, B. G. Breeze, P. Diggle, M. Markham, A. Bennett, H. Dhillon, M. E. Newton, and A. J. Kemp. *Laser spectroscopy of nv-and nv0 colour centres in synthetic diamond*. Optical Materials Express **7**(7), 2571 (2017).

[81] L. Hacquebard and L. Childress. *Charge-state dynamics during excitation and depletion of the nitrogen-vacancy center in diamond*. Physical Review A **97**(6), 063408 (2018).

[82] S. D. Subedi, V. V. Fedorov, J. Peppers, D. V. Martyshkin, S. B. Mirov, L. Shao, and M. Loncar. *Laser spectroscopic characterization of negatively charged nitrogen-vacancy (nv-) centers in diamond*. Optical Materials Express **9**(5), 2076 (2019).

[83] O. Peterson, J. Webb, W. McColgin, and J. Eberly. *Organic dye laser threshold*. Journal of Applied Physics **42**(5), 1917 (1971).

[84] E. Rittweger. *Maximizing far-field optical microscopy resolution through selected fluorophore transitions*. Ph.D. thesis (2009).

[85] A. Gruber, A. Dräbenstedt, C. Tietz, L. Fleury, J. Wrachtrup, and C. Von Borczyskowski. *Scanning confocal optical microscopy and magnetic resonance on single defect centers*. Science **276**(5321), 2012 (1997).

[86] B. Aull and H. Jenssen. *Vibronic interactions in nd: Yag resulting in nonreciprocity of absorption and stimulated emission cross sections*. IEEE Journal of Quantum Electronics **18**(5), 925 (1982).

[87] C. Bradac, M. T. Johnsson, M. van Breugel, B. Q. Baragiola, R. Martin, M. L. Juan, G. K. Brennen, and T. Volz. *Room-temperature spontaneous superradiance from single diamond nanocrystals*. Nature communications **8**(1), 1205 (2017).

[88] M. L. Juan, C. Bradac, B. Besga, M. Johnsson, G. Brennen, G. Molina-Terriza, and T. Volz. *Cooperatively enhanced dipole forces from artificial atoms in trapped nanodiamonds*. Nature Physics **13**(3), 241 (2017).

[89] D. Riedel, I. Söllner, B. J. Shields, S. Starosielec, P. Appel, E. Neu, P. Maletinsky, and R. J. Warburton. *Deterministic enhancement of coherent photon generation from a nitrogen-vacancy center in ultrapure diamond*. Physical Review X **7**(3), 031040 (2017).

[90] A. Edmonds, U. D'Haenens-Johansson, R. Cruddace, M. Newton, K.-M. Fu, C. Santori, R. Beausoleil, D. Twitchen, and M. Markham. *Production of oriented nitrogen-vacancy color centers in synthetic diamond*. Physical Review B **86**(3), 035201 (2012).

[91] S. W. Hell and J. Wichmann. *Breaking the diffraction resolution limit by stimulated emission: stimulated-emission-depletion fluorescence microscopy*. Optics letters **19**(11), 780 (1994).

[92] T. A. Klar and S. W. Hell. *Subdiffraction resolution in far-field fluorescence microscopy*. Optics letters **24**(14), 954 (1999).

[93] E. Rittweger, K. Y. Han, S. E. Irvine, C. Eggeling, and S. W. Hell. *Sted microscopy reveals crystal colour centres with nanometric resolution*. Nature Photonics **3**(3), 144 (2009).

[94] D. Wildanger, J. R. Maze, and S. W. Hell. *Diffraction unlimited all-optical recording of electron spin resonances*. Physical review letters **107**(1), 017601 (2011).

[95] D. Wildanger, B. R. Patton, H. Schill, L. Marseglia, J. Hadden, S. Knauer, A. Schönle, J. G. Rarity, J. L. O'Brien, S. W. Hell, *et al. Solid immersion facilitates fluorescence microscopy with nanometer resolution and sub-ångström emitter localization*. Advanced Materials **24**(44), OP309 (2012).

[96] S. Arroyo-Camejo, M.-P. Adam, M. Besbes, J.-P. Hugonin, V. Jacques, J.-J. Greffet, J.-F. Roch, S. W. Hell, and F. Treussart. *Stimulated emission depletion microscopy resolves individual nitrogen vacancy centers in diamond nanocrystals*. ACS nano **7**(12), 10912 (2013).

[97] B. Harke, J. Keller, C. K. Ullal, V. Westphal, A. Schönle, and S. W. Hell. *Resolution scaling in sted microscopy*. Optics express **16**(6), 4154 (2008).

[98] T. A. Klar, E. Engel, and S. W. Hell. *Breaking abbeś diffraction resolution limit in fluorescence microscopy with stimulated emission depletion beams of various shapes*. Physical Review E **64**(6), 066613 (2001).

[99] N. Aslam, G. Waldherr, P. Neumann, F. Jelezko, and J. Wrachtrup. *Photo-induced ionization dynamics of the nitrogen vacancy defect in diamond investigated by single-shot charge state detection*. New Journal of Physics **15**(1), 013064 (2013).

[100] R. P. Roberts, M. L. Juan, and G. Molina-Terriza. *Spin-dependent charge state interconversion of nitrogen vacancy centers in nanodiamonds*. Physical Review B **99**(17), 174307 (2019).

[101] F. Kleißler. *Towards Solid-state Spin Based, High-fidelity Quantum Computation*. Ph.D. thesis, Georg-August-Universität Göttingen (2018).

[102] N. B. Manson, M. Hedges, M. S. Barson, R. Ahlefeldt, M. W. Doherty, H. Abe, T. Ohshima, and M. J. Sellars. *Nv—n+ pair centre in 1b diamond*. New Journal of Physics **20**(11), 113037 (2018).

[103] M. S. Barson, E. Krausz, N. B. Manson, and M. W. Doherty. *The fine structure of the neutral nitrogen-vacancy center in diamond*. Nanophotonics (2019).

[104] E. Bourgeois, A. Jarmola, P. Siyushev, M. Gulka, J. Hruby, F. Jelezko, D. Budker, and M. Nesladek. *Photoelectric detection of electron spin resonance of nitrogen-vacancy centres in diamond*. Nature communications **6**, 8577 (2015).

[105] F. M. Hrubesch, G. Braunbeck, M. Stutzmann, F. Reinhard, and M. S. Brandt. *Efficient electrical spin readout of nv- centers in diamond*. Physical review letters **118**(3), 037601 (2017).

[106] P. Siyushev, M. Nesladek, E. Bourgeois, M. Gulka, J. Hruby, T. Yamamoto, M. Trupke, T. Teraji, J. Isoya, and F. Jelezko. *Photoelectrical imaging and coherent spin-state readout of single nitrogen-vacancy centers in diamond*. Science **363**(6428), 728 (2019).

[107] I. Meirzada, Y. Hovav, S. Wolf, and N. Bar-Gill. *Negative charge enhancement of near-surface nitrogen vacancy centers by multicolor excitation*. Physical Review B **98**(24), 245411 (2018).

[108] P. Siyushev, H. Pinto, M. Vörös, A. Gali, F. Jelezko, and J. Wrachtrup. *Optically controlled switching of the charge state of a single nitrogen-vacancy center in diamond at cryogenic temperatures*. Physical review letters **110**(16), 167402 (2013).

[109] P. Ji, R. Balili, J. Beaumariage, S. Mukherjee, D. Snoke, and M. G. Dutt. *Multiple-photon excitation of nitrogen vacancy centers in diamond*. Physical Review B **97**(13), 134112 (2018).

[110] D. A. Hopper, R. R. Grote, A. L. Exarhos, and L. C. Bassett. *Near-infrared-assisted charge control and spin readout of the nitrogen-vacancy center in diamond*. Physical Review B **94**(24), 241201 (2016).

[111] A. Wood. *Fibre cavities for microcavity polaritons* (2015).

[112] R. B. Balili. *Transfer matrix method in nanophotonics*. In *International Journal of Modern Physics: Conference Series*, vol. 17, pp. 159–168 (World Scientific, 2012).

[113] G. Muñoz-Matutano, A. Wood, M. Johnsson, X. Vidal, B. Q. Baragiola, A. Reinhard, A. Lemaître, J. Bloch, A. Amo, G. Nogues, *et al. Emergence of quantum correlations from interacting fibre-cavity polaritons*. Nature materials **18**(3), 213 (2019).

[114] R. Albrecht, A. Bommer, C. Deutsch, J. Reichel, and C. Becher. *Coupling of a single nitrogen-vacancy center in diamond to a fiber-based microcavity*. Physical review letters **110**(24), 243602 (2013).

[115] A. D. Greentree. *Nanodiamonds in fabry-perot cavities: a route to scalable quantum computing*. New Journal of Physics **18**(2), 021002 (2016).

[116] W. Rosenfeld. *A high finesse optical resonator for cavity qed experiments*. Diplom thesis, Universität Bonn (2003).

[117] M. Capelli, A. Heffernan, T. Ohshima, H. Abe, J. Jeske, A. Hope, A. Greentree, P. Reineck, and B. Gibson. *Increased nitrogen-vacancy centre creation yield in diamond through electron beam irradiation at high temperature*. Carbon **143**, 714 (2019).

[118] Y. G. Boucher. *Theoretical investigation of amplified spontaneous emission in an active structure by extended (3x3) transfer matrix formalism: the case of a non-uniform longitudinal distribution of emitters*. Journal of the European Optical Society-Rapid publications **1** (2006).

[119] G. Moody, M. Segnon, I. Sagnes, R. Braive, A. Beveratos, I. Robert-Philip, N. Belabas, F. Jahnke, K. L. Silverman, R. P. Mirin, *et al. Delayed formation of coherence in the emission dynamics of high-q nanolasers*. Optica **5**(4), 395 (2018).

[120] J. M. Binder, A. Stark, N. Tomek, J. Scheuer, F. Frank, K. D. Jahnke, C. Müller, S. Schmitt, M. H. Metsch, T. Unden, *et al. Qudi: A modular python suite for experiment control and data processing*. SoftwareX **6**, 85 (2017).

[121] T.-L. Wee, Y.-K. Tzeng, C.-C. Han, H.-C. Chang, W. Fann, J.-H. Hsu, K.-M. Chen, and Y.-C. Yu. *Two-photon excited fluorescence of nitrogen-vacancy centers in proton-irradiated type ib diamond*. The Journal of Physical Chemistry A **111**(38), 9379 (2007).

[122] J. F. Brachmann, H. Kaupp, T. W. Hänsch, and D. Hunger. *Photothermal effects in ultra-precisely stabilized tunable microcavities*. Optics express **24**(18), 21205 (2016).

[123] R. P. Mildren, A. Sabella, O. Kitzler, D. J. Spence, and A. M. McKay. *Diamond raman laser design and performance*. Optical Engineering of Diamond pp. 239–276 (2013).

[124] R. P. Mildren, A. McKay, R. J. Williams, and O. Kitzler. *Diamond raman lasers*. Optics and Photonics News **25**(9), 42 (2014).

[125] R. J. Williams, O. Kitzler, Z. Bai, S. Sarang, H. Jasbeer, A. McKay, S. Antipov, A. Sabella, O. Lux, D. J. Spence, *et al. High power diamond raman lasers*. IEEE Journal of Selected Topics in Quantum Electronics **24**(5), 1 (2018).

[126] C. V. Raman. *A new radiation*. Indian Journal of physics **2**, 387 (1928).

[127] H. M. Pask. *The design and operation of solid-state raman lasers*. Progress in Quantum Electronics **27**(1), 3 (2003).

[128] G. Eckhardt, D. Bortfeld, and M. Geller. *Stimulated emission of stokes and anti-stokes raman lines from diamond, calcite, and α-sulfur single crystals*. Applied Physics Letters **3**(8), 137 (1963).

[129] A. Penzkofer, A. Laubereau, and W. Kaiser. *High intensity raman interactions*. Progress in Quantum Electronics **6**(2), 55 (1979).

[130] P. Latawiec, V. Venkataraman, M. J. Burek, B. J. Hausmann, I. Bulu, and M. Lončar. *On-chip diamond raman laser*. Optica **2**(11), 924 (2015).

[131] P. Latawiec, V. Venkataraman, A. Shams-Ansari, M. Markham, and M. Lončar. *Integrated diamond raman laser pumped in the near-visible*. Optics letters **43**(2), 318 (2018).

[132] S. Ding, X. Zhang, Q. Wang, F. Su, S. Li, S. Fan, S. Zhang, J. Chang, S. Wang, and Y. Liu. *Theoretical models for the extracavity raman laser with crystalline raman medium*. Applied Physics B **85**(1), 89 (2006).

[133] O. Kitzler, A. McKay, D. J. Spence, and R. P. Mildren. *Modelling and optimization of continuous-wave external cavity raman lasers*. Optics express **23**(7), 8590 (2015).

[134] A. Sabella, D. J. Spence, and R. P. Mildren. *Pump–probe measurements of the raman gain coefficient in crystals using multi-longitudinal-mode beams*. IEEE Journal of Quantum Electronics **51**(12), 1 (2015).

[135] R. Mildren and J. Rabeau. *Optical engineering of diamond* (John Wiley & Sons, 2013).

[136] *Private communications with Prof. Richard P. Mildren*.

[137] *Private communications with Dr. Jan Jeske*.

[138] S. Ruschin and S. Bauer. *Bistability, hysteresis and critical behavior of a co2 laser, with sf6 intracavity as a saturable absorber*. Chemical Physics Letters **66**(1), 100 (1979).

[139] H. Gibbs. *Optical bistability: controlling light with light* (Elsevier, 2012).

[140] J. Liu, V. Petrov, U. Griebner, F. Noack, H. Zhang, J. Wang, and M. Jiang. *Optical bistability in the operation of a continuous-wave diode-pumped yb: Luvo 4 laser*. Optics express **14**(25), 12183 (2006).

[141] L. Zhang, L. Zhan, M. Qin, Z. Zou, Z. Wang, and J. Liu. *Large-region tunable optical bistability in saturable absorber-based single-frequency brillouin fiber lasers*. JOSA B **32**(6), 1113 (2015).

[142] T. Wang, L. Zhang, C. Feng, M. Qin, and L. Zhan. *Tunable bistability in hybrid brillouin–erbium single-frequency fiber laser with saturable absorber*. JOSA B **33**(8), 1635 (2016).

[143] S. Li, Q. Ge, Z. Wang, J. C. Martín, and B. Yu. *Optical bistability via an external control field in all-fiber ring cavity*. Scientific reports **7**(1), 8992 (2017).

[144] S. Ahmadi, H. A. El-Ella, J. O. Hansen, A. Huck, and U. L. Andersen. *Pump-enhanced continuous-wave magnetometry using nitrogen-vacancy ensembles*. Physical Review Applied **8**(3), 034001 (2017).

[145] D. Riedel, S. Flågan, P. Maletinsky, and R. J. Warburton. *Cavity-enhanced raman scattering for in situ alignment and characterization of solid-state microcavities*. arXiv preprint arXiv:1909.12333 (2019).

[146] E. Janitz, M. Ruf, Y. Fontana, J. Sankey, and L. Childress. *High mechanical bandwidth fiber-coupled fabry-perot cavity*. Optics express **25**(17), 20932 (2017).